POLITECNICO DI MILANO
DEPARTMENT OF MECHANICAL ENGINEERING
DOCTORAL PROGRAMME IN MECHANICAL ENGINEERING

CONTINUOUS HEALTH MONITORING OF RAILWAY AXLES USING VIBRATION MEASUREMENTS

Doctoral Dissertation of:
Mohamed Mahmoud Abdelkader Hassan

Supervisor:
Prof. Stefano Bruni

Tutor:
Prof. Stefano Beretta

The Chair of the Doctoral Program:
Prof. Daniele Rocchi

2018 – cycle XXX

Acknowledgements

Foremost, I would like to express my sincere gratitude to my supervisor Prof. Stefano Bruni for his continuous support of my Ph.D study and related research. I am very grateful for his patience, motivation and enthusiasm. His guidance helped me in all the time of research and writing this thesis. He is a great supervisor, intelligent, knowledgeable expert in his field and he has a very nice and caring personality. It is a great honor for me to have worked under his supervision and I could not have imagined working with a supervisor better than him. I will forever be grateful for everything he has done for me.

Besides my supervisor, I would like to thank Prof. Stefano Beretta (my tutor) and Prof. Michele Carboni not only for their encouragement, but also for the insightful comments I received during my research which guide me to improve and widen my research from various perspectives.

I wish to acknowledge all the members of the Railway Dynamics Research Group in which I am working, for their help, support and all the fun we had together. Thanks to the colleagues and friends at our department and a special thank to my officemate Dr. Binbin Liu. It is a real privilege to work in an environment that one can enjoy.

My sincere thanks also go to all members of my family, especially my parents, for their support and encouragement throughout my study.

Last, but not least, I also dedicate this Ph.D. thesis to my wife and my lovely children, *Lena* and *Hamza*, who are the pride and joy of my life. I love you all very much and I appreciate all your patience and support during my Ph.D. period.

MOHAMED MAHMOUD ABDELKADER HASSAN
MILAN, ITALY, JULY 2018

Abstract

RAILWAY axles are one of the most critical components in railway vehicles since their failure can lead to derailment and, potentially, to major safety issues. A large proportion of all accidents in the rail industry related to rolling stock failures is due to fatigue crack propagation in the axles. To avoid catastrophic failure, axles are inspected periodically at regular intervals to detect the presence of defects or faults. However, despite the high standards of present engineering practice in non-destructive inspection of axles, fatigue-induced in-service failures of railway axles still occasionally occur, representing a serious threat to the safe operation of railway systems. Therefore, the implementation of continuous structural health monitoring (SHM) technique plays a pivotal role in further reducing in-service failures of railway axles.

In this thesis, a new approach for continuous SHM parameters of railway axle during its operation is proposed. The approach depends on measuring the Low Frequency Vibration (LFV) arising from the axle in-service bending deflections. The methodology for estimating the condition of axle is based on the so called breathing mechanism of fatigue crack, which is affecting the bending stiffness and thus generating additional vibration in vertical and horizontal (perpendicular to axle axis in the traveling direction) directions due to the change of crack angular position with respect to the load direction. Specific patterns of this vibration, namely NxRev components (harmonic components at frequencies that are integer multiples of the frequency of rotation), can be used for axle fault detection purposes.

To assess the possible use of the proposed SHM approach, a combination of numerical and experimental investigations has been carried out. The numerical investigations are based on non-linear Finite Element (FE) models of cracked railway axle (considering both detailed solid models (using 3D elements) and simplified beam-line models (using Timoshenko beam elements) for solid and hollow axles. After validation, the models are used to investigate the optimal placement of sensors as well as the minimum size of a detectable crack. Experimental activities have been performed on the test bench for rotating bending tests on full-scale railway axle specimen available at the laboratory of the Department of Mechanical Engineering of Politecnico di Mialno.

In order to consider the effect of disturbances arising from train-track interaction, track irregularity and wheel out-of-roundness, a multi-body model of a complete railway vehicle is defined, incorporating one axle modelled as a flexible cracked axle. This model is totally new and, after verifications, was used to evaluate the NxRev components of axle vibration occurring in presence of axle cracks having different position along the axle and different size, in combination with different sources of disturbance.

Finally, signal processing techniques are proposed which are able to deal with the unfavorable signal/noise ratio presented by the crack detection problem and with the fact that the speed of revolution of the axle is not constant, leading to non-stationary vibration signal. To this aim, two de-noising strategies are proposed, one using a tacho-signal, the other only relying on acceleration measurements.

The final results of this work show that the fatigue crack of railway axles can be detected using the axle bending vibrations measurements. The 2xRev and 3xRev components of the horizontal axle-box acceleration are well correlated to the size of the crack and are almost insensitive to the effect of the disturbances considered in this study, hence, they can be used for the continuous monitoring of axle integrity. The signal processing technique developed in this work proved to be fully adequate to extract information related to the presence of a crack even in case of large variation of vehicle speed and large disturbance from wheel-rail interaction.

A simple criterion for crack detection threshold is defined and applied to the results, showing the possibility of detecting cracks with size in the order of 15-20% of the total section area, depending on crack location.

Contents

List of Figures

List of Tables

CHAPTER 1

Introduction

1.1 Background

Due to the increasing demand for faster and more secure rail transport, reliable passenger and freight rolling stocks are required. Railway vehicles consist of many different elements, some of which being critical from safety point of view. Wheelsets are one of the most critical components in railway vehicles, in both wagons and locomotives because their failures can lead to derailment and potentially, to major safety issues including loss of human lives. Train wheelsets consist of three main components, the wheels, the axle and the bearings.

A large proportion of all accidents in the rail industry related to rolling stock failures is due to crack propagation in the axles. To avoid catastrophic failures, axles components are inspected periodically at regular intervals in order to detect the presence of defects or faults, e.g. for freight wagons, every 600,000 km or 6 years. To apply an effective inspection test (like Magnetic Particles (MP) or Ultra-Sonic (US)) axles need to be removed from the bogie at the maintenance schedule and disassemble the auxiliary systems (e.g. the brakes and the traction motor) to access to the main body of the axles. Due to the possibility that the wheelset defects can develop during service and evolve very rapidly, the railway industry has started to invest heavily in the continuous monitoring of wheelsets to minimise the chance of a catastrophic derailment [1, 2].

According to recent study of the D-RAIL FP7 project considered the railway accidents that have been reported in 23 countries over the past years [3], it was shown that out of the 700 accidents considered, 37% of them were due to rolling stock faults (see Figure 1.1) and 84% of all rolling stock-related accidents were caused by wheelset and bogie defects (see Figure 1.2). In addition, the D-RAIL FP7 project showed that 41% of all rolling stock accidents were caused by axle failure which includes axle bearings failure and axle failure.

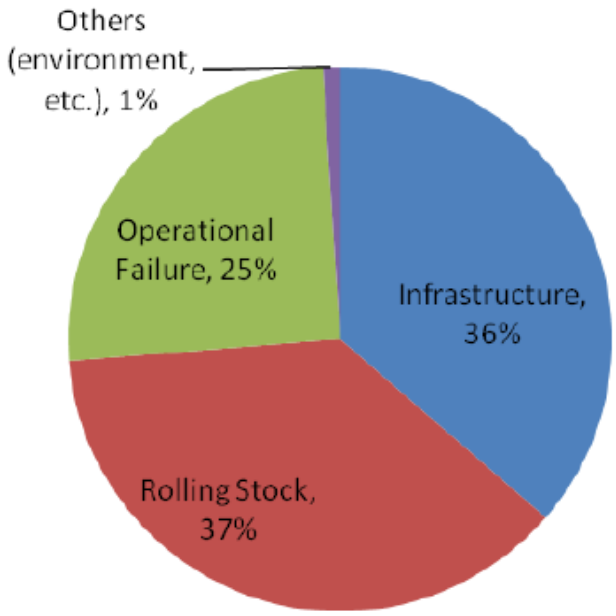

Figure 1.1: *Railway accidents cases considered in the D-RAIL FP7 project [2].*

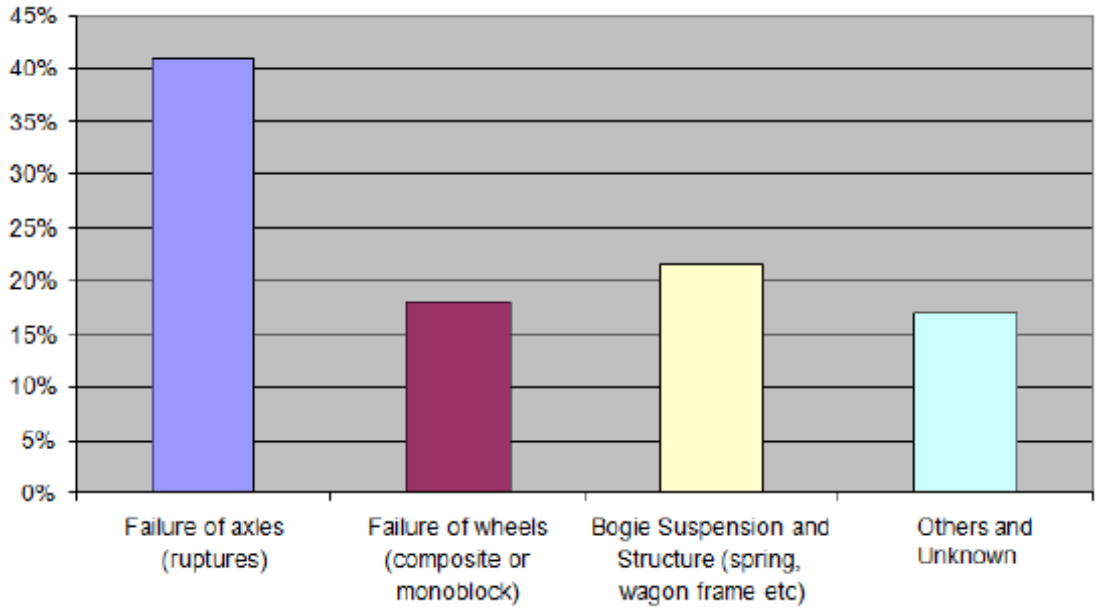

Figure 1.2: *Cases of rolling stock related accidents [2].*

If the axle or axle bearing defect is not detected promptly, it will gradually become more severe, leading to more serious damage which can lead to catastrophic failures [4]. Early detection of faults helps to schedule maintenance activities of rolling stock in a more efficient way without changing the minimum required availability of the trains. Bad maintenance scheduling can lead to reducing the number of available trains, which in some cases, can cause disturbance of normal train services giving rise to significant fines or in some cases can lead to serious accidents.

To avoid fatigue damage in railway axles, the traditional design methods [5,6] based on the fatigue limit are complemented by a damage tolerant approach [7, 8], according to which the axles are regularly inspected at proper maintenance intervals by US or MP testing. However, despite the high standards of present engineering practice in non-destructive inspection of axles, fatigue-induced in-service failures of railway axles still occasionally occur, representing a serious threat to the safe operation of railway systems. Therefore, the implementation of continuous structural health monitoring (SHM) technique plays a pivotal role in further reducing in-service failures of railway axles.

Different SHM techniques have been proposed to detect fatigue cracks in railway axles, including acoustic emission (AE) [9], high frequency vibrations (changes in natural frequencies) [10], microwave testing [11], alternating current field measurements [10], induced current focusing potential drop [10], AC thermography [12] and laser-air coupled hybrid UT [13].

1.2 Thesis objectives

Considering the actual State of the Art of technologies in railway axles inspections, as well as developments in other fields of industry, a new approach for continuous SHM of railway axles is proposed. The approach is based on measuring the Low Frequency Vibration (LFV) arising from the axle in-service bending deflections. The methodology for estimating the condition of axle is based on the so-called breathing mechanism of fatigue crack, which is affecting the bending stiffness and thus generating additional vibration in vertical and horizontal (perpendicular to axle axis in the traveling direction) directions due to the change of crack position with respect to the load direction. Specific patterns of this vibration, namely NxRev components (harmonic components at frequencies that are integer multiples of the frequency of rotation) can be used for fault detection purposes, which facilitates the continuous SHM of the axle.

This approach depends on measuring the axle-boxes vertical and horizontal accelerations and by means of Fourier transform, the vibration measurements can be converted from time domain to frequency domain (or to angle domain and then to order domain) to extract the signal harmonic components and track the harmonics trends during the axle service life. The proposed SHM technique was finalized by defining a warning criterion in order to give the operator an alarm about future failure of a cracked axle of the running train.

1.3 Thesis outline

More detailed considerations about railway axles maintenance, as well as the possibility of using the proposed SHM methodology in railway axle monitoring system will be detailed described in following chapters of this work:

Chapter 2: In this chapter, a review of the State of the Art of railway axles design requirements is introduced. Next, some examples of axles failed in-service are described. Afterward, different inspection techniques for railway axles are briefly described to give the reader insight of currently leading-edge technology of non-destructive testing and wayside inspection systems. Dynamics related to a crack in rotating shaft are briefly introduced considering the influence of the crack breathing mechanism, crack shapes and different crack modeling approaches.

Chapter 3: A complete description of Finite Element models of cracked railway axle is introduced in this chapter. These models consist of full-scale hollow and solid axles with complete properties, model of material damping, model of different crack sizes and different crack locations, considering several boundary conditions as for lab tests and as for a rolling wheelset in real environment.

Two models were built using different types of Finite Elements. The first model was built using solid elements included in ABAQUS commercial software. Considering the computational cost of the solid elements, a simplified model of the cracked axle using Timoshenko beam elements, the second model, was constructed and the effect of crack breathing mechanism was introduced at one element depending on the crack location and size. MATLAB software was used to implement the second model.

Two levels of validation are performed to test the validity of using the simple Finite Element model to represent the influence of breathing mechanism in railway axle dynamics. Firstly, validation against experimental results, obtained from full-scale rotating bending tests performed on the Dynamic Test Bench for Railway Axles available at the labs of Politecnico di Milano, is performed. Secondly, the Timoshenko beam FE model is compared to numerical results obtained from the solid FE model.

After validation, different locations of the crack with different sizes are modeled and their results are reported and discussed. To test the possibility of using this proposed technique in cases of axles with crack under press-fit parts, two experiments were carried out on full scale solid axle specimens and their results are included in this chapter.

Chapter 4: To take into account properly the effect of disturbances associated with track irregularity, wheel out of roundness and flexibility of the track, more realistic boundary conditions than the ones used in chapter 3 were considered for the wheelset. In this chapter, a multi-body (MB) model of a railway vehicle also considering track flexibility was built and merged with the Timoshenko beam FE model of one cracked axle to form a detailed model of a railway vehicle with one cracked axle.

In this model, called MB-FE model, the simplified model of crack breathing mechanism mentioned in chapter 3 is applied to a specific beam element, depending on the crack location. The MB-FE model was verified against Polimi conventional railway vehicle MB software (ADTReS). After verification, The MB-FE model was used to study the influence of different locations of crack propagation on the vibration signals measured at the vehicle axle-boxes in vertical and horizontal direction. Finally, in the last section of this chapter, a simple criterion for crack detection threshold is defined and applied to the numerical results of cracked axle.

Chapter 5: This chapter introduces a brief revision of the State of the Art of data treatment techniques regarding rotating machine signals. A proposed technique is presented to extract the NxRev features from non-stationary signals with low signal to noise ratio. The proposed signal processing technique is applied to crack simulated signal corrupted with random noise to assess the possibility of using this technique to extract the signal harmonics. Moreover, a tacho-less technique suitable for railway continuous SHM applications is proposed and validated.

Chapter 6: In this chapter, the conclusions of this work, as well as some further developments for the future work, are presented.

CHAPTER 2

Review of the State of the Art

2.1 Railway axles service life

Railway axles are commonly operated over a service life of 30 years or more which refers to a very high number of loading cycles in the order of 10^9. Railway axles are designed for a long term of operation. However, there are known cases of their failure, which are caused by defects that arise during the operation and serve as a source of origin and development of crack to critical size [14–16]. During the 20^{th} century, the number of failures of railway axles was reduced drastically due to improved steels and assessment concepts. According to the railway safety performance report of the European Railway Agency (ERA) of 2011 [1, 14], the number of broken axles in the European union between 2006 and 2009 was in total 329. Related to the number of about 1.66×10^{10} train kilometers over these four years this refers to one fracture event per 50.45 million train kilometers. Railway axles were investigated at the very beginning of fatigue research and design. Fatigue failure of axle has been a problem for engineers since the railway service started in the early part of the 19^{th} century.

Railway axles are one of the most important components in railway systems since a fail-safe design is not available where their failure can lead to derailment and, potentially, to major loss of functionality and human lives. In order to maintain the safety of railway systems, a large number of investigation and experiments have been carried out by outstanding research ever since, and many improvements have been made in the material, manufacturing, heat treatment, design method and inspection techniques. To increase the fatigue strength of the press fitted part of the axle, which suffered from fretting fatigue, heat treatment of induction hardening method has been applied. Axles in service are regularly checked by ultrasonic testing and magnetic particle inspection. It is known that in-service defects in the cylindrical bodies, especially in the axle of railway transport, often take the form of semi-elliptical surface crack [14–17].

One of the main parameters that characterize the fatigue crack growth (FCG) is the stress intensity factor (SIF). Press fit technology is commonly used for an attachment of components of railway wheelsets, e.g. axles, wheel and traction gears. Besides design of axles and press fitted joints including optimum dimensions, material selection and surface treatment are important issues. According to EN 13261 [6], steel EA1N and EA4T are considered as standard materials of railway axles, first of them being a low strength carbon steel with 0.4%C. EA4T is a low alloyed steel with fairly high strength. Despite a proper axle design is implemented, a chance of damage initiation due to corrosion, ballast impact or metallurgical defects during service cannot be completely eliminated. It is therefore common practice to regularly inspect railway axles by means of visual inspection or non-destructive testing (NDT) techniques.

2.2 Some railway accidents involving axles

Railway axles and wheels are a couple of the most important components in railway vehicle with regard to safety. Axles are mechanical components whose failure can produce catastrophic consequences, as previously mentioned. The following accidents are examples of railway axle failures for which fatigue failure was the main mechanism.

Accident 1: The first reported accident caused by a broken axle occurred on the line between Paris and Versailles, May 1842.
This accident was the first railway accident resulting in serious damage. In this accident, the driving axle of a four-wheel locomotive was broken suddenly with the resulting death of 100 people. This accident initiated the research and study on the failure mechanisms of railway axles including their wear and fatigue (Figure 2.1) [18].

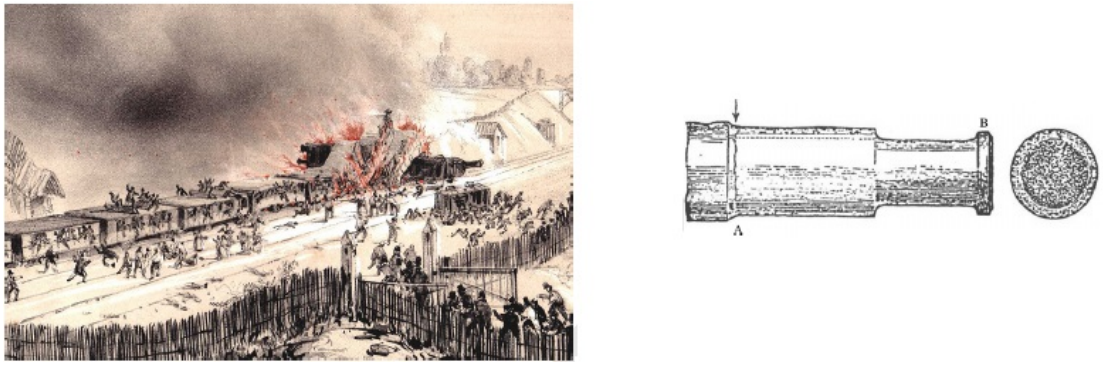

Figure 2.1: *First railway accident which caused major loss of life (left: Meudon accident; right: the sketch of broken axle) [18].*

Accident 2: The derailment of a freight train at Rickerscote, March 1996.
One person was killed and 10 injured in this accident which was caused by a broken axle which was reported as a complete fracture of an axle and consequent derailment of a two-axle freight wagon containing liquid carbon dioxide. The derailed wagons blocked the adjacent line and were run into by a traveling post office train going in the opposite direction. When the broken axle was examined, it was clear that the corrosion pitting increased the stress locally in the axle to initiate a fatigue crack. At the mid-span section of the axle, where the paint had flaked off the surface, there were corrosion pits

mostly about 0.03 mm deep and one about 0.05 mm deep. It is likely that the crack, which initiated from one of these pits, grew and led the failure of the axle into two pieces [19, 20].

Accident 3: Fracture of an axle at Shield Junction, Scotland, January 1998.
The fracture surface of the broken axle was studied, and the results showed that the propagation of two cracks had caused the fracture. The damaged bitumen had allowed the salt solution to come into contact with the surface of the axle and remain trapped there and produce a corrosive environment which increased the local stress. This corrosive environment combined with the in-service mechanical stresses had caused the failure of the axle. The damage caused by the stress corrosion fatigue is more severe than that of corrosion or fatigue loading acting alone [19, 20].

Accident 4: Fracture of an axle caused derailment of the train at Brenerely Junction, June 2002.
The broken axle of this accident had been tested with magnetic particle inspection method to detect any cracks on its surface when it was fitted with a new set of wheels in 1988. Because the axles were grit blasted before inspection using magnetic particles to remove all the rust patches on the surface, the cracks could not be detected and missed [19, 20].

Accident 5: Derailment of Canadian national railways Quebec due to broken axle, Canada, February 2001.
On 15 February 2001, CN train No. G-894-31-14 derailed 25 cars at Mile 12.56 of the Drummondville Subdivision, near Trudel, Quebec [21]. Twenty-four cars were destroyed, together with a main-track switch, the signal system, and 800 meters of track (see Figures 2.2 and 2.3). The derailment was caused by the fatigue fracture in an axle on car CNWX 107921. The fatigue failure occurred at a site where accumulation of moisture created corrosion pitting, which led to the initiation and development of fatigue fractures, and consequently, the axle failure.

Figure 2.2: *Canadian railway accident, February 2001.*

Figure 2.3: *Broken axle of the Canadian accident, 2001, and zoom in the fatigue failure surface.*

At the time of this failure, the fatigue fracture covered over 65 percent of the fracture surface. Initiation occurred at sites with corrosion pitting in the axle journal fillet. While the fracture surfaces were highly oxidized, there were no signs of overheating on any of the components, as mentioned in the accident final report. The corrosion pitting on the axle journal fillets, as well as spalling on the bearing ring, cones and axle roller bearings, indicated that moisture penetrated and accumulated in the area.

Accident 6: The accident of central station in Koln, Germany, July 2008.
In this accident, fortunately, the train derailed as a result of the broken axle when it was running on the switches at very low speed and, therefore, there were no major consequences. This accident affected a driving axle of an ICE3 trainset (see Figure 2.4). An interesting failure analysis is reported in [22].

Figure 2.4: *Broken axle of the IC518 ICE3 train in the Koln main station, 9.7.2008. (left: the broken driving axle seen from the internal side, right: investigators looking at the derailed train [22]).*

Accident 7: The derailment of a freight train in Italy, June 29, 2009.
A less luck case is the axle failure which was responsible for one of the most tragic railway disasters which happened in Europe in the last decade. The freight train 50325 Trecate-Gricignano, composed of a locomotive and 14 tanks carrying liquefied petroleum gas (LPG), derailed in the Viareggio station, Italy, on 29.6.2009 (see Figures 2.5 and 2.6).
The derailment was as a result of the sudden failure of the leading axle of the first wagon. After the derailment, the tank wagon overturned and started leaking LPG which, after a few minutes, caught fire, burning a large area around the railway station, killing 32 people and many more were injured with severe burns [23].

Figure 2.5: *Broken axle that caused the Viareggio accident, Italy, (left), zoom in the fractured section (right).*

Figure 2.6: *Some snapshots of the Trecate-Gricignano derailment accident.*

2.3 Beginning of research in railway axles failure

Because railway wheelsets are safety critical components and their failures can cause derailments, deaths and injuries, as mentioned before, and because wheelsets cannot be duplicated, safety can be obtained only through a severe and rigorous inspection plan with the use of many non-destructive testing technologies, such as Visual Inspection (VI), Magnetic Particles testing, and Ultra-Sonic testing. It should be remembered that the concept of "zero risk" is intrinsically impossible in any mechanical system, i.e. the probability of failure intended as the mathematical function that describes the possibility of occurrence can never be zero. That's why "risk management" is so fundamental for all railway components, especially for axles. Although the useful life of some wheelsets may be rather long (30 years), wheels, axle or bearings may fail in service and need regular checks as well. Definitely, the failure of running axle leads to a derailment, so a special attention has been paid for their conditions.

Axles are historically the weakest component of the wheelset [23]. Meudon accident on 8 May 1842 (the previously mentioned, Figure 2.1) was the main reason initiating the researches performed by August Wöhler, which are still the basis of the knowl-

edge of material fatigue. Stresses reverse every half cycle ("rotating bending") and this makes the axle a component prone to in-service failure. This is why regulations impose that maximum stresses are limited and that materials with well-known crack propagation rules are used. Despite almost two hundred years of development, statistics say that broken axles still represent a quite common event. An interesting report of the ESIS/TC24 [23] indicates that 78 axles were broken in 2006, 103 in 2007, and 104 in 2008. More recent statistics can be found in the 2017 report of ERA on railway safety [24].

In 1848 James and Galton published results of tests on large iron bars subjected to alternating loads as there were known from railway axles [25]. They showed that the loads causing failure were lowered by up to two thirds as compared to static loading in such cases. A few years later, German railway engineer, August Wöhler, started his test series, the results of which were published between 1858 and 1871 [26]. In Figure 2.7, the upper drawing shows Wöhler's apparatus for the measurement of service strains on railway axles. The dashed line indicates the deflected position and the below drawing shows Wöhler's apparatus built for fatigue testing by applying a reserved bending to an axle like a specimen [27].

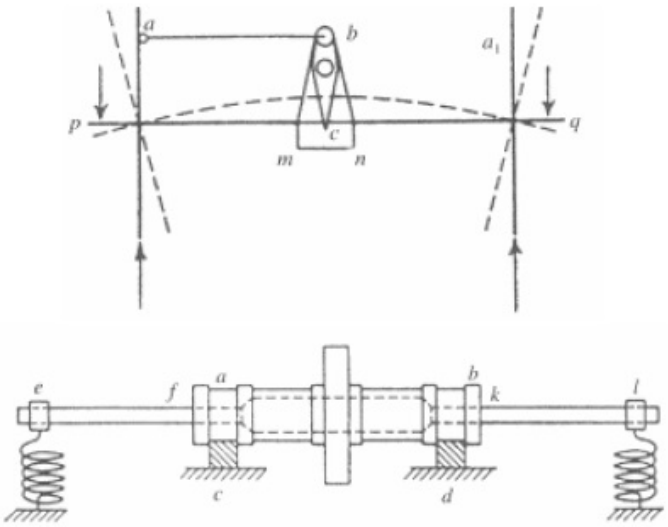

Figure 2.7: *Wöhler's apparatus fatigue testing machine (upper: strain measurements , lower: experiments replicate real loading) [25].*

The development of the S-N (or σ-N, stress versus number of cycles to failure) curve based fatigue design triggered by these early activities was highly important not only for railway applications but for engineering in general [15]. Wöhler led to the identification of the fatigue limit for steels. Despite its long use, there is a growing evidence that for lives longer than the conventional 10^6 to 10^7 cycles, at which the fatigue limit is determined, the safe stress range continues to be eroded down to 10^9 cycles and more, which is at the very long lives typical of that required for axles and wheels. Furthermore, Wöhler's studies clearly identified the benefits of gradual transitions in profile. He also observed fretting initiated failures due to micro-slip between press fitted wheels and axles [26].

Paper [28] analyzed the causes of failure in railway axles to show how the results have been applied to improve axle manufacture and in-service inspection. The paper compared the axles used in Europe and Japan in terms of their fatigue design strategy. The results of stress analysis calculations that were performed for various different North American freight railway axle designs were presented in [29]. Moreover, the paper proposed that a standard axle stress analysis method should be adopted by the North American freight railway industry for new axle designs.

Reference [30] emphasized that in spite of the criticality of axles, modern approaches have not been used in addressing a critical revision of traditional design. In this paper, the scale effects in fatigue limit and in crack growth rate for high strength steel used for high speed railway axles were studied. Two cases of failures in axles and cylindrical roller bearings of a freight wagon servicing for about 30 years were examined in [31]. The examination proved that the failures were caused by fatigue fractures of the inner rings of the bearings. Dynamic strength of bearings was exceeded, then the rings widened and the axle slid in them. Finally, the axle-box housing deformed and breaking occurred. The failed wheel-drive shaft component used on an unmanned, remotely operated vehicle for maneuvering military targets was studied in [32]. This study showed how vulnerable such a rotating component can lead to failure by fatigue.

A method of a fatigue life prediction for railway vehicles based on computer simulation was presented in [33]. In this research, stresses were evaluated in certain bogie cross sections by knowing the forces and predicted the fatigue life by using a cumulative damage theory. Paper [34] presented a design-driven validation approach by employing a Bayesian approach combining data from both physical experiments and the computer model, to develop a prediction model as the replacement of the original computer model for the purpose of design. Moreover, reference [35] presented a single-loop reliability design optimization formulation based on first-order reliability method and an equivalent formulation that can also include system-level reliability constraints.

The need to examine axles arises because of their safety critical nature, as previously introduced. They have been subjected to large numbers of repeated loading cycles. Each time that the axle rotates, an element of material on the surface of the axle goes from a compressive state to a tension state of equal magnitude. Factors such as loading geometry, surface quality, corrosion effect, material failure, being heterogeneous of micro structure, introduce local stress concentration on components. A failure due to fatigue crack can be started from the regions including these stress concentration and then it moves ahead and finally failure occurs, called fatigue fracture. In addition, instead of maximum stress values, the periodic variation (load cycle) of stress becomes important. A brief description of the European Community Standards for railway axle design can be found in [36, 37].

2.4 Hollow and solid railway axles

Railway axles can be grouped as freight wagon axle, coach axle, and locomotive axle. To improve the vibration isolation ability of railway vehicle, the unsprung mass of the vehicle has to be reduced. Lighter unsprung mass gives better ride quality because it can absorb more vibrations than heavier one. Therefore, lighter unsprung masses are required for high performance applications. In order to get light unsprung mass, high

strength materials have to be used which means high cost and high notch sensitivity because high strength materials are considered as brittle materials and in result high strength material is not suitable for railway axles. Another solution is the use of hollow axles instead of solid ones. As well known that, the least stressed part of an axle is its core so boring out the core can improve the strength-mass ratio. Thanks to their reduced mass, hollow axles are one of the key components of the high-speed coach and are used for high-speed vehicles. The two main types of railway axles, solid and hollow, are shown in Figure 2.8.

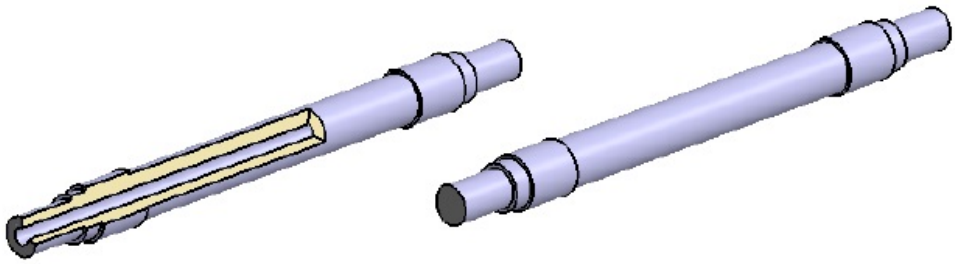

Figure 2.8: *Railway axles (left: hollow axle (half section has been shown for sake of visibility) right: solid axle).*

2.5 Review of railway wheelset inspection methods

2.5.1 Wheelset maintenance

Maintenance is obviously important as it affects life cycle cost, reliability and safety of railway wheelsets. The typical structure of the maintenance cycle of a wheelset consists of mainly three phases:

1. Regular checks in service to look for abnormal defects such as Rolling Contact Fatigue (RCF) defects, and/or bearings overheating.
2. Wheel re-profiling by underfloor lathes in "first level" workshops (typically located in larger depots and spread over a country).
3. Shipment of the entire wheelset to a "second level" workshop (either belonging to the train operating company or an external mechanical workshop) for the complete overhaul when wear has reached its maximum level (e.g. wheels cannot be further re-profiled), running table defects cannot be rectified (e.g. too large wheel flats) or simply because the prescribed interval (time) or life (km) run by the wheelset has reached the limit indicated in the maintenance. Moreover, in this level the scheduled inspections of axles are performing to discover any possibility of a beginning of fatigue cracks.

Second level workshops handle complete wheelsets disassembling the axle-boxes, the bearings, and the wheels from the axle and then performing VI and MP on the axle. US inspection test is generally performed in this level without disassembling the wheelset components. Old wheels are pressed off by cutting or by oil-injection methods, while new wheels are fitted according to press- or shrink-fit and then turned by conventional lathes.

It is evident that this maintenance scheme is well functioning but forces the moving of heavy and bulk wheelsets to specialized workshops where expensive tools and equipments are needed (heating ovens / hydraulic presses, large size lathes). Wheelset maintenance is expensive, time consuming, complex to organize, involves large capital and human resources.

To ensure that wheelset of railway vehicle is operating in proper condition, necessary maintenance as well as monitoring have to be done periodically for critical components of railway wheelsets. Several techniques have been introduced for condition based monitoring of railway wheelsets (e.g. tread condition detectors, wheel profile monitoring systems, wheel impact load detectors, hot axle/hot wheels detector, acoustic bearing detector and brake pad inspection systems).

2.5.2 NDT for railway axles inspection

Railway axles rupture can be initiated from small notches due to various factors such as paint detachment, damage from ballast impacts, pitting from corrosion, fretting fatigue in areas subject to interference fits, and others. This kind of damage can potentially act as an initiation of a fatigue crack, causing final fracture of the axle. Figure 2.9 shows some examples of notches that can be evolved to fatigue cracks. Mechanical damage (like damage from ballast impact) can occur at any time during operation of the axle.

a *b* *c*

Figure 2.9: *Examples of in-service railway axle damage.*
***a**: paint detachment **b**: corrosion pits **c**: damage from ballast impact.*

Possible damage of axles can be initiated from the invisible (inaccessible) areas (like wheel seat, break seat), in this case of damage mostly ultrasonic test are being used. In other hand, cracks start on accessible parts of axle (mostly surface cracks, like ones initiated by corrosion), magnetic particle inspection, ultrasound techniques or eddy currents are used to detect this kind of cracks.
Some existing methods and automated systems of fault detection in wheelsets [13] are briefly presented here:

Ultrasonics inspection techniques

Ultrasonic (US) test uses high frequency sound energy to conduct examinations and make measurements. US inspection can be used for flaw detection/evaluation, dimensional measurements, material characterization, and more. To illustrate the general inspection principle, Figure 2.10 presents a configuration of pulse/echo inspection signal.

A typical US inspection system consists of several functional units, such as the pulser/receiver, transducer, and display devices. A pulser/receiver is an electronic device that can produce high voltage electrical pulses. Driven by the pulser, the transducer generates high frequency ultrasonic energy. The sound energy is introduced and propagates through the materials in the form of waves. Once the wave meets discontinuity (such as a crack) in its path, part of the energy will be reflected back from the flaw surface. The reflected wave signal is transformed into an electrical signal by the transducer and is displayed on a screen. In Figure 2.10, the reflected signal strength is displayed versus the time from signal generation to when an echo was received. Signal travel time can be directly related to the distance that the signal traveled. From the signal, information about the reflector location, size, orientation and other features can sometimes be extracted.

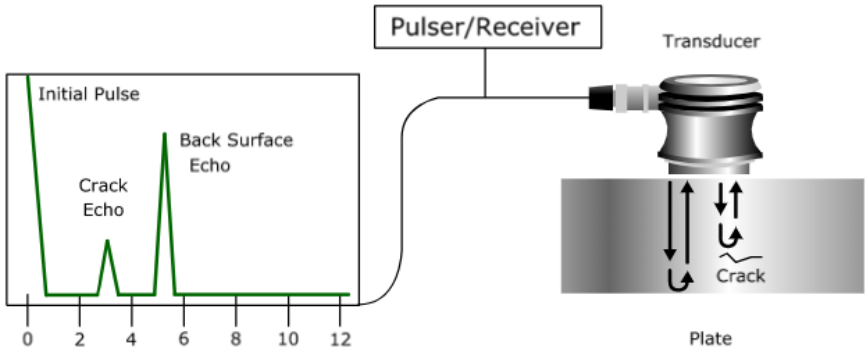

Figure 2.10: *Basic principle of Ultrasonic inspection technique.*

There are well-known techniques of US inspection for railway axles [38] (see Figure 2.11), especially the solid ones:

- "Near end": the probe scans from the end of the axle to the adjacent wheel seat.
- "High angle": scans from the axle surface are used where inspection is required under bearings and wheels, where these have not been removed.
- "Far end": scan was developed to inspect the full length of the axle from one end and is generally applied during overhauls. The signal is very complex and difficult to interpret.
- Rotating probe through bore: This method can be applied for hollow axles as the ultrasonic probe passes through the central bore to scan the axle. This method can be applied by only removing the bearing cover from the sides of the axles (see Figure 2.12).
- Phased array detection: Phased array detection method is an modification of the standard ultrasonic inspection. The difference is in a type of probe used to generate ultrasonic waves. Phased array probe is capable of generating a large number of different ultrasonic beam profiles from a single probe assembly, thus covering a greater area of specimen under investigation. By using electronic control system, ultrasonic beam steering and focusing can be performed decreasing testing time and increasing detection precision (see Figure 2.13).

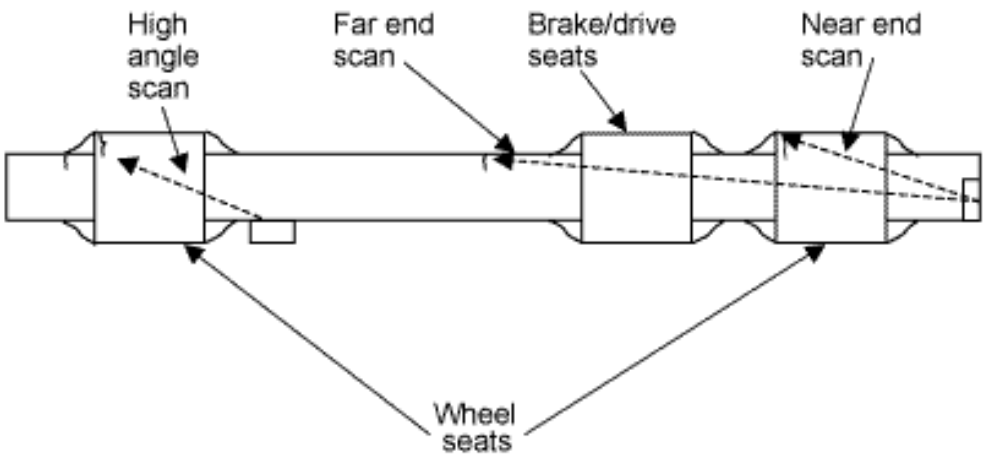

Figure 2.11: *Crack positions and Ultrasonic axle test geometries.*

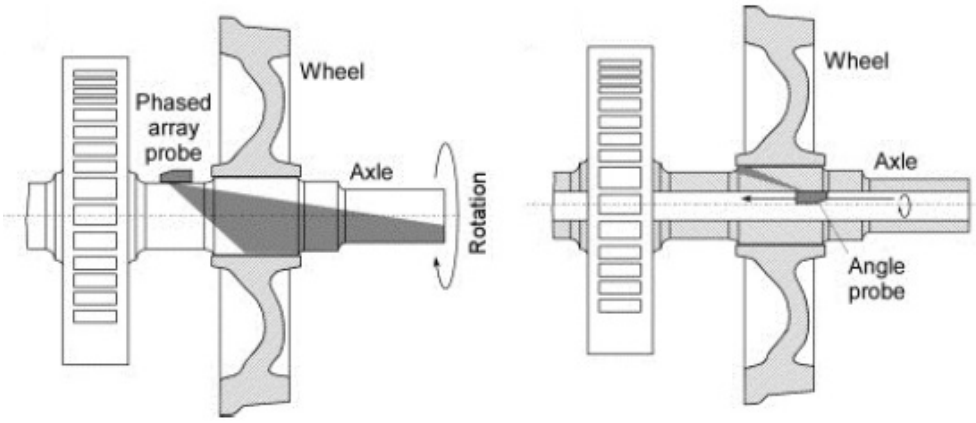

Figure 2.12: *US setup for solid axles (left), US setup for hollow axles (right).*

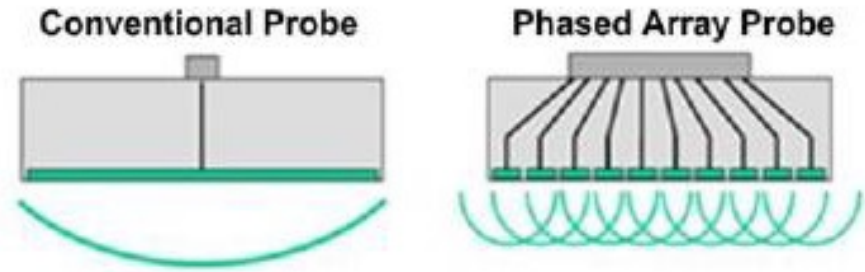

Figure 2.13: *Schematic of phased array probe.*

Inspection system for hollow axle consist mostly a phased array device with a probe. By using motor to drive linear axis for moving the probe axially inside the bore and a PC for device control. This configuration allows reduction of inspection time four times in comparison with conventional ultrasonic method (20 minutes versus 5 minutes respectively), see Figure 2.14.

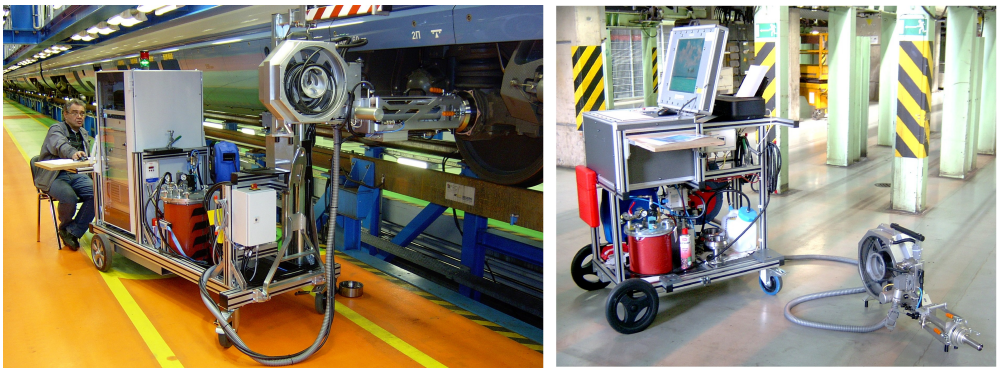

Figure 2.14: *Railway hollow axle testing using phased array probe (Source: Socomate International).*

Generally, ultrasonic inspection is a very useful and versatile NDT method and it has some advantages including:

1. It is sensitive to both surface and subsurface discontinuities.
2. The depth of penetration for flaw detection or measurement is superior to other NDT methods.
3. Only single-sided access is needed when the pulse-echo technique is used.
4. It is highly accurate in determining reflector position and estimating size and shape.
5. Minimal part preparation is required.
6. Electronic equipment provides instantaneous results.
7. Detailed images can be produced with automated systems.
8. It has other uses, such as thickness measurement, in addition to flaw detection.

Ultrasonic inspection also has some limitations, which include:

1. Skill and training is more extensive than with some other methods.
2. It normally requires a coupling medium to promote the transfer of sound energy into the test specimen.
3. Materials that are rough, irregular in shape, very small, exceptionally thin or not homogeneous are difficult to inspect.
4. Cast iron and other coarse-grained materials are difficult to inspect due to low sound transmission and high signal noise.
5. Linear defects oriented parallel to the sound beam may go undetected.
6. Reference standards are required for both equipment calibration and the characterization of flaws.

Magnetic particle inspection method (MP)

Possible surface inspection techniques are penetrant testing, e.g. magnetic particle inspection (MP) and various electromagnetic techniques. MP inspection is a classical NDT technique for surface crack detection where a magnetic field is induced in a component and the magnetic flux leakage at a surface breaking defect is revealed by spraying the component with a magnetic particle ink. The magnetic field may be produced by an electromagnet yoke, by current flow in the specimen or by an encircling coil or adjacent conductor. The magnetic ink may contain black particles (in which case the surface is usually coated with a thin white contrast paint) or the particles may be fluorescent, in which case the item is inspected under ultraviolet light [38] (see Figure 2.15).

Although MP inspection is widely used and is one of the most efficient methods to look for any surface defects, it has some drawbacks. MP inspection needs complete removal of axle from the bogie including the wheels which means time consuming procedure and also, is not so economical. For these reasons this method is used for long term inspection intervals. Other drawbacks during the disassemble of axle components before inspection and re-installation of the components after inspection, rubbing may cause damage to the axle or its components and the axle may become unfit for future use. To perform a MP inspection test, the axle coating which is done for safety against corrosion effects has to be removed from the axle and then it is repeated after the axle inspection [39].

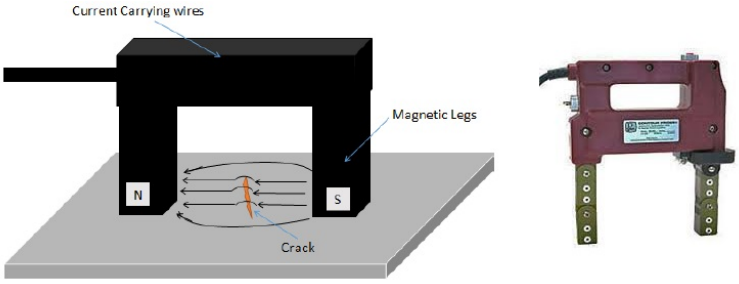

Figure 2.15: *Principle of magnetic particle inspection technique.*

Eddy current inspection

When alternating current is applied to the coil, a magnetic field develops in and around it. The alternating magnetic field generated expands as the alternating current rises to maximum and collapses as the current drops back to zero. The interaction of eddy currents generated in the test piece with any flaws present will cause variations in the secondary electromagnetic field produced by the eddy currents giving rise to impulse changes (see Figure 2.16). Hence, the eddy current effect can be used for crack detection and qualitative evaluation of their severity [40].

Microwave sensor testing

This method is based on a physical phenomenon called the interaction of electron gas and ultrasonic waves in metals. Emission of ultrasonic waves on the metal surface

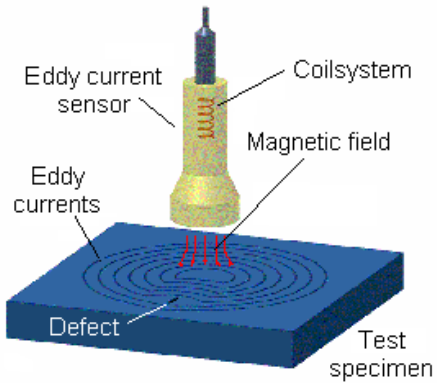

Figure 2.16: *Basic concept of eddy current inspection technique.*

is determined by microwave sensor. Theoretical works showed that there is possible fact to determine remotely dangerous-or-non-dangerous inner metal stress, measuring the surface conduction (density of surface charges) [11]. Research and testing were conducted including remote indicators of active defects on steel samples and railway wheels in static mode as well as dynamic testing in moving mounted wheels. Experiments showed that this new method could be used to determine the initial formation of active defects (cracks), even under elastic tension.

One of the most important advantages of microwave method is the fact that it can be used for detecting surface cracks under dielectric coatings. Because microwave signals easily penetrate inside dielectric materials, this methodology is expected to detect cracks under dielectric coatings of various thicknesses. It must be noted that dielectric coatings such as paint, corrosion preventative substances, etc., may have varied thicknesses although they are generally not very thick and are commonly known as the family of low-loss dielectric materials [41].

AC thermography method

This method depending on passing high frequency electric current through the axle in inspection station. As the current passes through the inspected specimen, a slight heating effect is generated and increased at crack ends, creating hot spots at crack corners, while the temperature decreased at crack centre [12]. The drawback of this inspection method is that it requires no equipment can be located between the camera recording temperature changing and the inspection surface. Also, due to possible interference in temperature reading caused by additional sources (sunlight interference, unexpected sources of heat reflected), this method needs some improvements before applying in larger scale application (see Figure 2.17).

Electro-Magnetic array (EMA)

AC Field Measurement (ACFM) is a surface crack inspection technique developed by TSC inspection systems and is being offered as an inspection technique for various applications by Bombardier. EMA is another electromagnetic surface inspection system operating on a slightly different physical principle to ACFM. It was developed by Newt International and is being offered as a test method by Alstom transport service under

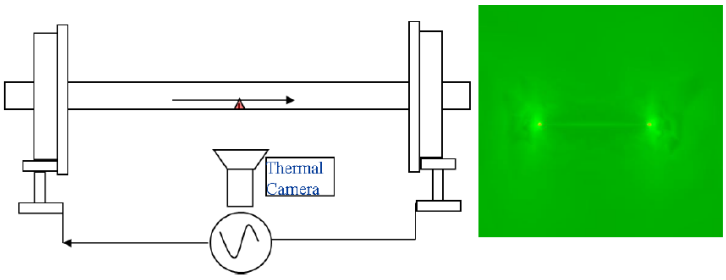

Figure 2.17: *Principle of AC thermography technique.*

the name of EMFaCIS (Electro-Magnetic Metal Fatigue and Crack Inspection Service). In both cases, an inspection probe (or array of probes) induces an alternating current in the surface of the component under test. This produces a magnetic field that is distorted by the presence of a crack. Components of the magnetic field are detected and the equipment displays and records signals that give the length and depth of the defect calculated by comparison with a theoretical model of the electromagnetic fields.

The techniques are relatively insensitive to lift-off and so can be used to test through paint coatings. Another advantage arises from the fact that the data is recorded as the probe is scanned over the component [38]. This means that:
- The scanning can be carried out by less-experienced staff with data analysis by more skilled staff.
- Data is available for further analysis and checking.
- Inspection can be carried out in conditions of poor access, so long as it is possible to manipulate the probe over the test surface.

Laser-based ultrasonic cracked axle detection

For cracked axle detection, this method uses a laser in conjunction with standard ultrasonic transducer to detect faults on the axle of train passing through a testing station. A high-energy, pulsed laser is used to generate ultrasonic modes in the axle and a non-contact, air-coupled transducer to receive the ultrasonic signal emitted by the specimen which is then sent to a signal processing unit for analysis to determine the presence of cracks across the axle circumference [41]. Each inspection is capable of detecting circumferentially oriented cracks across the body of the axle. By repeating the inspection multiple times around the circumference of the axle, it is possible to detect cracks around the entire axle body. The automated cracked axle detection system consists of 10 inspection stations, which inspect the axle for cracks greater than 7 [mm] long [41].

High frequency vibrations

System based on high frequency vibrations analysis detects cracked axles through the use of compensated resonance, by exciting the axle with an impact and measuring the resulting vibration with an accelerometer in contact with the axle. Changes in the high-frequency components of the vibration indicate the presence of a crack [41].

Acoustic emission (AE)

When the damage develops in a material, ultrasonic elastic waves are formed as a released energy. Acoustic Emission (AE) method is based on observing these waves as shown in Figure 2.18. In railway field, AE tests are being introduced mostly for investigating the state of a bogie bolster, monitoring the state of rail defects and for acceptance tests of bearing races but research effort is put on possible application in railway axles monitoring. Tests conducted on railway axle showed that sensors are capable of sensing fracture of the axle, given that appropriate signal processing is used (achieved with wavelet de-noising techniques) [41].

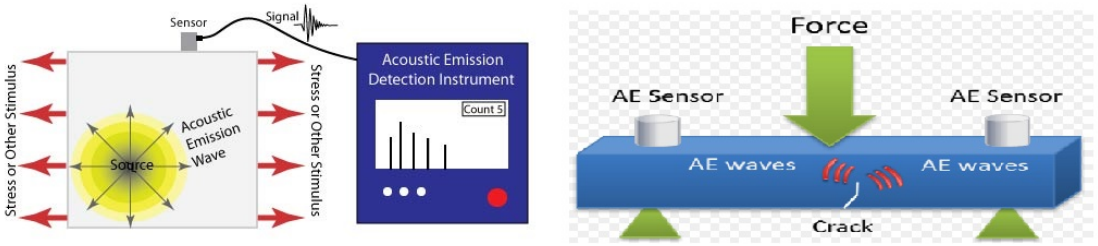

Figure 2.18: *AE theory principle and its application in crack detection.*

2.6 Modern approaches of railway axle integrity

Any non-destructive technique has a detection threshold, i.e. the minimum size of the defect that can be observed in practice. US devices used for axle integrity checks are calibrated by using sample defects machined on a specimen made of the same material as the axle to ensure exactly the same ultrasonic characteristics of the steel. As with any other experimental, non-destructive technique, US supplies information (known as "indications") with a degree of uncertainty. This means that the so-called Probability Of Detection (POD) depends on many factors [23]. An interesting work in the application of the POD approach to railway axles can be found in [42].

Although deterioration progresses continuously, no on-board monitoring techniques are currently available to check in real-time the propagation of axle cracks. They can only be inspected at predetermined intervals. In case a crack of the size below the detectability threshold is present at a certain inspection, the interval should ensure that this crack does not propagate, breaking the axle before the following inspection (see Figure 2.19). As mentioned before, the consequences of a misconducted NDT testing or an underestimated crack propagation law can be tragic.

Axle fatigue fracture is always brittle and sudden, despite the fact that the steels for axles have a rather limited ultimate tensile stress and a high ductility. The analysis of fractured surfaces shows that this is the one typical for shafts subjected to rotational bending under low nominal stresses and mild stress concentrations.

The failure mechanism of railway axles can be described as illustrated in Figure 2.20, where the crack started from a small notch where there is a concentration of stresses. With the repetition of stress cycle, the crack starts propagating incrementally in a plane perpendicular to the axle axis (transverse crack) causing decrease in the resistant cross-section area at the failure plane and therefore, increase its stresses due to the increase of

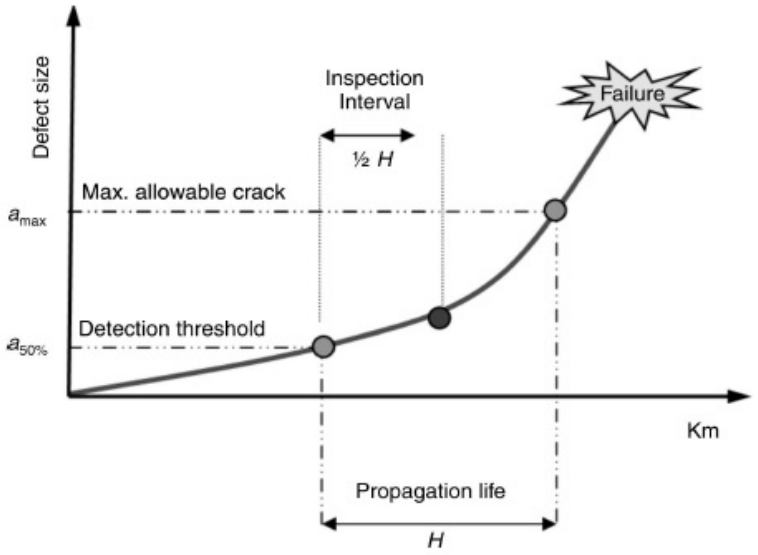

Figure 2.19: *Crack propagation curve and inspection interval definition [23].*

stress concentration factor. The crack propagation rate increases exponentially during the crack life till final failure occurs very rapidly when the advancing crack reaches a critical size where the cross-section cannot withstand the stresses leaving a very rough surface, see Figures 2.5, 2.20 and 2.21.

Failures generally happen in transition zones where there is a change in the cross-section. That's why the design of fillets and abutments is somewhat critical in axle design and integrity. From failure analysis, it is interesting to mention that torsion stress does not play an important role in fatigue failure, even in driving axles [10].

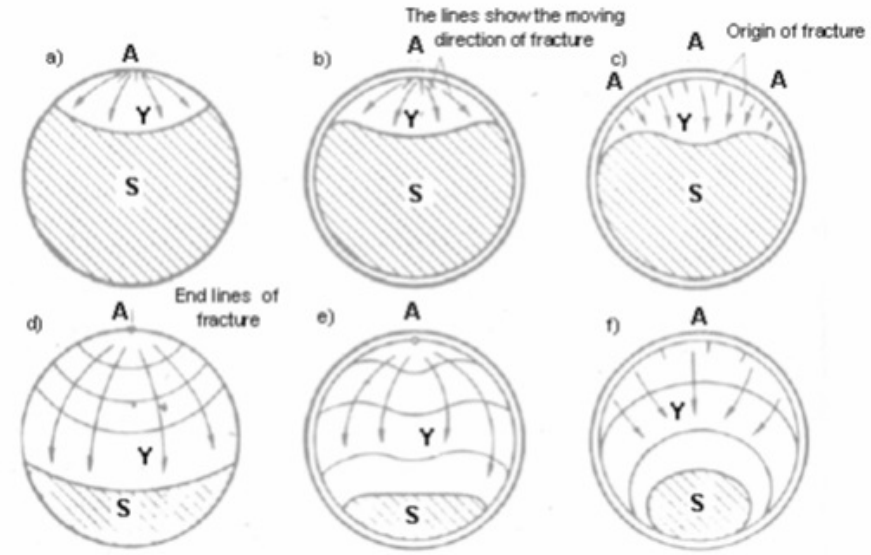

Figure 2.20: *Schematic of crack propagation on surfaces of smooth and notched shafts under various loading conditions [23].*

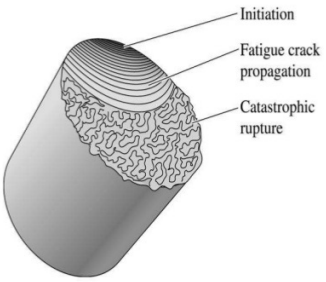

Figure 2.21: *Schematic representation of a fatigue fracture surface in a steel shaft.*

The detection of cracks in railway axles is carried out by a variety of NDT methods, as previously introduced. The POD represents the effectiveness of the inspection, and is a quantity needed, together with crack growth rates, to determine inspection intervals to avoid in-service failures [38].

2.6.1 Probability of detection (POD)

POD data is used, in combination with crack growth data, to give an optimum inspection intervals for a given component in service. The interval is set such that an in-service defect which the NDT system would miss cannot grow to a size likely to cause failure before the next inspection (Figures 2.19 and 2.22). Obviously, more sensitive inspection techniques, which detect smaller defects, will give high probability of detection with small flaw size.

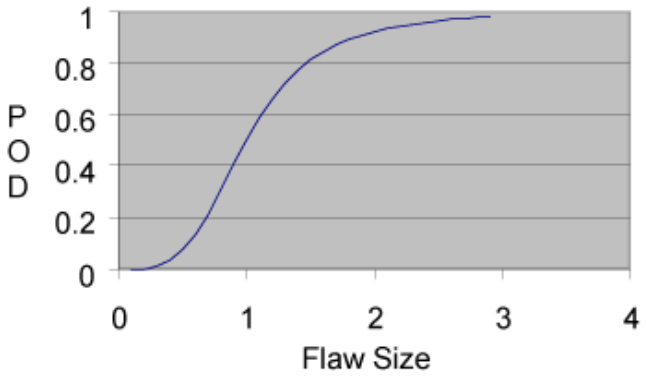

Figure 2.22: *General shape of POD curve.*

The establishment of the POD of a particular inspection can be carried out experimentally, with the help of some theory or by 'expert judgement'. The experimental method is basically a task of providing a sample with a known set of flaws, measuring the number detected by a technique compared with the number present. However the performance of a non-destructive testing technique is closely related to the procedure used and the particular component under test. The cost of providing flawed samples usually prohibits the number of trials that can be carried out. The practice of carrying out measurements to establish the POD is therefore constrained by this situation and there are well established practices which need to be followed. These methods have been generally established by the United States aircraft industry [38].

Theoretical modeling can be used if the theory available accounts for the various flaw geometries and properties and allows for operator error. Usually, however some support from experimental methods is useful, expert judgment is frequently used to relate PODs known of a particular technique known in one situation to those in another similar one [38]. Comparison of POD curves is quite difficult because the curves may have different shapes and minor changes in procedure can cause significant changes in POD. For simplicity the flaw size for POD at 90% is often used for comparison. A set of POD curves used for determination of inspection intervals on railway axles is given by [43].

2.6.2 High strength axles

Railway axles are historically produced according to UIC standard 811 [44], which originally specified five steel grades (A1=C35, A2=22MnCrV5, A3=C45, A4=25CrMo4, A5=42CrMo4). European standards on axles were later developed by CEN for design (EN 13103 / EN 13104) and for manufacturing (EN 13261) including only A1 and A4 steel grades. The design of axles is based on EA1N for which fatigue limits and safety factors are available, while adjustments are described in order to evaluate the safety factor and permissible stresses for other steel grades (EA4T and EA1T). Alloying and thermal treatments are common methods to obtain steels with better performances, this allows the design of optimized components.

Fiat Ferroviaria (today Alstom Ferroviaria), in the 70s started developing the well-known and successful Pendolino trains family for Italian Railways, proposed to use the high strength alloyed steel 30NiCrMoV12 [23] to design an optimized axle, achieving a substantial mass reduction. According to [36], a reduction of more than 20% in the axle mass can be obtained designing an axle with 30NiCrMoV12 instead of A4T, and more than 30% instead of A1N. A comprehensive description of the properties and the advantages offered by this steel is also presented in [36]. On their side, German Railways, DB, made use of 34CrNiMo6 alloyed steel for the driving axles of the ICE3 train (trailing axles are made of A4T). The design procedures of railway axles running on the European network can be found in [36]. In addition, this reference introduces the European rules and requirements for technical homologation of a new axles and the properties of standard steels for axles.

2.7 Dynamics of cracked rotors

The molecules of rotating shafts working under cyclic loads are subjected to stresses changing between tension and compression. Due to these conditions of loading, cracks can be started from tiny notches (Figure 2.9) and developed causing failure in mechanical components (see Figures 2.5, 2.20 and 2.21). This type of cracks is so called transverse crack where the crack propagates in a plane perpendicular to the rotor axis.

Crack existence and its dimensions are investigated commonly by means of non-destructive tests, as mentioned before, but crack detection is much difficult in case of rotating element during its operation, especially when compared with stationary structures. In case of rotating shafts working in field of turbomachinery (e.g. power plants), dynamic tests, based on vibration measurements, are suggested for identifying presence and location of cracks as the change in the overall dynamic behavior might be caused

by the local reduction of the stiffness due to a crack that has developed somewhere in the structure [41].

Vibrations analysis has been found to be a proper technique to extract symptoms justifying developing fault in a component under investigation. If these symptoms are found and they are giving the right to suspect fault existence which is putting threat to system safe operation, then maintenance activities might be planned with minimized interruption in machine working schedule [41]. Generally, the dynamic behaviour of the system will change due to a crack existence but in practice it has been found that small size cracks cannot make such sufficient change to the dynamics of machine system that they can be virtually detected by this means. Only if the crack grows to a potentially appropriate size can they be readily detected. It's kind of race between fault detection and machine degradation [45].

2.7.1 Crack propagation in rotating shafts

For better design and prediction of rotating shafts, crack propagation rate and its path models are continuously developed for more accurate investigation [46]. Fracture mechanics concepts play key role in modeling, analyzing and interpreting results of analysis of fatigue crack propagation. After a lot of researches in crack propagation, it was concluded that the crack propagates deeper inside element structure due to high stress intensity factors (SIF) at the crack tip even with constant external loads. As shown in Figure 2.19, the propagation rate in rotating shafts change from case to case where the crack propagates slowly in the first stage to relevant depth, afterward, the propagation rate increase rapidly to a critical dangerous depth within few days of machine operation. Cracks in railway axles generally propagate in a plane perpendicular to the axle axis, taking the name of "transverse cracks".

2.7.2 Crack breathing mechanism

The constant direction of rotating shaft weight and acting loads lead to have compression stress in one side of its cross section and tension in the other side. When the crack position is in the compression side, the crack will be fully closed. Once the crack or part of it becomes in the tension stress region, the crack starts opening gradually depending on its angular position until the crack walls become fully open. This process is repeated every axle revolution causing a periodic crack opening and closing, thus giving rise to the actual breathing mechanism phenomenon. Therefore, as a result of changing of crack angular position with respect to the load direction, in rotating shafts, the crack surfaces conditions change between fully opened and fully closed, which called " Crack Breathing Mechanism".

Because the static deflection of the shaft is much greater than the deflection due to the dynamic response of the cracked shaft, the crack breathing mechanism is controlled by the shaft angular position [41, 47]. The propagation of transverse crack in rotating shaft causes a change of the local flexural stiffness. During a complete revolution of the shaft, the breathing mechanism causes periodic changes of the area moments of inertia of the cracked section which lead to variations in local stiffness. The consequent periodic changes of the local flexural stiffness of the axle significantly affect the synchronous and super-synchronous vibrations of the shaft where the stiffness variations are causing additional deflections of the shaft even if load amplitude remains constant

that can be expressed by an adequate number of harmonic orders of a Fourier series (NxRev) frequencies [41].

The crack breathing mechanism was investigated in detail in [10] using experimental tests as well as simulation results. The breathing mechanism can be modelled using different approaches as introduced in [10]. The most accurate model of crack breathing mechanism is based on the Finite Element method using solid elements. This model is considered as a reference for any other models. Moreover, vibration related to a crack in turbomachinery has been investigated in [10] and examples of measured vibration levels increased due to crack propagation in rotating shafts of power plant turbomachinery are presented in this reference.

2.7.3 The effect of crack shape on rotating shaft vibration

Because the crack with rectilinear tip is the common in the models of shafts with transverse crack while real cracks may have different shapes (mostly convex elliptical), a comparison was introduced in [10] to study the effects of cracks with different tip shape on rotating shaft vibrations. Two crack shapes (rectilinear and elliptical) with equal cracked area were modeled and the vibrations related to breathing mechanism were calculated during a run-down transient of the shaft where the two cracks were considered in the same position. The simulation results revealed that the effects caused by elliptical cracks on shaft vibrations can be considered equivalent to those caused by rectilinear cracks, providing that the same cracked area is assumed. 2xRev component, the most significant symptom, is equal for both crack shapes and the differences in the other harmonic components (1xRev and 3xRev) are negligible [10].

2.8 Proposed approach for continuous SHM of railway axles based on vibration measurements

Most of the inspection methods of railway axles, presented in Section 2.5.2, need to build wayside inspection stations through which the trains can pass during the operation or require gaining access to the axle body by dissembling some components which means loss of money, efforts and time. Despite the high standards of present engineering practice in non-destructive inspection tests of axles, fatigue-induced in-service failures of railway axles still occasionally occur, representing a serious threat to the safe operation of railway systems. Therefore, the implementation of continuous structural health monitoring (SHM) techniques plays a pivotal role in further reducing in-service failures of railway axles.

Due to the lack of online systems collecting real-time data which can be used as continuous monitoring systems of railway axles operating conditions, the scope of this work is to introduce a new approach, which is new in railway field, using the change of the axle bending deflection, low frequency vibration (LFV) signal, to monitor the axle condition regarding the presence of a crack.

The proposed SHM strategy aims to measure the first three harmonic components of axle bending vibration. This strategy has been successfully applied in the past to the detection of cracks in turbine shafts [10, 48]. However, in the case of railway axles the detection of NxRev components is more problematic due to some additional issues such as:

1. Railway axles are rotating at speeds well below their first critical speed, which means low vibration amplitude related to a crack will be obtained, whereas shafts in turbomachinery and other industrial machinery are often working above at least the first critical speed.
2. The high level of disturbance generated by track irregularity and wheel out-of-roundness (OOR) disturbance. Indeed, the level of vertical axle-box acceleration caused by track irregularity can be in the range of 500 m/s^2 whereas the amplitude of the acceleration caused by the crack is in the order of magnitude of 1 m/s^2. Wheel OOR typically causes lower amplitudes of axle-box acceleration compared to track irregularity, but the component of the signal caused by this disturbance is periodic with the wheel turn, therefore, providing the same NxRev components caused by crack breathing mechanism, so that this disturbance cannot be separated by the use of synchronous averaging [49].
3. The angular speed of the railway axle is changing in complicated way which means that the vibration signal obtained from cracked axle will be non-stationary signal.
4. Because the axle not only transferring the load but also provides a support for other auxiliary systems, e.g. traction motor and brakes, limited sections can be used to measure the effect of a crack presence.

These challenges are addressed in the next chapters by different research activities where different Finite Element models for railway cracked axles have been constructed to study the influence of a crack presence on the axles dynamics with considering different crack locations, sizes and different types of irregularities. These models were validated by experimental results obtained from tests carried out on a full-scale railway axle specimen performed using the Dynamic Test Bench for Railway Axles available at the labs of Politecnico di Milano.

The SHM technique proposed in this thesis takes into account properly the effect of disturbances associated with train-track interaction, track irregularity, track flexibility and wheel OOR disturbance. For this purpose, a multi-body (MB) model of a railway vehicle also considering track flexibility is merged with a Finite Element model of one cracked axle to form a detailed model of a railway vehicle with one cracked axle. In this model, called MB-FE model, a model of crack breathing mechanism is considered depending on the crack size and location. This model is used to evaluate the NxRev components of axle vibration occurring in presence of cracks having different positions along the axle as well as different depths. In addition, a simple definition for crack detection threshold depending on the obtained numerical simulations results is defined.

After examination of the State of the Art, the cracked axle vibration signal has been tested using different signal processing techniques and a suitable technique able to deal with non-stationary and noisy signals, which are representative of signals obtained from railway field, is introduced. Moreover, different tacho-less techniques have been tested and a new tacho-less technique suitable for railway continuous SHM applications is proposed.

CHAPTER 3

Finite element models of railway cracked axle and laboratory tests

This chapter deals with the modeling techniques used to predict Low Frequency Vibration (LFV) caused by the breathing mechanism of a cracked axle subjected to rotating bending load. Moreover, the chapter reports about the validation of the models using three point rotating bending load test. In this chapter, two Finite Element models are considered: the first one was created using solid (3D) elements included in commercial software ABAQUS/CAE, this model allows a very precise description of the mechanical properties of the flexible axle and of the non-linear behaviour of the crack, but requires a large computational effort. To overcome this problem, a second simpler model of the cracked axle is defined using Timoshenko's beam element (Beam FE model). In this model, the effect of crack breathing mechanism is introduced by means of a special element whose stiffness properties are varied periodically with the rotation of the axle. The Beam FE model was coded in MATLAB and verified with solid model results and experimental results. After verification, different crack sizes at different locations were simulated for different boundary conditions of the railway axle.

3.1 Geometrical shape of railway axle

Two types of railway axles were modeled, one hollow and one solid axle. A hollow configuration with 0.169 m cylindrical body diameter, 0.065 m bore diameter and 2.25 m total length, which is typically the one used in passenger trains, was considered. A solid configuration, as shown in Figure 3.1, with 0.16 m cylindrical body diameter and 2.25 m total length, which is typically the one used in freight trains, was modeled. These configurations were defined according to technical documentation delivered by axle manufacturer.

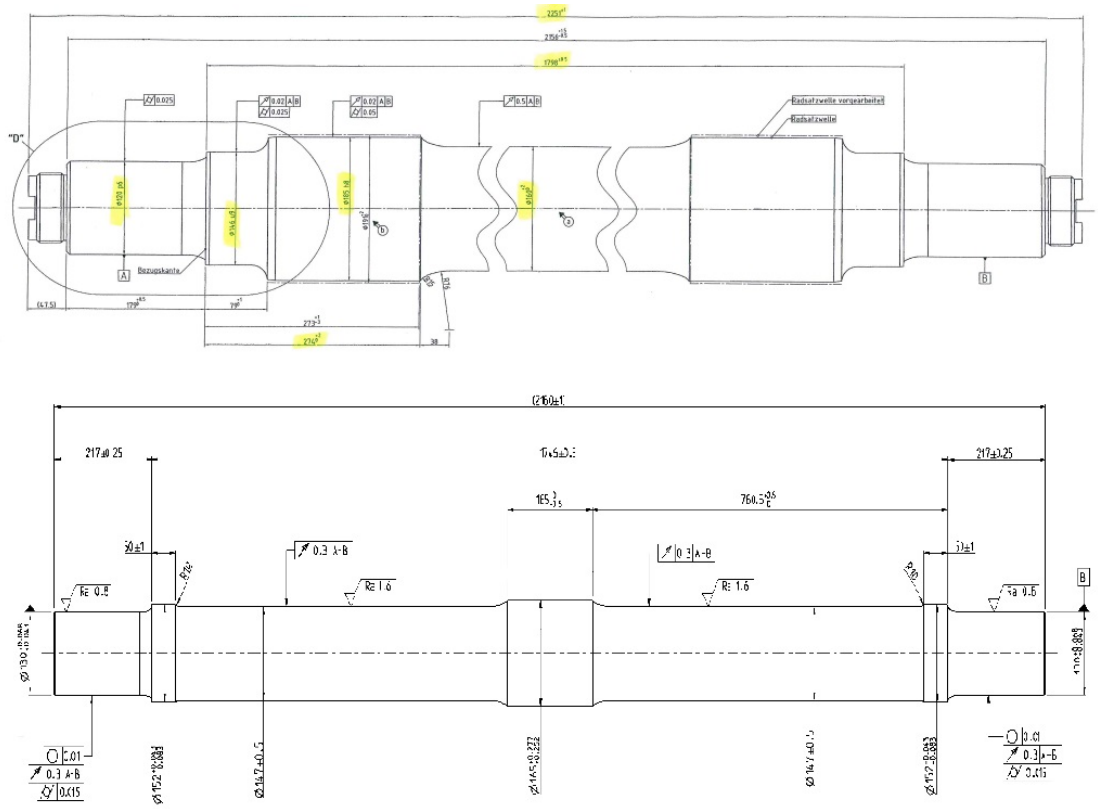

Figure 3.1: *Solid axle configuration,*
(upper: typical railway axle dimensions, lower:axle specimen used in the experimental tests).

3.2 Axles solid FE models using ABAQUS/CAE

3.2.1 Cracked axles solid FE models

In cracked axle model, a crack with specified size and location has to be defined. To reduce size and number of finite elements used in solid FE model, the elements were simplified in transition zones of the axle while due to the crack breathing mechanism is the most important phenomenon has to be investigated by the simulations, care was taken to ensure a proper mesh of the FE model in the cracked region, see Figure 3.2 where the crack was introduced at the middle part of the axles as an example.

Because the effects caused by elliptical cracks on shaft vibrations can be considered equivalent to those caused by rectilinear cracks for the same cracked area [10], cracks having rectilinear shape of the tip were considered in these models. The model consists of different sections to represent locations of boundary conditions, loads, and measuring points. A complete 3D model for hollow and solid axle are presented in Figure 3.2.

Axles material properties were defined according to parameters of A1N grade steel, from which axles were produced [5], where its mechanical properties are:
Elastic modulus = 210 [GPa], Poisson ratio = 0.26 [-] and density = 7300 [kg/m^3].

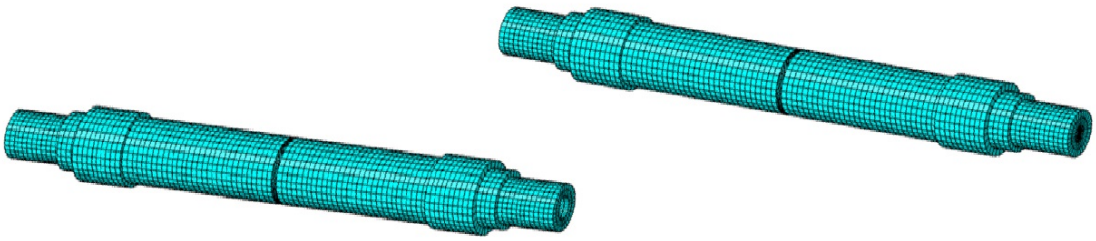

Figure 3.2: *ABAQUS 3D model for hollow and solid axles (crack at middle part of the axles).*

3.2.2 Analysis Type

ABAQUS introduces several analysis types which are divided in two main groups: general and linear perturbation. In ABAQUS/CAE, different analysis types are managed under the step module. The general analysis can deal with both linear and nonlinear effects. If nonlinear effects are expected, such as the crack breathing mechanism, the *NLGEOM* command should be activated [50]. Due to nonlinearity coming from crack surfaces contact during axle rotation, dynamic explicit analysis in double precision was used. Abaqus/Explicit was chosen because it is more efficient than Abaqus/Standard for solving contact interactions [50].

The dynamic explicit analysis available in ABAQUS/Explicit was used with short dynamic response time and extremely discontinuous processes and allows general contact conditions. The dynamic explicit solver performs a large number of small time increments efficiently using an explicit central difference time integration method. In this method, each increment is relatively inexpensive compared to the direct-integration method because there is no solution for a set of simultaneous equations.

The explicit central difference operator satisfies the dynamic equilibrium equations at the beginning of the increment, t and the accelerations calculated at time t are used to advance the velocity solution to time $t + \Delta t/2$ and the displacement solution to time $t + \Delta t$. The stability increment limit is given in terms of the highest frequency of the system as $\Delta t \leq 2/\omega_{max}$, but when introducing damping to the system, the time increment is calculated as:

$$\Delta t_{stable} \leq \frac{2}{\omega_{max}}(\sqrt{1+\zeta_{max}^2} - \zeta_{max}) \tag{3.1}$$

where, ζ_{max} is the damping coefficient in the mode with the highest frequency. An approximation to the stability limit can be written as the smallest transit time of a dilatation wave across any of the elements in the mesh, $\Delta t_{stable} = \frac{L_{min}}{C_d}$, where L_{min} is the length of the smallest element in the mesh and C_d is the wave speed of the material [50]. The shorter the element length, the smaller the stability limit. The wave speed is a property of the material as: $C_d = \sqrt{\frac{E}{\rho}}$, where E is Young's modulus and ρ is the material density. For example, if the smallest element dimension is 5 mm and the dilatation wave speed is 5000 m/s, the stable time increment is on the order of 1×10^{-6}s.

3.2.3 Cracked axle mesh

The axles were discretized using second-order interpolation, reduced integration C3D8R elements. These elements are using one Gauss integration order less than required

for exact integration of strain energy density over element volume to obtain element stiffness matrix, this lead to lower computational time and increase flexibility of such element, thus decreasing shear locking in certain problems [41, 51].

Reduced integration elements have major drawback, the hourglass effect, this drawback is happening during stiffness calculations scheme causing mesh instability [50]. Effective method to control this phenomenon is the enhanced hourglass control formulation, which was used in these 3D solid models. It is a robust formulation based on enhanced strain methods and not requiring user-set parameters. The enhanced hourglass control formulation also provides highly accurate results for elastic bending in the presence of coarse mesh [50], and this advantage was used to reduce mesh density in regions located in a distance from crack, allowing further reduction in total calculation time.

Sweep technique with advancing front algorithm was used to mesh the cracked axles. Since the crack-breathing mechanism is the most important phenomenon to be investigated by the simulations, care was taken to ensure a proper mesh at the cracked region by refine the mesh at this region, as presented in Figure 3.2.

3.2.4 Contact between crack surfaces

There are two types of contact algorithms in ABAQUS/Explicit: kinematic and penalty method. The kinematic contact method does not allow any penetration of the contact elements while the penalty method does. When defining a contact between two surface, one serves as a slave surface and the other one as a master. The crack surface contact was defined as a time-dependent boundary condition which had to be calculated at every time step.

Contact between crack surfaces was set with a penalty friction formulation with the friction constant $\mu = 0.2$ [10] in the tangential direction. In the normal direction the contact was set with hard contact, in this approach when no contact is detected at surfaces where the crack is open, zero pressure is set. As soon as condition is changed with crack closure, surfaces start to be in contact, constraint enforcement is applied and contact pressure is increased. The contact was performed with a surface to surface contact method which has many advantages which can be used in application of crack breathing mechanism analysis [50].

3.2.5 Damping model

The function of damping is to dissipate energy and push the amplitude of the vibration to decay with time. Viscous damping applies forces to the structure proportional to velocity but oppositely directed. Unfortunately, the common sources of damping are not viscous and are neither easy to measure nor as easy to represent mathematically as viscous damping [52]. These sources include "internal friction" in the material and Coulomb friction in connections, neither of which exerts forces proportional to velocity. Fortunately, damping in structural problems is usually small enough that it can be idealized as viscous. Indeed, damping forces $C\dot{x}$ (C: damping matrix, $\dot{x}$: velocity vector) are usually well below 10% of stiffness forces Kx (K: stiffness matrix, x: displacement vector), inertia forces $M\ddot{x}$ (M: mass matrix, $\ddot{x}$: acceleration vector), and external forces. Typical values of damping ratio ζ range from about 2% for piping systems to about 7% for bolted structures and reinforced concrete [52].

Two approaches are often used to include viscous damping in FE analysis: proportional damping and modal damping. In this model, proportional damping, also called "Rayleigh damping", was applied. Proportional damping refers to the following arbitrary and nonphysical definition of the damping matrix:

$$C = \alpha M + \beta K \tag{3.2}$$

Assuming linear viscous damping focusing on Rayleigh damping, the damping ratio for the n-th mode of a system is:

$$\zeta_n = \frac{\alpha}{2}\frac{1}{\omega_n} + \frac{\beta}{2}\omega_n \tag{3.3}$$

The meaning of this definition, in terms of the damping ratio ζ, is shown in Figure 3.3. Values of ω_1, ω_2, ζ_1 and ζ_2 are chosen depending on the range of interested frequencies and required damping ratio.

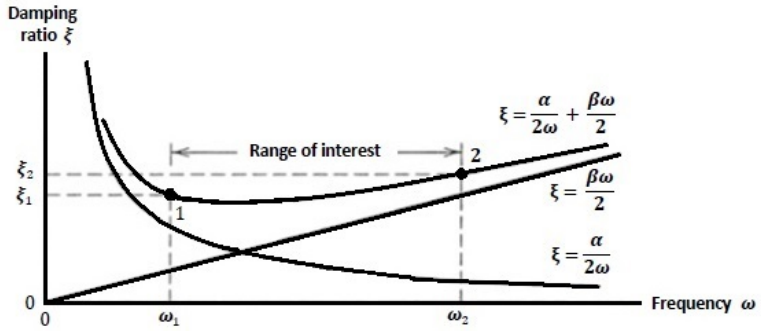

Figure 3.3: *Fraction of critical damping for the proportional damping scheme [52].*

By simultaneous solution of the following two equations:

$$\zeta_1 = \frac{\alpha}{2}\frac{1}{\omega_1} + \frac{\beta}{2}\omega_1 \quad , \quad \zeta_2 = \frac{\alpha}{2}\frac{1}{\omega_2} + \frac{\beta}{2}\omega_2 \tag{3.4}$$

With α and β, damping matrix C is established. With this definition of C, one must accept the curve between point 1 and 2 in Figure 3.3 as a satisfactory representation of damping over the frequency range of interest, i.e. $\omega_1 < \omega < \omega_2$. While this representation may be acceptable, it cannot be physically correct because it demands infinite damping at $\omega = 0$. The form αM damps lower frequencies more heavily and the form βK damps higher frequencies more heavily.

Damping effect on Abaqus/Explicit stable time increment

As the damping coefficient for the highest mode (ζ_{max}) increases, the stable time increment in Abaqus/Explicit decreases according to Equation 3.1. By substituting $\omega_2 = \omega_{max}$ in Equation 3.4, the frequency of the highest mode, ζ_2, becomes ζ_{max}. Equation 3.4 indicates a tendency for stiffness proportional damping coefficient (β) to have a greater effect on the stable time increment than mass proportional damping coefficient (α), this equation demonstrates that it is generally preferable to damp out low

frequency response with mass proportional damping (αM) rather than stiffness proportional damping (βK). However, mass proportional damping (αM) can significantly affect rigid body motion, so large α is often undesirable.

To avoid a dramatic drop in the stable time increment, the stiffness proportional damping coefficient (β) should be less than or of the same order of magnitude as the initial stable time increment without damping ($\Delta t_{stable} \leq \frac{2}{\omega_{max}}$) [50]. As previously introduced, an approximation of the stability limit is often written as the smallest transit time of a dilatational wave across any of the elements in the mesh as:

$$\Delta t_{stable} \simeq \frac{L_{min}}{C_d} \tag{3.5}$$

This estimate for Δt_{stable} is only approximate and in most cases is not a conservative estimate. In general, the actual stable time increment chosen by Abaqus/Explicit will be less than this estimate by a factor between $\frac{1}{\sqrt{3}}$ and 1 in a 3D model [50]. The time increment chosen by Abaqus/Explicit also accounts for any stiffness behavior in a model associated with penalty contact [50].

Because of the use of very refine elements at cracked section to reproduce the breathing mechanism effect, time stability problem, caused by the stiffness proportional damping coefficient (β), appeared in simulations of cracked axle with Abaqus/Explicit solver. In Abaqus/Explicit a small amount of numerical damping is introduced by default in the form of bulk viscosity to control high frequency oscillations. Bulk viscosity introduces damping associated with volumetric straining. Its purpose is to improve the modeling of high-speed dynamic events. Abaqus/Explicit contains two forms of bulk viscosity, linear and quadratic. Linear bulk viscosity is introduced to damp "ringing" in the highest element frequency. This damping is sometimes referred to as truncation frequency damping. It generates a bulk viscosity pressure that is linear in the volumetric strain rate. Linear bulk viscosity damping coefficient is equal to 0.06 by default [50]. The second form of bulk viscosity pressure is quadratic bulk viscosity and is found only in solid continuum elements. Quadratic bulk viscosity damping coefficient is equal to 1.2 by default [50].

To overcome the deterioration of time stability in cracked axles solid models, stiffness proportional damping coefficient (β) has been eliminated. A combination of Rayleigh damping with mass proportional damping coefficient (α) equal to 3, to damp the low frequencies, as well as bulk viscosity, to damp high frequencies by using Linear bulk viscosity damping coefficient equal to 0.2 and Quadratic bulk viscosity damping coefficient equal to 2, was used.

3.2.6 Loads and boundary conditions

Three different cases of loads and boundary conditions are considered and modeled for both solid and hollow axle:

- **"First case"** model; in this case, three points rotating bending load was modeled to represent the full-scale specimens used in experimental tests. Cracked axle experimental tests have been carried out using the Dynamic Test Bench for Railway Axles (BDA) available at the labs of Politecnico di Milano-Department of Mechanical Engineering. The experimental tests are introduced in Section 3.4 . In

this case, the load is defined at the central part of the axle to represent the same load condition used in laboratory tests in which 170 kN load was applied vertically to the middle part of the axles models, as shown in Figure 3.4. Two types of boundary conditions (BCs) were applied, namely displacements and rotations localized at the wheel seats. In this case, the BCs are defined to consider the axle simply supported by perfectly rigid bearings. Therefore, the displacements of the axle are constrained in x, y and z directions at one wheel seat and in x and z directions at the other wheel seat, whilst the rotations around these axes are considered completely free at both wheels.
To apply the axle's angular speed, a kinematic coupling was defined between the wheel seat area on one side of the axle and a suitably created reference point. The angular speed prescribed to the reference point is thereby transferred to the surface of the axle, thus producing axle's rotation according to user-specified parameters (constant or variable speed). The axle's angular speed was set to 592 rpm, approximately the same speed used in the laboratory tests (see Figure 3.4). The crack was

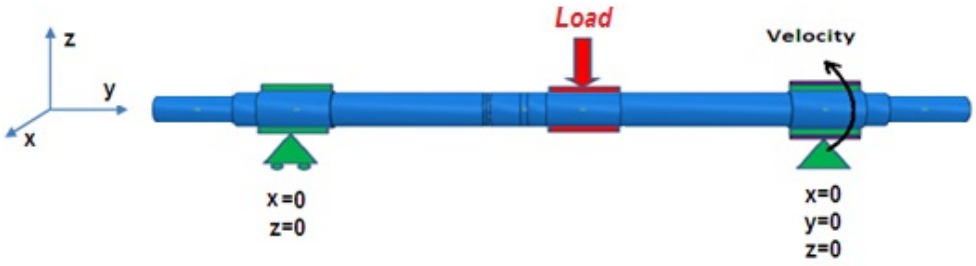

Figure 3.4: *"First case" model to represent laboratory tests.*

located close to the axle center section same as in the experimental tests. Different crack sizes are modeled and simulated and the results are compared with the experimental results to validate the models, as described in Section 3.5.1.

- **"Second case"** model; in this case, two loads were defined, 90 kN each, and applied statically in vertical direction to the outer surface of cylindrical surface located at the axle ends where seats of the axle-box existing. Same boundary condition of displacements and rotations introduced in the first case were used. The loads and boundary conditions for this case are presented in Figure 3.5 and its results introduced in Section 3.5.3. This case represents the wheelset rolling on a perfectly smooth track, neglecting any effect related to the deformation of the track or the wheel.

- **"Third case"** model; real case, where the simply supports BCs used in the previous two cases were replaced by the train primary suspension. For this purpose, three springs are considered at each end in x, y, and z direction, and the loads were applied statically to the vertical springs. Also, the stiffness of the wheel and infrastructure are estimated in Section 3.2.7 and considered in this model, as shown in Figure 3.6. Moreover, two different sources of irregularities are applied directly to the wheel springs. These irregularities include wheel out of roundness (OOR) and wheel-rail contact excitation due to wheel OOR disturbance (see Section 3.2.8 for an example of these irregularities).

Figure 3.5: *"Second case" model with simple support BCs and loads applied at the axle ends.*

Special attention is paid to the wheel OOR disturbance because the component of the signal caused by this disturbance is periodic with the wheel turn, hence providing the same NxRev components caused by crack breathing, so that this disturbance cannot be separated by the use of synchronous averaging. The results of this case are presented in Section 3.5.5.

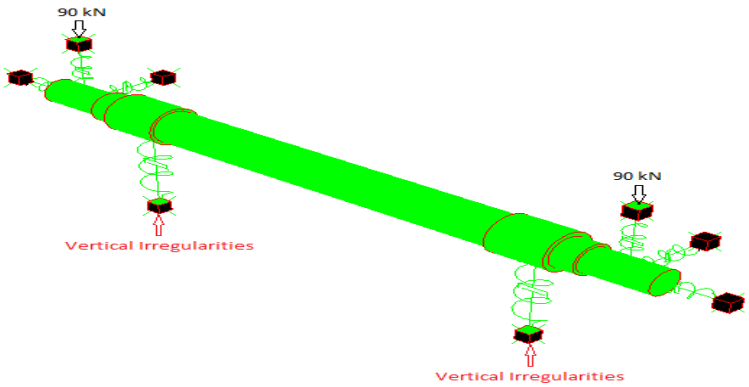

Figure 3.6: *"Third case" model (real case of the axle with primary suspension and representation of wheel stiffness).*

3.2.7 Estimation of railway wheel and infrastructure stiffness

To consider the stiffness of the railway wheel and the infrastructure under it, one wheel and portion of track were modeled using 3D finite elements included in ABAQUS commercial software. In this model, forces were applied statically at the internal surface of the wheel hub. The wheel was mounted above a system including, rail, sleepers, pad and bed, as shown in Figure 3.7. Typical values of sleeper bay, sleeper mass, track bed stiffness, track bed damping, rail pad stiffness and rail pad damping were adapted directly from [53] and are presented in Table 3.1.

The stiffness coefficient was calculated as: $k_w = \frac{F}{\delta}$, where k_w is the wheel and infrastructure stiffness coefficient, F is the acting force and δ is the total vertical deformation of the wheel hub. Two different cases were simulated, firstly, considering the wheel located above one sleeper and the second case considering the wheel located in the middle of a sleeper bay. The results showed that there is no big difference in the stiffness between the two cases where its value in the first case is equal to $1.45 \times 10^8\ N/m$ whilst in the second case is equal to $1.3 \times 10^8\ N/m$.

Table 3.1: *Typical values of track model components*

Track model component	Value
Sleeper bay	$0.5\,m$
Sleeper mass	$324\,kg$
Track bed stiffness	$200\,MN/m$
Track bed damping	$150\,kN.s/m$
Rail pad stiffness	$1\,GN/m$
Rail pad damping	$50\,kN.s/m$

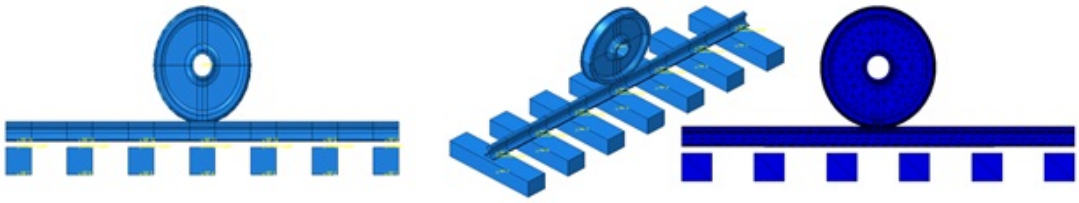

Figure 3.7: *Estimation of railway wheel stiffness.*

Typical values of stiffness and damping coefficients of railway vehicle primary suspension are summarized in Table 3.2 [53], also the calculated value of railway wheel stiffness coefficient is mentioned in this table. Railway wheel damping coefficient was assumed approximately equal to its stiffness divided by 10^3.

Table 3.2: *Typical values of stiffness and damping coefficients for axle primary suspension and calculated values for axle wheel*

Direction	**K** (N/m)	**C** $(N.s/m)$
Longitudinal (x)	7.5×10^6	1×10^5
Lateral (y)	7.1×10^6	1×10^5
Vertical (z)	8.1×10^5	3×10^4
Wheel	1.375×10^8	1×10^5

3.2.8 Wheel out-of-roundness (OOR) model

As mentioned before, two sources of irregularities were included in third case model, wheel OOR and wheel-rail contact excitation due to wheel OOR. A profile of wheel OOR was introduced as a sum of twenty sine functions with wavelengths corresponding to the nominal wheel circumference (2.88 m) and the nineteen lowest sub-multiples. The amplitudes of these components were defined based on the elaboration of experimental measurements of wheel OOR reported in [54] while the phases of the harmonics were generated using different random sets of numbers for each wheel, therefore, avoiding correlation of the OOR profiles obtained on the different wheels. An example of wheel OOR signal and its spectrum at 592 RPM for left and right wheel is shown in Figure 3.8.

Wheel OOR profile led to simultaneous wheel-rail contact excitation depending on the train speed at several frequencies. Excitation frequency can be calculated as: $f = \frac{S}{\lambda}$, where S is the train speed and λ is a wavelength. For the first five wavelengths of wheel

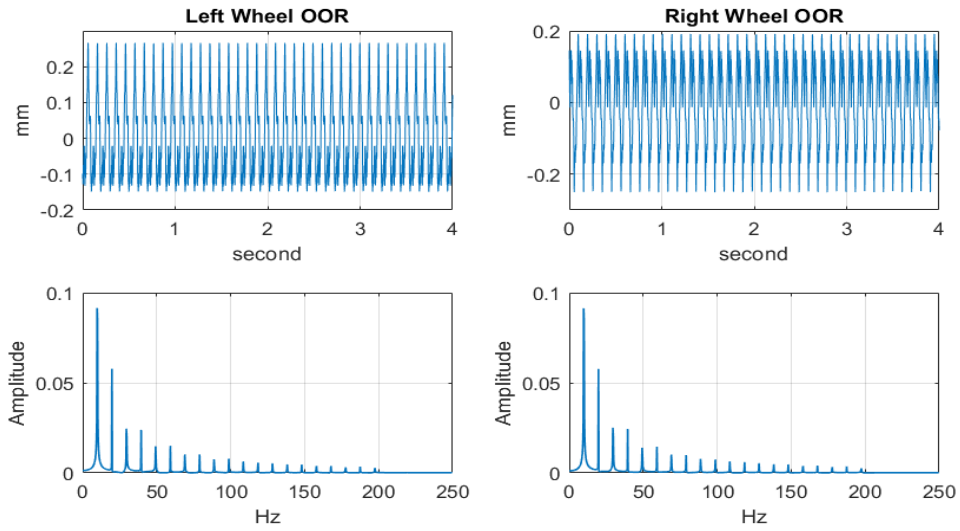

Figure 3.8: *Wheel OOR signal and its spectrum at 592 RPM for left and right wheel.*

OOR profile, the excitation frequencies are in range $5 \sim 125$ [Hz] for train speed in the range of $50 \sim 250$ [Km/h], as introduced in [41, 55].

A combination of wheel OOR and wheel-rail interaction disturbances based on the above mentioned calculation is presented in Figure 3.9 for right and left wheel.

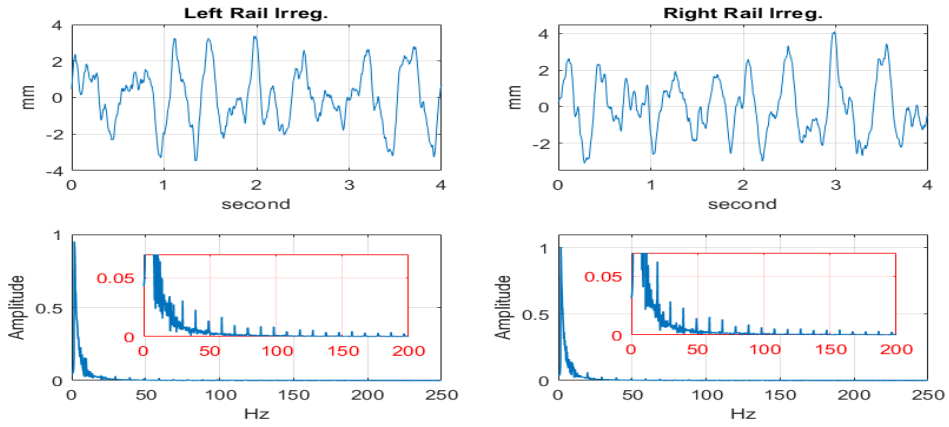

Figure 3.9: *A combination of wheel OOR and wheel-rail interaction signals at speed 592 RPM for left and right wheel.*

3.2.9 Crack locations and measuring section positions

In the "first case" model, the case which represents the experimental tests, the crack was introduced close to the central region and the vibration signals were measured from same positions and directions as of the sensors used in the experimental tests, as introduced in section 3.4. In the "second" and "third case" model, different crack locations were model for both hollow and solid axle. These locations were selected to cover the possibility of crack existence at any section of the axle. Crack locations were

considered at the wheel seats and at three positions in the central portion of the axle as shown in Figure 3.10. Different possible measuring points were considered: at the axle-boxes, in the middle of the axle and at two other intermediate sections of the axle (see Figure 3.10). Special attention was paid to measuring points (1) and (5) because these two points are located at the axle-boxes positions which means easy to install vibration measuring devices (e.g. accelerometers).

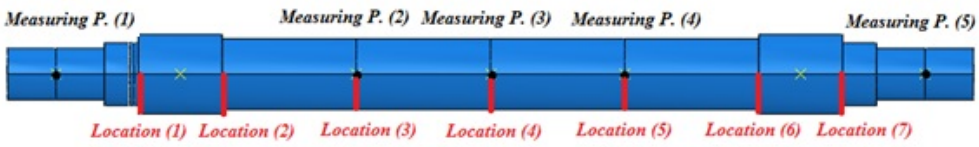

Figure 3.10: *Different cracks and measuring sections locations.*

Since the type of simulation is explicit, loading and rotation were applied in a way to avoid sudden amplitude changes causing convergence problems. This was done by introducing tabular values of gradually rising amplitudes of force and rotation speed.

Crack size (%) in this work means the percentage of the cracked area to the total cross-section area. Different crack sizes (0% (no crack case) until 50% with 5% step, as shown in Figure 3.11) were modeled and simulated at every crack location presented in Figure 3.10.

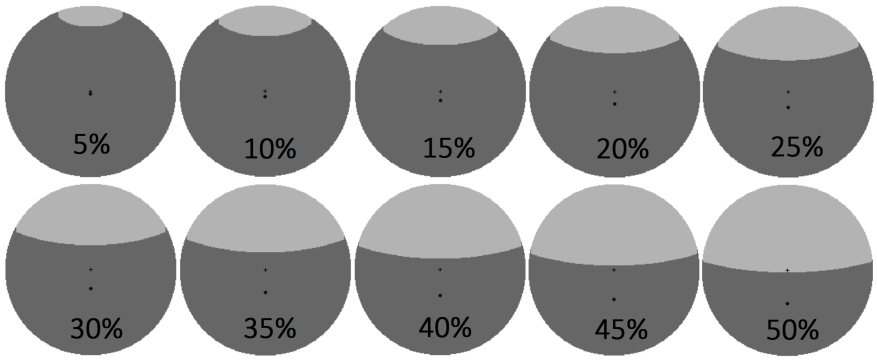

Figure 3.11: *Shapes of elliptical crack with different sizes for solid axle (light color: cracked area, dark color: Intact area).*

3.3 FE model using Timoshenko's beam elements

The breathing mechanism can be modelled using different approaches. Accurate models can be based on the Finite Element method using solid elements and modeling the crack by means of non-linear contact elements with or without friction, as introduced in Section 3.2. However, a mathematical model of this type is highly computationally intensive, due to the very large number of nodal coordinates involved in the analysis. Furthermore, the boundary conditions that can be applied to the Finite Element model with solid elements are necessarily simplified and cannot reproduce the complex situation arising for a railway axle being part of a wheelset rolling on a flexible, irregular track in presence of wheel OOR.

An alternative approach is to model the axle using Timoshenko's beam elements and to use a simplified model of crack breathing mechanism which is based on introducing one beam element having first and second area moments of the cross section which are periodically varying depending on the angular position of the axle and on the shape and depth of the crack [10]. This second modeling approach is developed hereafter. Timoshenko's beam elements with 6 DOFs per node were used to construct the Beam FE model shown in Figure 3.12.

In this model, the modeling and simulation of railway axle with a crack that produces variation in the stiffness as a function of the stress field over the shaft cross section that depends on the crack angular position was introduced. This approach consists of different steps by considering the equivalent beam element shown in Figure 3.12, in which the cross section is formed by the non-cracked part of the section plus the closed part of the cracked section. The length of the equivalent beam element (l_c) is defined in Section 3.3.3 as function of the depth of the crack, according to the method presented in [10].

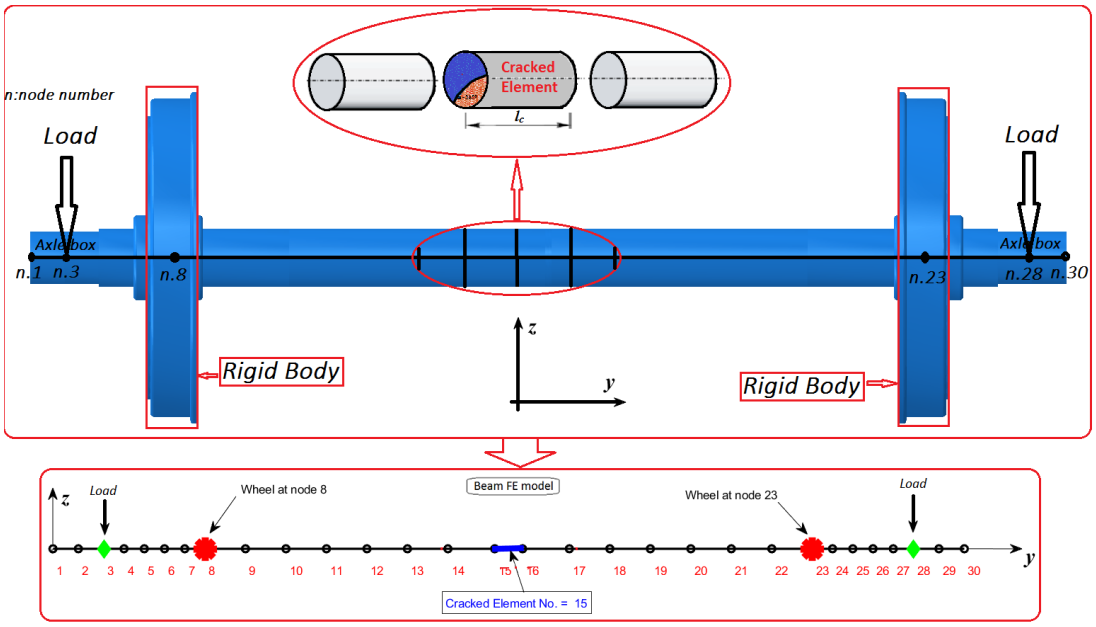

Figure 3.12: *An example of wheelset discretization using beam element included one cracked element (l_c).*

3.3.1 Equation of motion of cracked axle

The wheelset was discretized as shown in Figure 3.12. Timoshenko's beam theory [56] was used to obtain the stiffness matrix of the axle and the cross-section area was updated using the crack breathing mechanism model introduced in Section 3.3.2.
The obtained model is represented mathematically by a set of differential equations as given by Equation 3.6:

$$[M_{FE}]\langle\ddot{x}(t)\rangle + [C_{FE}]\langle\dot{x}(t)\rangle + [K_{FE}(t)]\langle x(t)\rangle = \langle F_{FE}\rangle \tag{3.6}$$

where:
$x(t) = [y_1 \;\; z_1 \;\; x_1 \;\; \theta_{y_1} \;\; \theta_{z_1} \;\; \theta_{x_1} \;\; ... \;\; y_n \;\; z_n \;\; x_n \;\; \theta_{y_n} \;\; \theta_{z_n} \;\; \theta_{x_n}]^T$ is the vector of nodal coordinates and n is the total number of nodes. Figure 3.13 shows the reference frame of one finite element and its DOFs. M_{FE}, C_{FE} and $K_{FE}(t)$ are the Finite Element mass, damping and stiffness matrices of the cracked axle respectively. F_{FE} is the forces vector acting at the elements nodes. The stiffness matrix $K_{FE}(t)$ is time-dependent due to the periodic variation of the stiffness properties of the cracked element.

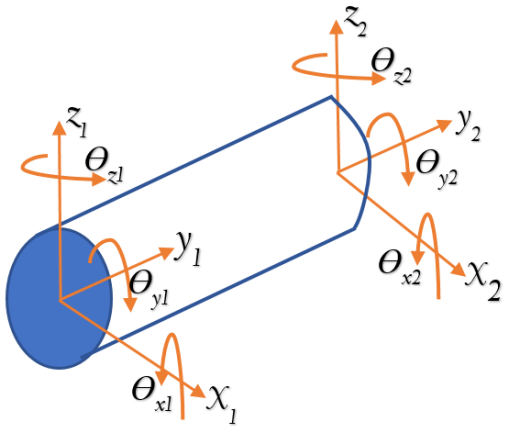

Figure 3.13: *Reference frame of beam element DOFs.*

The stiffness and mass matrices of Timoshenko beam element with 6 DOFs per node shown in Figure 3.13 are presented as follow:

Stiffness Matrix

$$k_e = \begin{pmatrix} t & 0 & 0 & 0 & 0 & 0 & -t & 0 & 0 & 0 & 0 & 0 \\ & a & p & 0 & -q & c & 0 & -a & -p & 0 & -q & c \\ & & b & 0 & -d & q & 0 & -p & -b & 0 & -d & q \\ & & & j & 0 & 0 & 0 & 0 & 0 & -j & 0 & 0 \\ & & & & h & -r & 0 & q & d & 0 & g & -s \\ & & & & & e & 0 & -c & -q & 0 & -s & f \\ & & & & & & t & 0 & 0 & 0 & 0 & 0 \\ & & & sym. & & & & a & p & 0 & q & -c \\ & & & & & & & & b & 0 & d & -q \\ & & & & & & & & & j & 0 & 0 \\ & & & & & & & & & & h & -r \\ & & & & & & & & & & & e \end{pmatrix},$$

where, the coefficients are defined as:

$$t = \frac{EA}{l}, \quad a = \frac{12J_xE}{(1+\phi)l^3}, \quad b = \frac{12J_zE}{(1+\phi)l^3}, \quad c = \frac{6J_xE}{(1+\phi)l^2}, \quad d = \frac{6J_zE}{(1+\phi)l^2}, \quad e = \frac{(4+\phi)J_xE}{(1+\phi)l},$$

$$f = \frac{(2-\phi)J_xE}{(1+\phi)l}, \quad g = \frac{(2-\phi)J_zE}{(1+\phi)l}, \quad h = \frac{(4+\phi)J_zE}{(1+\phi)l}, \quad p = \frac{12J_{xz}E}{(1+\phi)l^3}, \quad q = \frac{6J_{xz}E}{(1+\phi)l^2}, \quad r = \frac{(4+\phi)J_{xz}E}{(1+\phi)l}$$

$$s = \frac{(2-\phi)J_{xz}E}{(1+\phi)l}, \quad j = \frac{GJ_p}{l}, \quad \phi = \frac{12EJ}{GAl^2}$$

The parameter ϕ counts for the shear effects, E and G are respectively the Young's modulus and the shear modulus, A is the cross-section area, different J are the second moments of area. J_p is the polar second moment of area around y axis. l is the element length. The length of the cracked element is set to l_c which depends on the crack size as introduced in Section 3.3.3. The coefficients p, q, r, s equal to zero for the all non-cracked elements because J_{xz} has a value for cracked element only due to asymmetry cross-section. In case of cracked element, the cross-section area (A) and the second moments of area (J, J_{xz}) are updated depending on the angular position of the axle and calculated at every simulation time step using simple model of crack breathing mechanism introduced in Section 3.3.2.

Mass Matrix

$$m_e = \frac{\rho A a}{105}\begin{pmatrix} 70 & 0 & 0 & 0 & 0 & 0 & 35 & 0 & 0 & 0 & 0 & 0 \\ & 78 & 0 & 0 & 0 & 22a & 0 & 27 & 0 & 0 & 0 & -13a \\ & & 78 & 0 & -22a & 0 & 0 & 0 & 27 & 0 & 13a & 0 \\ & & & 70r & 0 & 0 & 0 & 0 & 0 & -35r & 0 & 0 \\ & & & & 8a^2 & 0 & 0 & 0 & -13a & 0 & -6a^2 & 0 \\ & & & & & 8a^2 & 0 & 13a & 0 & 0 & 0 & -6a^2 \\ & & & & & & 70 & 0 & 0 & 0 & 0 & 0 \\ & & & sym. & & & & 78 & 0 & 0 & 0 & -22a \\ & & & & & & & & 78 & 0 & 22a & 0 \\ & & & & & & & & & 70r & 0 & 0 \\ & & & & & & & & & & 8a^2 & 0 \\ & & & & & & & & & & & 8a^2 \end{pmatrix},$$

where, in this matrix:
$2a$ is the element length, ρ is the axle material density and $r = \frac{J_p}{A}$.

The damping matrix (C_{FE}) is constructed using Rayleigh damping approach, presented in Section 3.2.5, where; α= 3 and β= 0.0001 are defined to produce 3% damping ratio covering range of frequencies from 10 Hz to 150 Hz which is the frequency range of interest in this work.

Equation 3.6 is solved in time domain using the Newmark method with fixed time step using a code written in MATLAB language.

3.3.2 Simple model of crack breathing mechanism

The breathing mechanism is a result of the stress and strain distribution around the cracked area, which is due to static loads (such as the axle weight, the bearing reaction forces), and the dynamic loads (such as the unbalance and the vibration induced by the inertia force distribution). When the static loads overcome the dynamic ones, the breathing is governed by the angular position of the axle with respect to the stationary load direction, so that the crack opens and closes completely once per revolution [10, 41, 57], as shown in Figure 3.14.

The corresponding calculation can be carried out step by step through an iterative procedure as introduced in Figure 3.16. The opening and the closing (breathing mechanism) of the crack is determined by the stress field over its cross section as caused by the dynamic bending moments. Here, the system is nonlinear and the crack parameters have to be determined for each time step. The model of the breathing mechanism used was adapted from [10]. The identification process starts with the estimation of the crack parameters and the modeling of the structure through the finite element method. It is considered that the crack influences only the stiffness parameters. Consequently, it is assumed that the other parameters do not change in the presence of a crack.

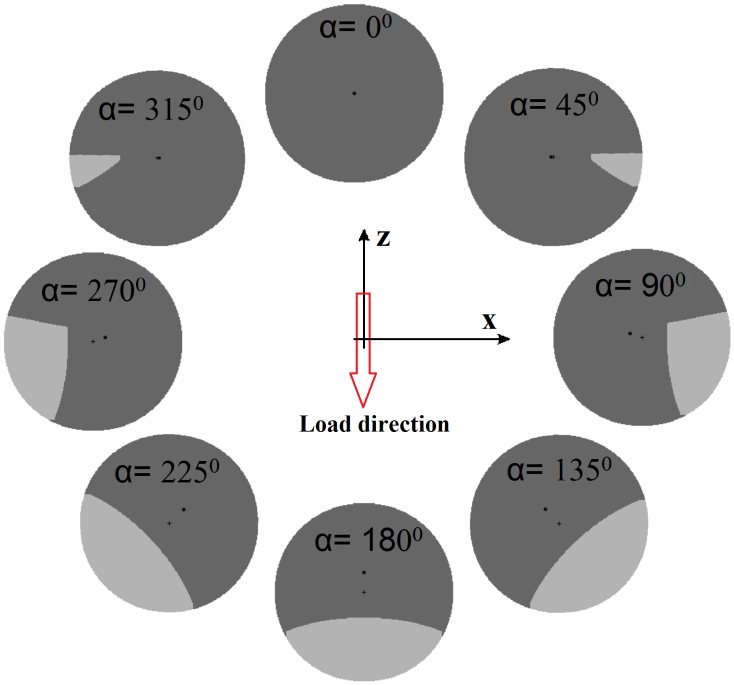

Figure 3.14: *Breathing mechanism of 30% elliptical crack during one revolution (light color: cracked area, dark color: Intact area).*

To determine the stiffness matrix of the cracked element, $K_c(t)$, it is necessary to calculate the second moments of inertia of the cross section where the crack is located. For a given shape and depth of the crack, these sectional properties are determined as function of the axle's angular position using an iterative procedure which aims at reproducing the crack breathing mechanism [10]. To this aim, the cross section is meshed as shown in Figure 3.15. Starting from an initial assumption on the opening/closing of the crack, the geometric centre, first and second area moments of the section are computed.

By using these parameters, the tensile stresses resulting from the static bending moment applied on the cracked section are computed at each cell. Then, the cells of the mesh at which the crack is open/closed are obtained as a function of the tensile stresses found: if at one cell the tensile stress is positive, it means crack is open at the considered location and therefore the cell does not contribute to the calculation of the moments of inertia of the cross section. If otherwise the tensile stress is negative, it means the two facing surfaces of the crack are pressed together, so the crack is closed at the considered location and the cell contributes to the moments of inertia of the cross section and then

to the stiffness matrix. The procedure is repeated iteratively, until convergence of the cross-sectional moments of inertia is reached.

Finally, the procedure is repeated for a different angle of rotation of the axle (in steps of 1 Deg for example) and the values of the sectional parameters A, J_x , J_z and J_{xz} are calculated for the new angle of rotation. More details about this breathing mechanism model and its calculation steps can be found in [10].

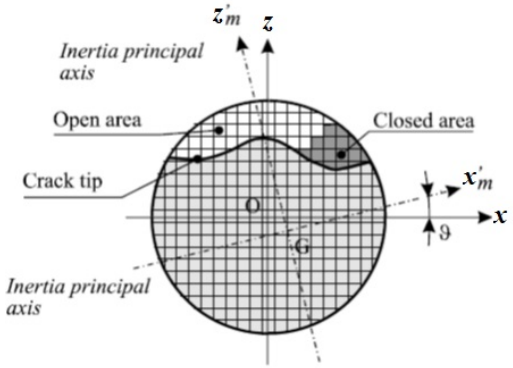

Figure 3.15: *Cross section mesh of the cracked element [10].*

Figure 3.16 shows a flowchart of the iterative calculations of the breathing mechanism as well as the axle response at every rotational angle of the axle.

An example of the change of resisting cross-section area (A) for solid axle with diameter 0.16 m and 50% crack during one revolution as well as the resulting moments (J_x, J_z and J_{xz}) calculated depending on resisting cross-section area and the angular position of the axle (α) are presented in Figure 3.17.

3.3.3 Cracked element length (l_c)

The length of the cracked element (l_c) must be calculated to represents the influence of the discontinuity introduced by the crack, which obviously depends on the crack depth. This cannot be determined easily, because axial stresses due to bending, start from strongly non-linear distribution in correspondence of the crack and along the beam gradually assume a quasi-linear distribution over the cross section as the distance from crack increases. The equivalent beam length (l_c) has been defined empirically in [10] based on the best fitting between a 3D model and the simplified one. This length depends only on the depth of the crack and is considered constant and independent from the breathing mechanism effect. The dimensionless values of $\frac{l_c}{D}$ (D referred to the diameter of the shaft) are shown in Figure 3.18 as function of the crack size, for transverse cracks with rectilinear tip. Negligible differences have been found in case of elliptical crack tip according to [10].

The same crack locations and measuring sections introduced in Section 3.2.9 for the solid FE model have been introduced to the beam FE model shown in Figure 3.12. The crack breathing mechanism was applied to specified elements corresponding to same locations introduced in Figure 3.10 for the solid FE model and measuring the axle vibration from nodes corresponding to same measuring sections presented in Figure 3.10 for the solid FE model.

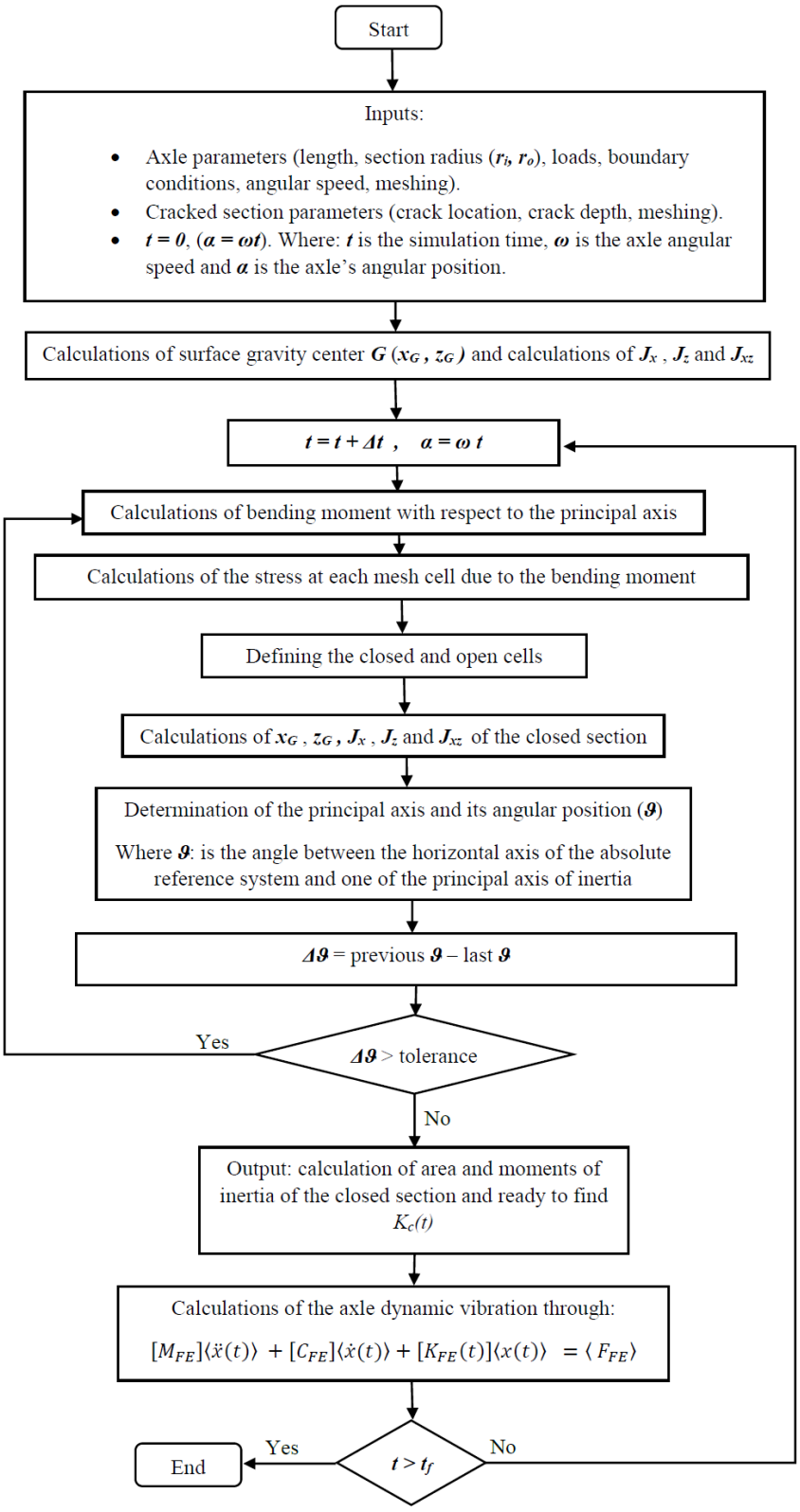

Figure 3.16: *Flowchart of the iterative calculation of the breathing mechanism [10] and the axle response.*

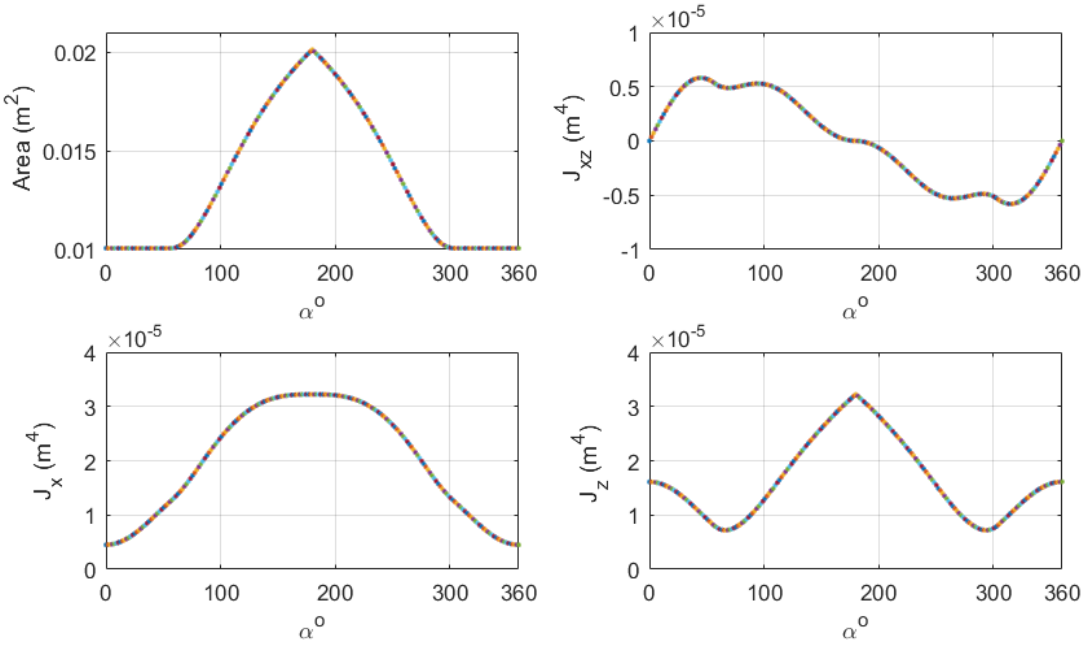

Figure 3.17: *Example of calculated* $A, J_{xz}, J_x and J_z$.

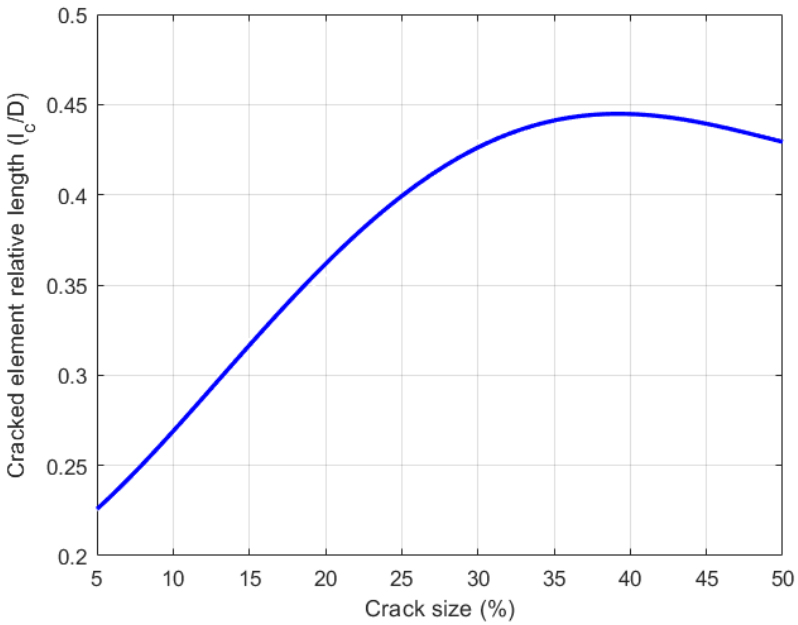

Figure 3.18: *Relationship between the crack size (%) and cracked element relative length (*$\frac{l_c}{D}$*); adapted from [10].*

Table 3.3 Summarizes the crack locations and measuring sections for the solid FE and Timoshenko beam FE models. It's worth to clarify that, for same cracked axle parameters, the solid FE model calculations requires some hours of simulation time whilst the beam FE model requires just few minutes.

Table 3.3: *Crack locations and measuring sections for the solid FE model (Figure 3.10) and the beam FE model (Figure 3.12)*

	Symbol	Solid FE model	Beam FE model
Crack Locations	$C1$	Location 1	Element 7
	$C2$	Location 2	Element 8
	$C3$	Location 3	Element 11
	$C4$	Location 4	Element 15
	$C5$	Location 5	Element 19
	$C6$	Location 6	Element 22
	$C7$	Location 7	Element 23
Measuring Sections	MP_1	Measuring P. 1	Node 3
	MP_2	Measuring P. 2	Node 11
	MP_3	Measuring P. 3	Node 15
	MP_4	Measuring P. 4	Node 20
	MP_5	Measuring P. 5	Node 28

3.4 Laboratory tests

Two experimental tests were carried out on full-scale railway solid axles specimens. Results from previous tests are used to validate the beam FE models of cracked solid and hollow axles. Description of the laboratory bench and tests set-up are presented in next subsections and the tests and FE models results are presented in next sections.

3.4.1 POLIMI fatigue test bench

The POLIMI fatigue test bench, shown in Figure 3.19, is a dynamic test bench for railway axles available at the labs of Politecnico di Milano, Department of Mechanical Engineering. This bench consists of one central bearing unit connected to an actuator that applies a vertical load on the specimen and two supports carrying the axle through tapered bearing units. The specimen is rotated using an electric motor to generate rotating bending fatigue. Three-point rotating bending load on a full-scale railway axle specimen tests are performed using this bench.

The bending vibration of a specimen axle reproducing the wheel press-fit region of a real railway axle was measured using the internal LVDT transducer of the hydraulic actuator and saved automatically to the test bench computer. It should be noted that the central part of the specimen is intended to reproduce one of the two-wheel seats in the real axle. Therefore, measuring the vibration in the central portion of the specimen corresponds to measuring the vibration of the real axle near the wheel mount, which is in turn close to the axle-box.

The tests in question are mainly intended to quantify the rate of crack propagation in railway axles as a function of different parameters such as axle design and material, surface treatments and applied axle loading [58]. Many tests were conducted in a framework of a project investigating crack growth rates and NDT inspection intervals and different specimens with different crack location were tested. Unfortunately, during the period of this work, all tests have been carried out on specimens with cracks under the press-fit part (under the inner ring of the central bearing) so, the below men-

tioned set-up of low frequency vibration (LFV) has been used to test the possibility of using the proposed SHM technique to detect the crack under press-fit parts (e.g. wheel seats) of railway axle as introduced in Section 3.5.2, whilst, for cracked axle FE models validation, two tests measurements obtained from the LVDT transducer for solid and hollow specimens have been used.

3.4.2 Laboratory tests set-up

Due to the limited pass-band of the LVDT transducer, an additional measuring set-up was installed in the bench to measure vibrations of the axle specimen, consisting of two laser distance meters Mel Electronic M7L/20 and one accelerometer. One laser transducer and the accelerometer are mounted in vertical direction directly above the central portion of the specimen.

The specimen is constrained at three points in horizontal direction (two at the ends and one at the central part), therefore, the horizontal transducer was installed between the specimen right end and the central part of it (see Figures 3.19 and 3.20). The vertical transducer and the accelerometer were installed to point the vertical vibration of the specimen central region, which is the one undergoing the largest bending displacements so that the highest sensitivity for vibration changes was achieved. The tests were carried out under constant speed.

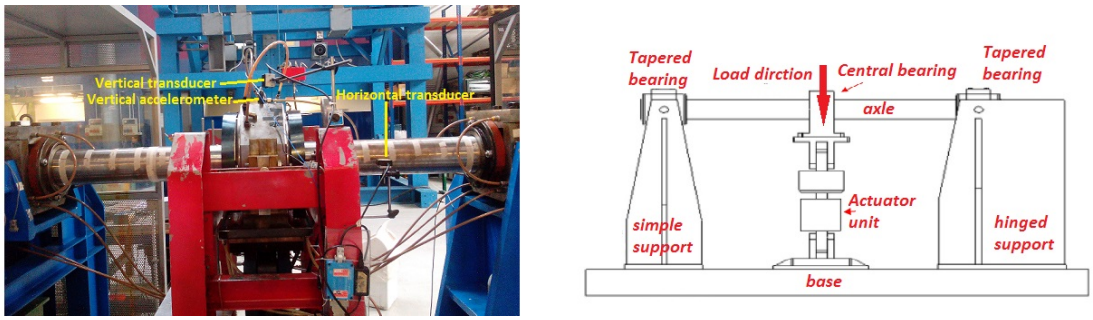

Figure 3.19: *Dynamic test bench for full scale railway axle (left: view of POLIMI bench , right: bench scheme).*

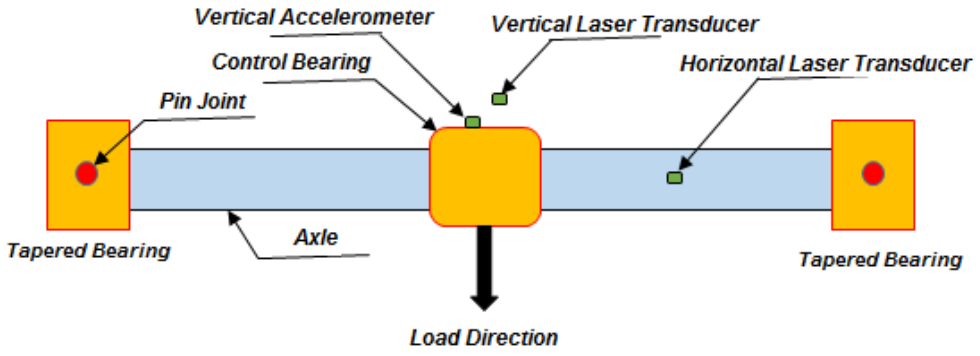

Figure 3.20: *Positions of the transducers and the accelerometer.*

3.4.3 Data acquisition

Data Acquisition was performed using NI modules, NI-9234, NI-9239, gathered in DAQ-9172 chassis. Due to the high flexibility and capability of MATLAB software, it was used to develop automatic acquisition routine allowing to collect vibration signal at pre-defined time intervals (e.g. every 15 minutes) and save it for further analysis. In next step, the collected signals were treated using a signal processing technique coded in the same environment (MATLAB software). Firstly, the signal was filtered (using bandpass filter) and afterwards, by means of fast Fourier transform ("FFT", MATLAB toolbox function), the signal spectrum could be obtained for every collected data block (time record).

Data were acquired for time durations multiples of the theoretical period of revolution. Due to slight change of rotational speed during data acquisition, as shown in Figure 3.21, not exactly integer number of revolution could be obtained and phenomena called "leakage" could appear in the signal spectrum. Leakage creates peaks at wrong frequencies, non-existing peaks, or change in amplitudes of existing peaks and therefore, reduces the ability to correctly observe peaks in the signal spectrum, due to creation of 'false' peaks and reducing spectral resolution [41]. To avoid the leakage influence, Hanning window was applied to compensate the small deviation of the angular speed from the nominal one. Additional routine was coded in MATLAB environment to grab the peaks of the signal harmonics automatically from its spectrum and therefore, the harmonics changes could be tracked during the test.

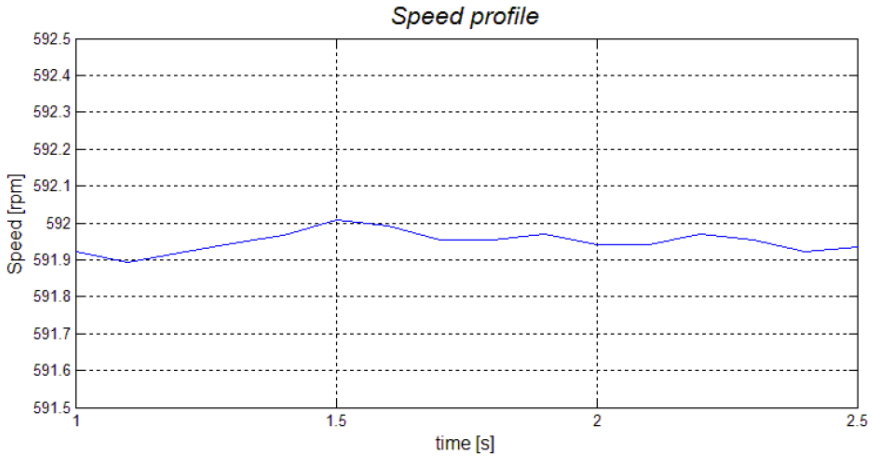

Figure 3.21: *Example of axle speed variation during test.*

Laser distance transducer

Axle displacement vibrations were measured using laser distance meters Mel Electronic M7L/20 (see Figure 3.22). Displacements at maximum 0.009 [mm] resolution can be measured using this type of transducer, defining the smallest change in distance sensor can be detected.

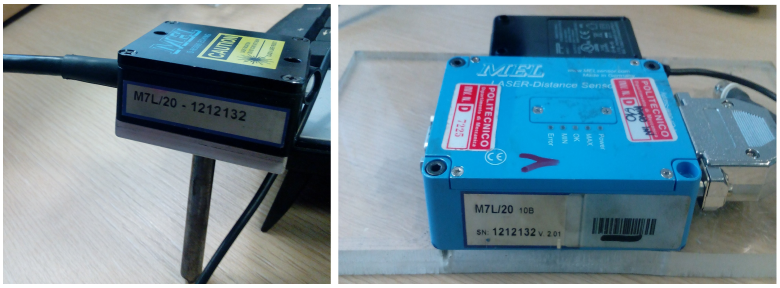

Figure 3.22: *Laser transducer head (left) and its power supply unit (right).*

Accelerometer

One accelerometer was used to measure the vertical vibration of the central part of the axle where the crack propagated from predefined artificial notches.
4508 DeltaTron Accelerometer was used during the experiments, with measurement frequency range 0.3 [Hz] till 8 [kHz], and measuring amplitude range -/+700 ms^{-2} peak (-/+ 71 g peak) (see Figure 3.23).

Figure 3.23: *4508 DeltaTron accelerometer.*

Laser transducers and accelerometer acquisition module

The signals measured by the laser transducers were collected by means of acquisition module NI 9234 (see Figure 3.24). The four input channels of this module are capable of simultaneously digitize signals at rates up to 51.2 [kHz] per channel with built-in anti-aliasing filters that automatically adjust to specified sampling rate. This module offers 24-bit resolution and 102 [dB] dynamic range. The NI 9239 data acquisition module was used for accelerometer's signal acquisition (see Figure 3.24).

Data acquisition chassis

The NI cDAQ-9178 chassis was used to collect and transfer measured signals from the modules to PC (see Figure 3.24). It is an eight-slot USB chassis designed for use with C series I/O modules, can measure a broad range of analog and digital I/O signals and sensors using a Hi-Speed USB 2.0 interface. Sampling rate value (5 kHz) chosen for measuring axle vibrations was applied to all modules channels.

Figure 3.24: *Sensors modules and data Acquisition chassis*
left: laser transducers module middle: accelerometer module right: modules rack.

3.5 Experimental and simulation results

As mentioned before, two types of cracked axles (solid and hollow) were modeled using two different types of Finite Element. Three cases of boundary and loads conditions were considered, see Section 3.2.6, and their results are introduced here:

3.5.1 Comparison of Beam FE model and laboratory experiments

The schematic of this case is shown in Figure 3.4. As mentioned before, to enable comparison with tests, two Timoshenko beam FE models of cracked axles were defined reproducing the geometry of a solid specimen axle and a hollow one used in the tests. The length of both specimens is 2.18 m, the external diameter is 0.147 m for the solid axle and 0.16 m for the hollow one and the bore diameter of the hollow axle is 0.065 m. In the tests, the specimens were rotated at the constant speed of 592 RPM (9.86 Hz). The two-tapered bearings supporting the specimen in the test stand are reproduced in the FE model using simple support BCs at the specimen ends. Vertical forces with magnitudes 185 and 170 kN is applied to the central section of the models of solid and hollow axles, respectively, to reproduce the loads applied in the test stand by the hydraulic actuator. To investigate the effect of crack propagation on the specimen vibration, different crack sizes from 0% (intact axle) to 50% in 2% steps were modeled for the solid and hollow specimens.

Because measurements of crack size could not be carried out during the test, a relationship between the amplitude of the NxRev harmonics and the size of the crack could not be established directly from test results. The crack size was measured at the end of tests by means of magnetic particles test and the crack propagation software AFGrow v. 4.0012.15 [59]. The estimated final cracks sizes at the end of the tests are 30% and 38% from total cross-section area for the solid and hollow specimens respectively.

The trends of 1xRev, 2xRev and 3xRev harmonic components are plotted as a function of crack size for beam FE models results and as a function of number of loading cycles for experimental results and introduced in Figure 3.25 for the solid axle and in Figure 3.26 for the hollow axle.

Validation using crack propagation laws

In order to relate the size of the crack during the test with the number of loading cycles applied, a backward calculation based on crack propagation laws [58] was used. By introducing the final crack size, the final number of cycles, the maximum and minimum stresses at the cracked cross-section and the material properties, an estimate was

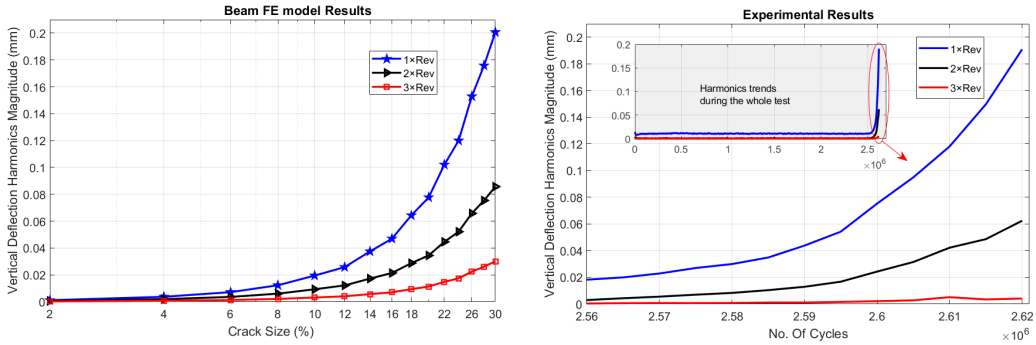

Figure 3.25: *Experimental validation of the solid axle beam FE model.*

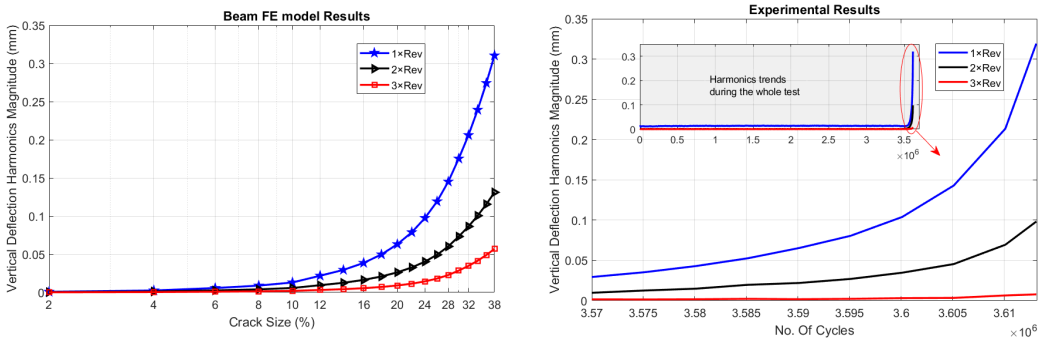

Figure 3.26: *Experimental validation of the hollow axle beam FE model.*

obtained for crack size as function of the number of loading cycles applied. Since the vibration of the specimen was continuously measured during the tests, the trend of NxRev vibrations with the number of loading cycles was obtained. Finally, merging the two trends of crack size and NxRev vibration with loading cycles, the relationship between NxRev vibration and crack size was obtained from the experiments.

Figure 3.27 compares the trend with crack size of the magnitude of the 1xRev and 2xRev harmonics for the measured and simulated vertical displacement in the centre of the specimen. The comparison of the 3xRev components is not shown because the experimental measure of this high frequency portion of the signal could not be measured accurately in the experiment due to the limited pass-band of the LVDT transducer.

In Figures 3.25, 3.26 and 3.27, a satisfactory agreement between the experimental and FE models results can be observed, especially for the 1xRev components, whereas for the 2xRev components a less good agreement is observed, again on account of the limited passband of the LVDT transducer used in the experiment.

3.5.2 Experimental results of axle with crack under press-fit part

The test set-up introduced in Section 3.4 has been used to test the possibility of using LFV measurements to detect the crack under press-fit part of railway axle. Two experiments were carried out for two solid axles specimens. In both tests, the cracks were introduced under the central bearing fitting part at distance 10 mm from its end as shown in Figure 3.28.

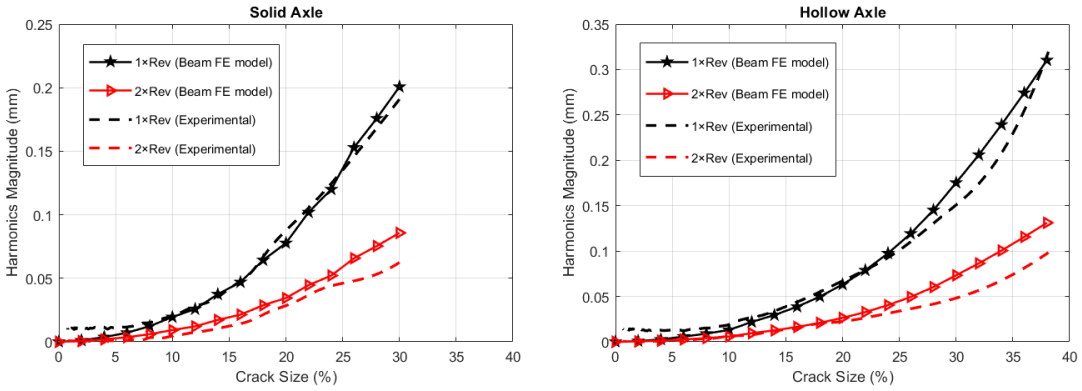

Figure 3.27: *Experimental validation of the beam FE model (left: solid axle; right: hollow axle).*

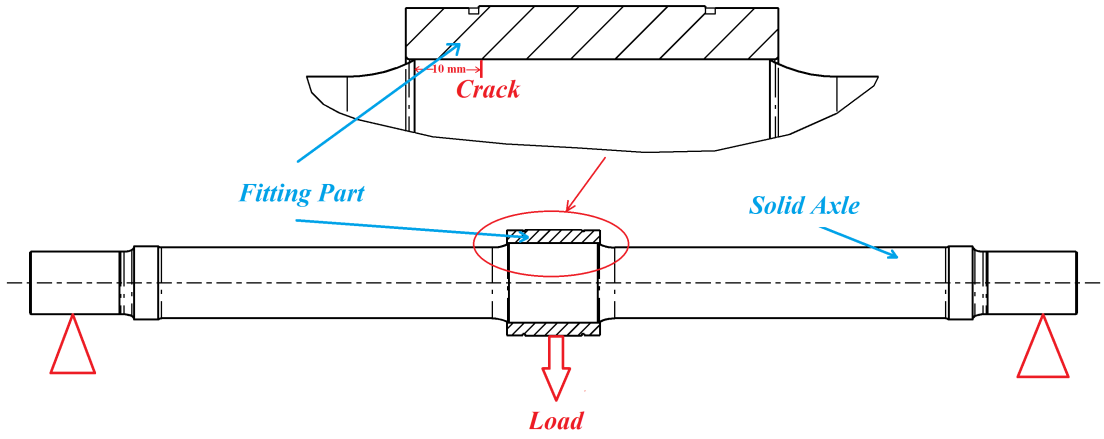

Figure 3.28: *Solid axle with crack under press-fit part of the central bearing.*

In both tests, the axles were running at constant speed (509 RPM) with different loads in each test. 100 kN was applied in the first test which ended at 33.5 million revolutions, while the second test run 15 million cycles with load 100 kN and afterward, it was increased to 125 kN and the test ended at 21.4 million loading cycles. After disassembling from the test rig, the axles were cut vertically at cracked section to analyse the crack propagation and its size. The inspections of the crack sections revealed that, in the first test, the crack did not propagate while in the second test, the crack propagated from the artificial notches to a size, approximately, equal to 16%, as illustrated in Figure 3.29. The results of the first three harmonics components for vertical acceleration are plotted with number of loading cycles for each test and introduced in Figure 3.30.

The results show that there is no change could be monitored from the harmonics trends of the first test whilst in the second test, the trends of the harmonics started to increase after loading cycles equal to 19.5 million, approximately, and continue increasing until the test stopped due to safety reason, unfortunately. These first results suggest that the proposed technique of railway axle health monitoring can be used to detect the crack even when it propagates under the press-fit parts. Moreover, more tests and a sound theoretical analysis are needed to confirm this statement. This is envisaged as a further work after this thesis.

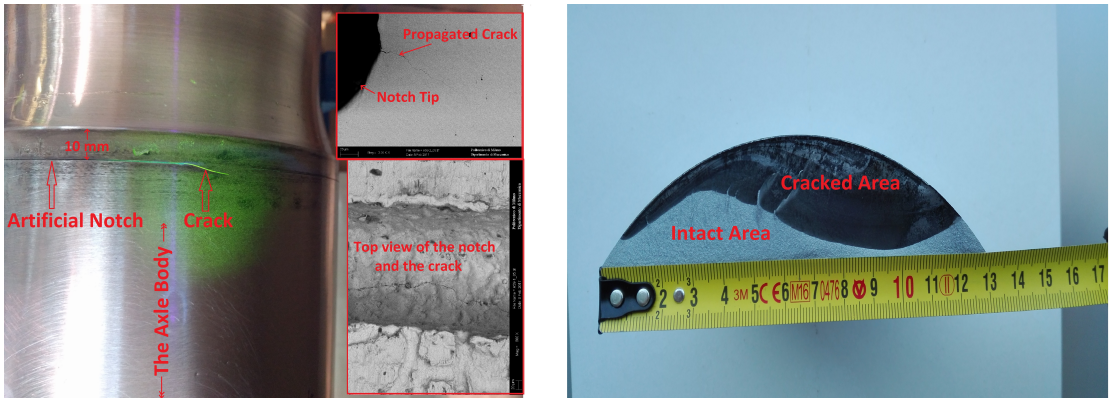

Figure 3.29: *Cracked section of second test specimen (left: propagated crack from the artificial notch; right: portion of the cracked cross-section).*

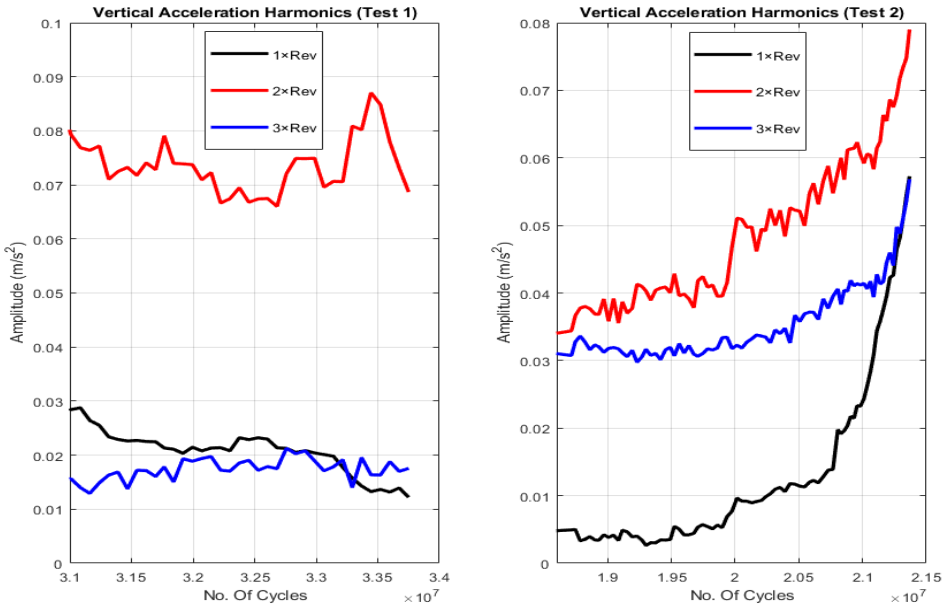

Figure 3.30: *Trends of first three harmonics of vertical acceleration (left: results of test 1, right: results of test 2.*

3.5.3 Comparison of solid FE model and beam FE model

The loads and boundary conditions of this case are presented in Figure 3.5. In both model of solid and hollow axle, Different possible locations of the crack and different locations of the measuring points for the monitoring equipment were considered [60], as presented in Figure 3.10. To investigate the influence of crack size change on axle dynamics, simulations were conducted in a way to cover cases from 0% (non-cracked axle) up to 50% of cracked cross section, evenly distributed in steps of 5% crack size, at every crack location. Time domain signal of axle deflections obtained from each simulation case was converted to frequency domain by means of fast Fourier transform algorithm (FFT), allowing to observe its harmonic components.

Time domain signals at the same measuring point (MP_1) in both models (solid FE and beam FE model) with 30% deep crack at same locations ($C1$) are presented in Figure 3.31 for solid axle. For both vertical and horizontal deflection of the axle, a good agreement between the two models is observed in terms of the waveform of time domain signals and also in terms of the peak-peak amplitude of the signals, although slight deviations are observed at specific angular positions.

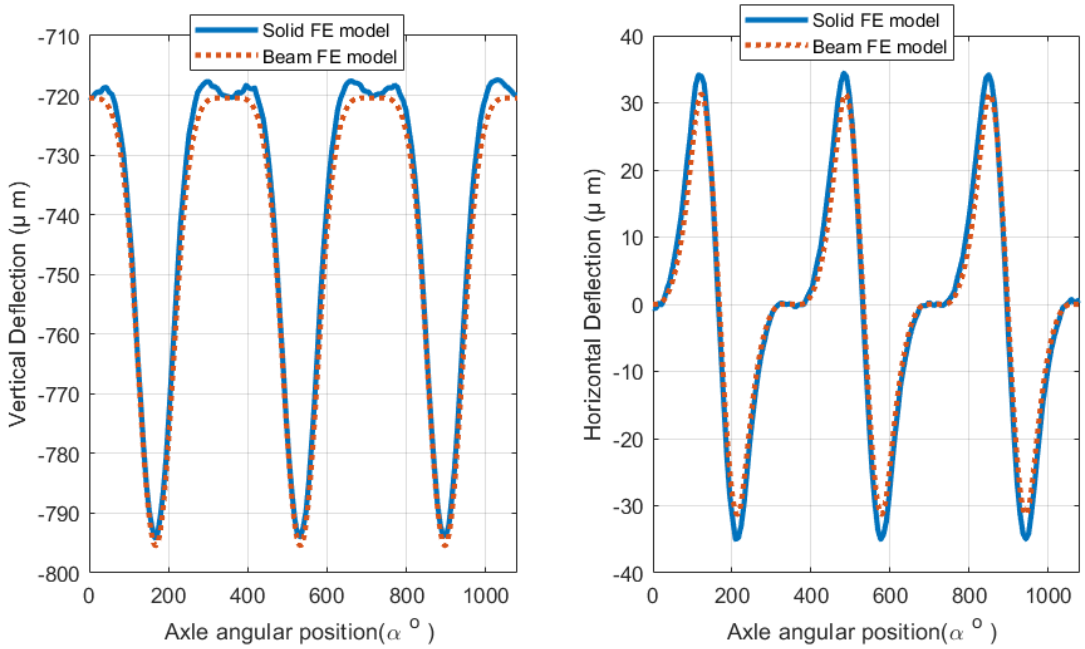

Figure 3.31: *Comparison between beam FE model results and solid FE model results at same measuring section (MP_1) for solid axle with 30% crack at location 1 (left: vertical deflection; right: horizontal deflection).*

In order to further extend the comparison, the time domain signals were computed for different crack sizes considering the same crack location. Table 3.4 shows the maximum deviation of the two results expressed for each case as a percentage of the peak-to-peak amplitude. The maximum deviations are below 7% and 4% for vertical and horizontal deflection respectively and tend to decrease with increase the size of the crack.

Table 3.4: *Maximum percentage deviation of beam FE model and solid FE model results from time domain signals*

Crack Size (%)	Maximum Vertical Deviation (%)	Maximum Horizontal Deviation (%)
10	-6.5	-4.0
20	-5.0	-3.5
30	-2.0	-3.0
40	-2.3	-2.7
50	2.2	2.2

Furthermore, the time domain signals were converted to frequency domain by means of FFT, allowing to obtain the spectra for each crack size signal and to analyse the trend with crack size of different harmonic components. The trends of the first three harmonics are compared in Figure 3.32 for the two models, considering again the vertical and horizontal deflection of the axle. The results presented in Figure 3.32 are in good agreement with each other for the all three harmonics and across the entire range of crack size considered, leading to the conclusion that the simple model based on Timoshenko beam elements is able to capture the crack breathing mechanism and the resulting vibration of the axle with satisfactory accuracy, compared to the model based on solid Finite Elements which is much more complex. It's worth noting that the vibration components in vertical and horizontal direction increase as the crack propagates deeper.

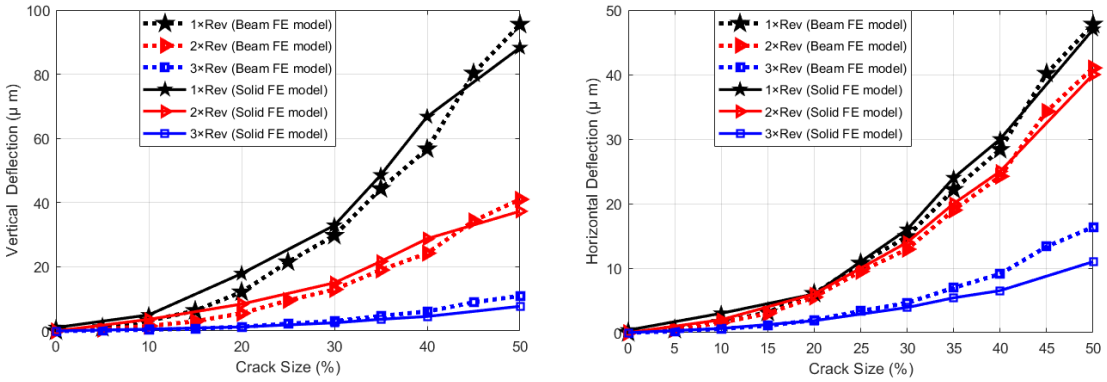

Figure 3.32: *Trends of first three harmonics for crack at location 1 of solid axle for beam FE and solid FE models results measured at section MP_1 (left: vertical harmonics; right: horizontal harmonics).*

3.5.4 Results at different crack locations

In this section, the vibration caused by the crack is analysed considering different crack locations and different measuring points, as shown in Figure 3.10. The loads and boundary conditions of this case are presented in Figure 3.5. Time domain signals of vertical and horizontal vibrations for solid axle are introduced in Figures 3.33 and 3.35, respectively. Each row of these figures subplots represents the same crack location results at different measuring points and each column represent different crack locations results at the same measuring point and the all subplots have the same scale in each figure. It's worth mentioning that every subplot presents eleven vibration signals for crack size varying from 0% till 50% with step 5%.

The results were obtained in time domain for each simulation case and then converted to frequency domain by using FFT, allowing to obtain the signals spectra, as shown in the examples introduced in Figures 3.34 and 3.36 for vertical and horizontal signals, respectively, and track the signals harmonics change with the crack propagation. The results reveal that the presence of a crack at any location of the railway axle perturbs the axle's vertical and horizontal vibrations and the vibration amplitude increases as the crack size increases.

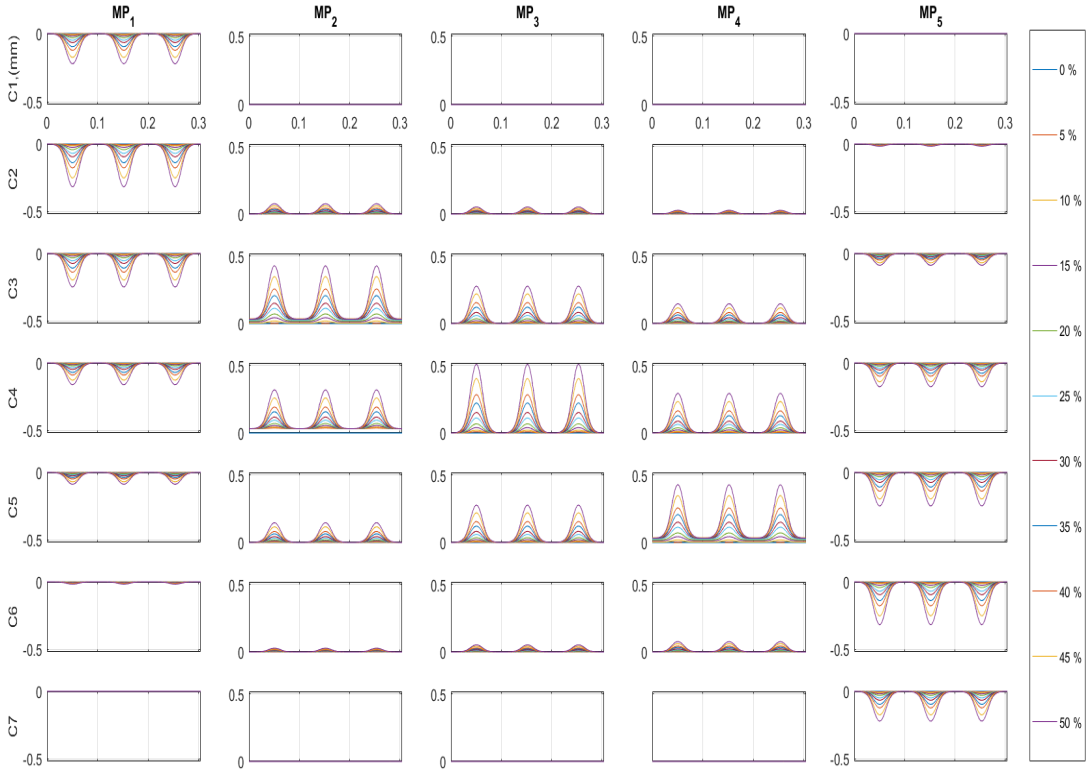

Figure 3.33: *Vertical time domain signals of solid axle (x axis in seconds and y axis in mm and all subplots have the same scale).*

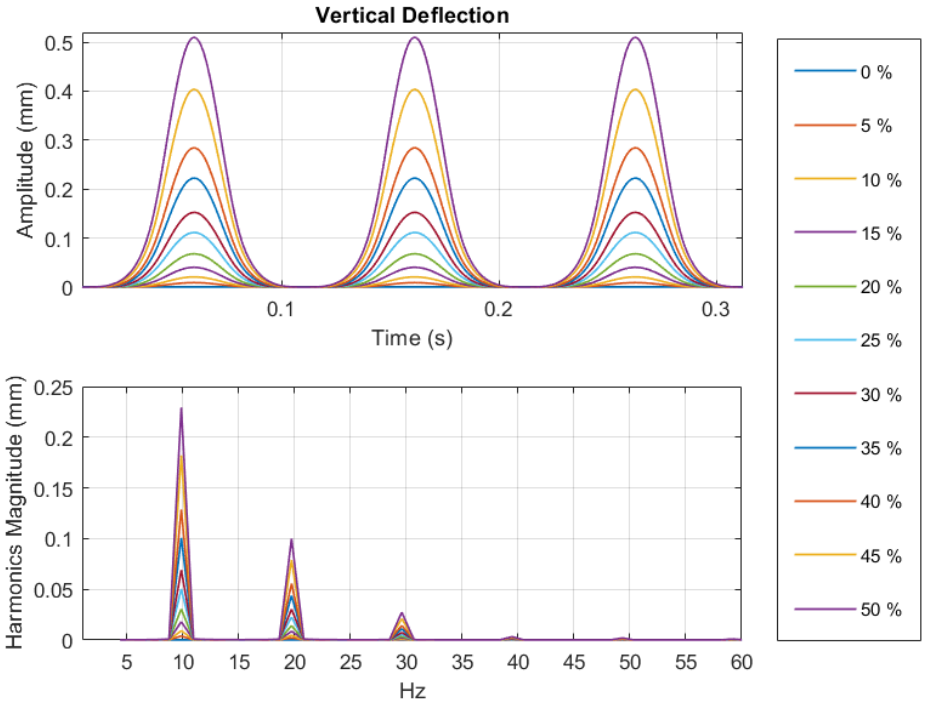

Figure 3.34: *Example of vertical deflection spectra measured at MP_3 for different crack sizes at $C4$.*

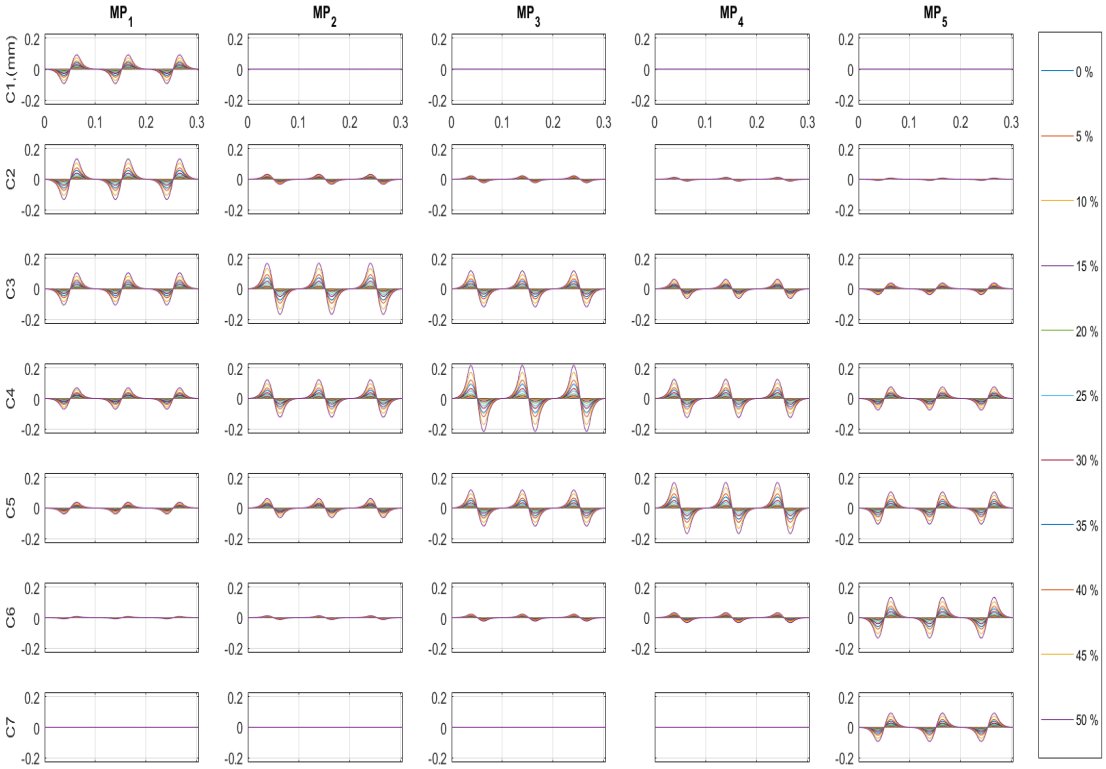

Figure 3.35: *Horizontal time domain signals of solid axle (x axis in seconds and y axis in mm and all subplots have the same scale).*

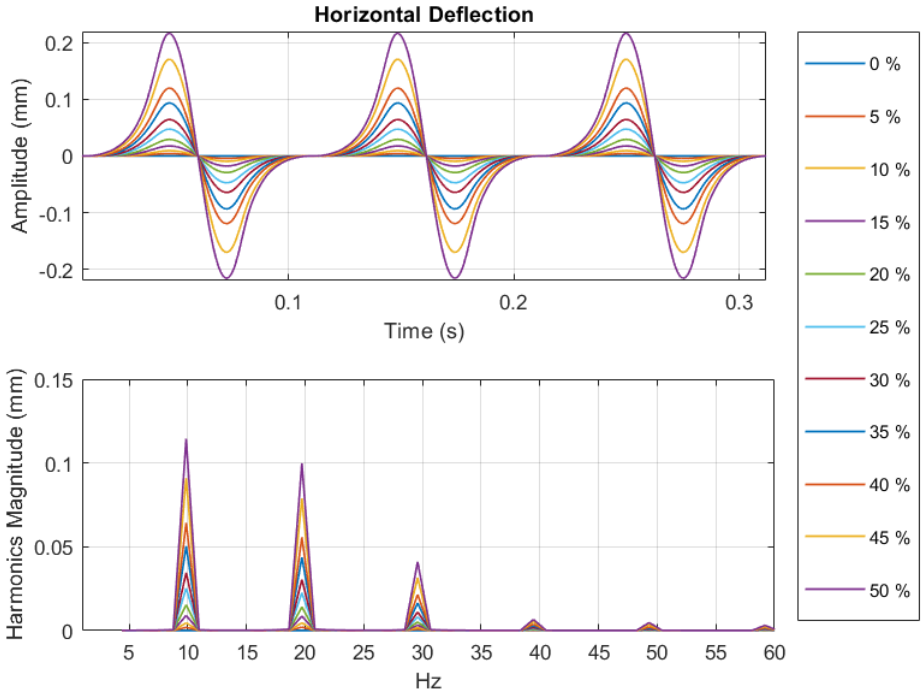

Figure 3.36: *Example of horizontal deflection spectra measured at MP_3 for different crack sizes at $C4$.*

The results obtained from measuring point 1 reveal that this point can be used to measure the influence of a crack at locations 1, 2, 3, 4, and 5, and the same can be noted for measuring point 5 which can detect the effect of a crack at locations 7, 6, 5, 4, and 3. Therefore, it is concluded that the measuring points 1 and 5, where the axle-boxes are mounted, can be used to monitor the presence of a crack at any place in the axle as well as to estimate the crack location.

The trends of the first three harmonics of vertical and horizontal directions vibrations of solid axle, presented in Figures 3.33 and 3.35, are shown in Figure 3.37. Due to symmetry, only results of crack locations 1, 2, 3 and 4 are shown in this figure.

Same simulations have been carried out on the hollow axle where the same crack locations and the same measuring points were considered.

The results of the solid axle (shown in Figures 3.33, 3.35 and 3.37) and the hollow one reveal some important issues:

- The amplitudes of the axle vibration components in vertical and horizontal directions depend on:
  1. The crack size (the amplitude increase as the crack propagates deeper).
  2. The axial position of the cracked section with respect to the measuring section.
  3. The mechanical and geometrical characteristics of the axle (the hollow axle is more flexible than the solid one [60]).
- The 1xRev excitation is higher (approximately double) in vertical direction than in horizontal direction, at any crack size.
- The 2xRev is almost equal in both directions, at any crack size.
- The 3xRev is slightly higher in horizontal direction than in vertical direction, at any crack size.
- The axle-boxes measurements (MP_1 and MP_5) can be used to detect crack at any positions along the axle as well as to estimate its location.

3.5.5 Results of cracked axle considering wheel OOR disturbance

The details of this cracked axle model is shown in Figure 3.6. In these simulations results, after obtaining the vibration signals in time domain, a filter was applied to eliminate the effect of low frequency component introduced by small changing of track irregularity (below $1\times$Rev harmonic component). For this reason, a bandpass filter, sixth order inverted Chebyshev filter, was applied with 5 Hz low cutoff frequency and 100 Hz high cutoff frequency. Then, the filtered signals converted to frequency domain by means of FFT.

The trends of first three harmonics of acceleration signals for solid axle are presented in Figure 3.38 for vertical direction and in Figure 3.39 for horizontal direction. Due to symmetry, the results of crack locations 1, 2, 3 and 4 are shown in the figures.

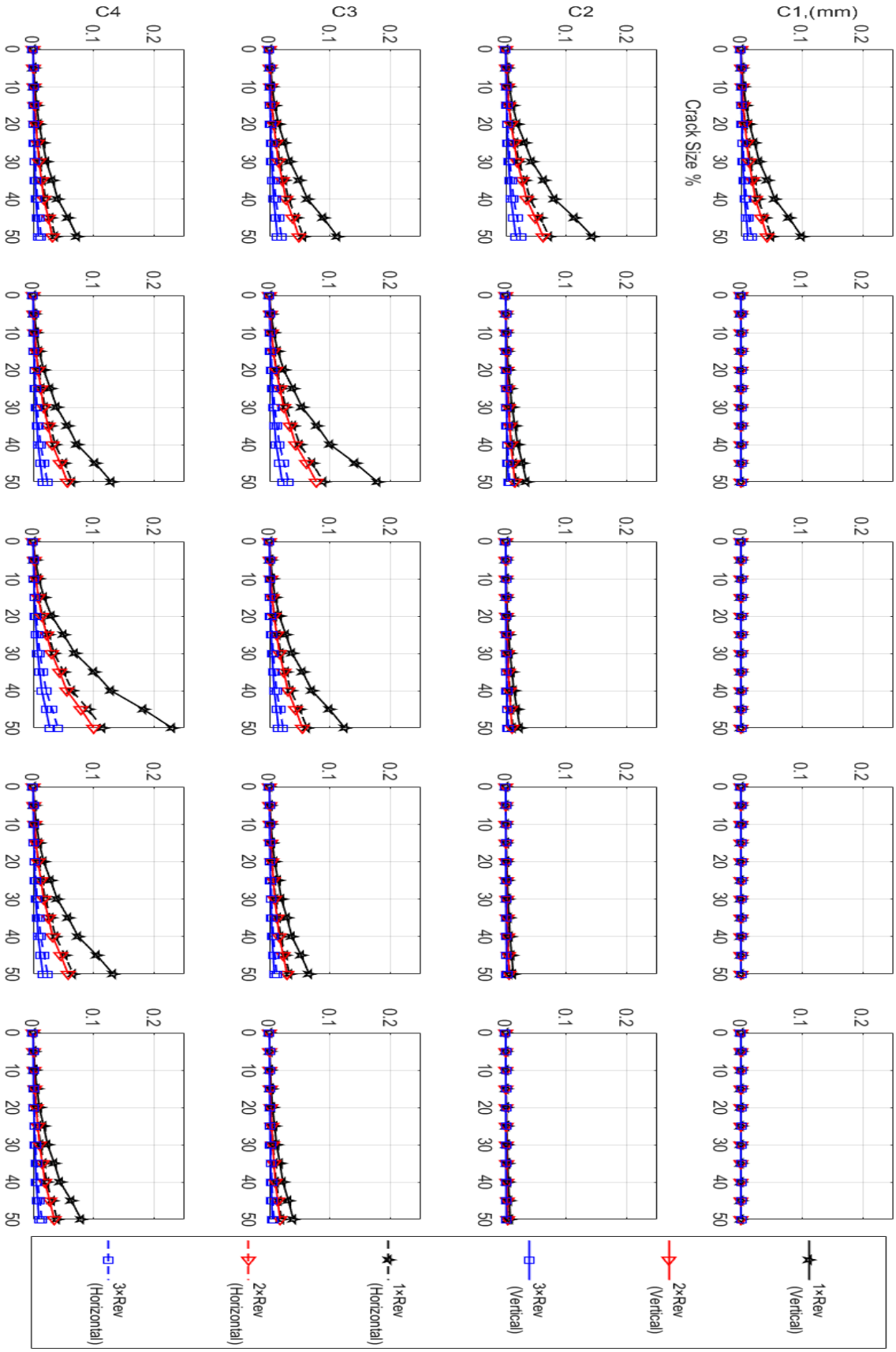

Figure 3.37: *Vertical and horizontal harmonics components trends for solid axle.*

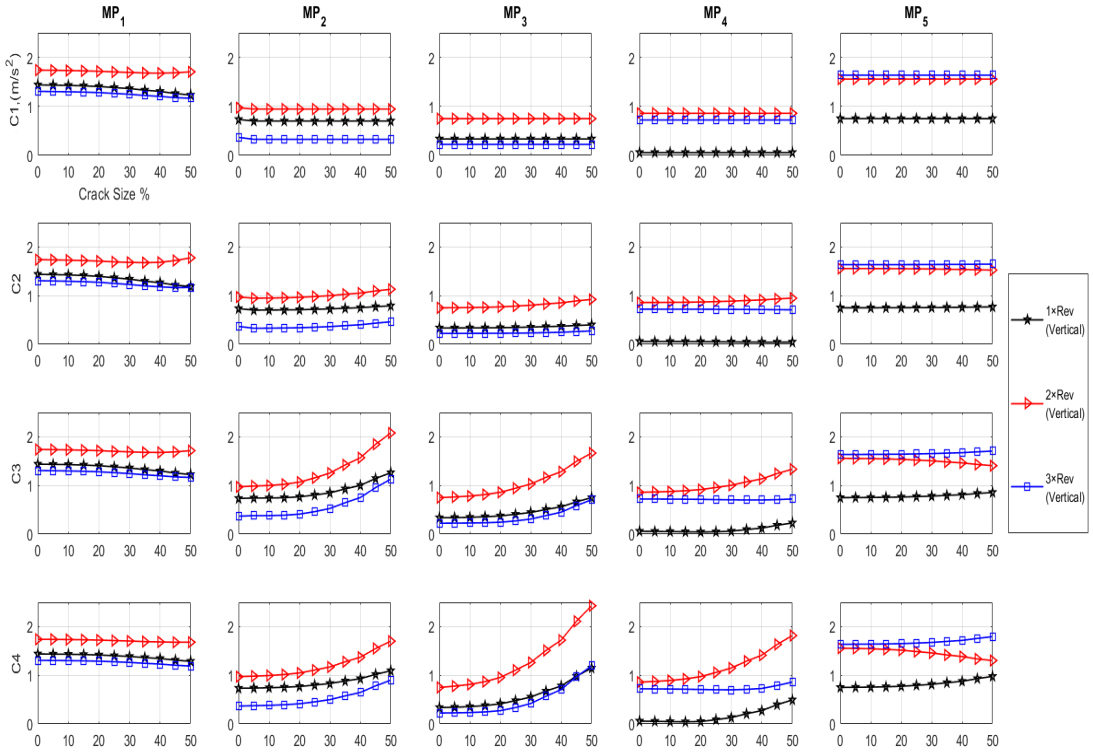

Figure 3.38: *Trends of vertical acceleration harmonics of solid axle.*

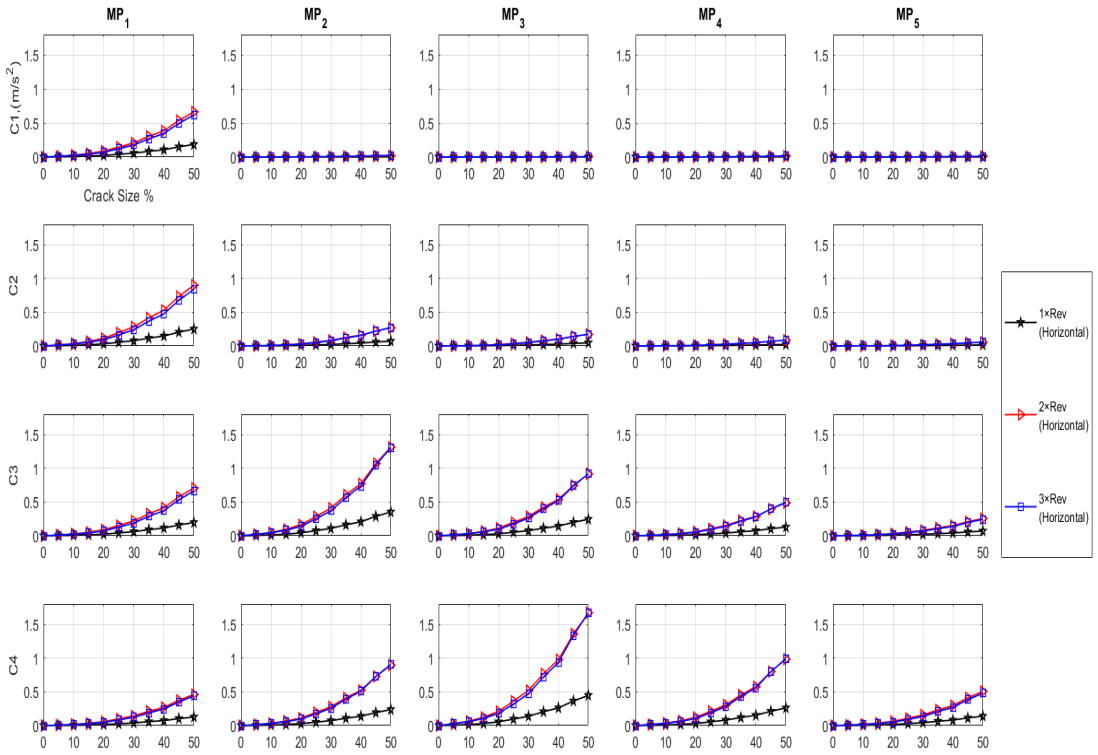

Figure 3.39: *Trends of horizontal acceleration harmonics of solid axle.*

As far as the harmonics of the vertical acceleration are concerned, the effect of wheel OOR disturbance appears to have a great effect on all harmonics considered especially for crack locations close to the wheel ($C1$ and $C2$). This effect decreases in the signals measured at the intermediate measuring points ($MP_{2\sim4}$) for crack locations far from the wheel ($C3$ and $C4$) and with sizes greater than 20%. On the other hand, The harmonic components of the horizontal acceleration are weakly affected by wheel OOR disturbance and show a clear monotonic trend with increasing size of the crack at any location.

In comparison with the horizontal displacement harmonics trends introduced in Figure 3.37, the second and third harmonics amplitudes of the horizontal acceleration shown in Figure 3.39 are higher than the first one due to the frequency influence affecting the acceleration amplitude.

From this case of simulations, we can conclude that the harmonics of the horizontal acceleration are weakly affected by wheel OOR disturbance and therefore a crack detection criterion based on monitoring these quantities can be robust towards the effect of this important disturbance. On the contrary, the results of the vertical acceleration show that this signal is highly affected by wheel OOR disturbance.

CHAPTER 4

Multi-body model of railway vehicle including finite element model of one cracked axle (MB-FE model)

The railway axle health monitoring technique proposed in this work needs to take into account properly the effect of different sources of disturbances, e.g. track irregularity, track flexibility and wheel OOR disturbance, as well as the wheel-rail contact dynamics. In order to analyse these effects, more realistic boundary conditions than the ones used in the models introduced in Chapter 3 need to be considered for the wheelset. A multi-body (MB) model of a railway vehicle also considering track flexibility is merged with the Timoshenko beam FE model of one cracked axle, presented in Section 3.3, to form a detailed model of a railway vehicle with one cracked axle as shown in Figure 4.1. However, this is not possible for the solid FE model, due to its complexity.

In this model, called MB-FE model, the model of crack breathing mechanism defined in Section 3.3.2 is applied to a specific beam element, depending on the crack location, as in the exemplary case shown in Figure 4.1 where the crack is supposed to be located in the centre of the fourth wheelset axle. Therefore, a totally new simulation tool enabling to consider the effects on wheelset vibration jointly caused by the presence of a crack in the axle and by the usual train-track interaction phenomena such as excitation from track flexibility, rail corrugation and wheel OOR has been created.

Table 4.1 shows the independent coordinates of the vehicle and track model, which are added to the nodal coordinates of the cracked axle defined by Equation 3.6. The MB-FE model consist of different models including vehicle MB model (including car body, two bogies and three wheelsets) with 21 degrees of freedom (DOF) in total and track models with 36 DOF (9 DOF per wheelset), whereas the Timoshenko beam FE model of the fourth wheelset has 180 DOF (30 nodes, 6 DOF for each node). Therefore, the MB-FE model has a total of 237 DOF and it can change depending on the number of nodes considered in the beam FE model for different mesh density.

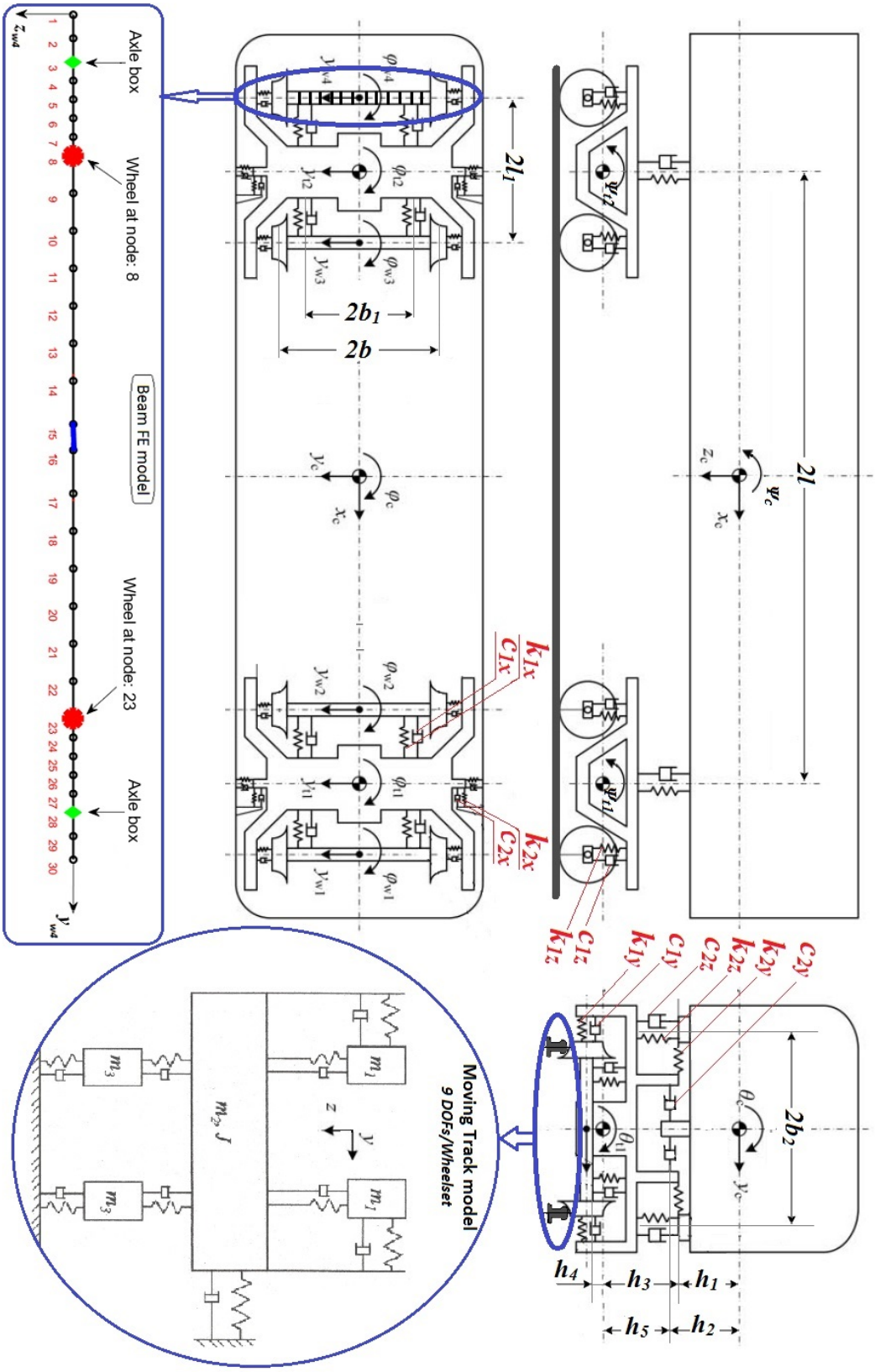

Figure 4.1: *Railway vehicle multi body model including beam FE model of one cracked axle and moving track model.*

Table 4.1: *Independent coordinates of the MB-FE model*

Component / DOF	Vertical	Lateral	Yaw	Pitch	Roll
Car body	z_c	y_c	φ_c	ψ_c	θ_c
Leading bogie	z_{t1}	y_{t1}	φ_{t1}	ψ_{t1}	θ_{t1}
Trailing bogie	z_{t2}	y_{t2}	φ_{t2}	ψ_{t2}	θ_{t2}
Wheelset 1∼3		$y_{w1\sim3}$	$\varphi_{w1\sim3}$		
Wheelset 4	Beam FE model				
Right rail 1∼4 (m_1)	$z_{r1\sim4}$	$y_{r1\sim4}$			
Left rail 1∼4 (m_1)	$z_{l1\sim4}$	$y_{l1\sim4}$			
Sleeper 1∼4 (m_2, J)	$z_{s1\sim4}$	$y_{s1\sim4}$			$\theta_{s1\sim4}$
Right ballast 1∼4 (m_3)	$z_{br1\sim4}$				
Left ballast 1∼4 (m_3)	$z_{bl1\sim4}$				

More details about the MB-FE model and its results are presented in the next sections.

4.1 MB-FE model

4.1.1 Railway vehicle MB model

The governing equations of the railway vehicle dynamics are introduced as follows, considering the notation for the independent coordinates introduced by Table 4.1.

(a) Car body dynamics:

$$m_c\ddot{z}_c + 2k_{2z}(2z_c - z_{t1} - z_{t2}) + 2c_{2z}(2\dot{z}_c - \dot{z}_{t1} - \dot{z}_{t2}) = m_c g \tag{4.1}$$

$$\begin{aligned} &m_c\ddot{y}_c + 2k_{2y}(2y_c - 2h_1\theta_c - y_{t1} - y_{t2} - h_3\theta_{t1} - h_3\theta_{t2}) \\ &\quad + 2c_{2y}(2\dot{y}_c - 2h_1\dot{\theta}_c - \dot{y}_{t1} - \dot{y}_{t2} - h_3\dot{\theta}_{t1} - h_3\dot{\theta}_{t2}) = 0 \end{aligned} \tag{4.2}$$

$$\begin{aligned} &J_{cz}\ddot{\varphi}_c + 2k_{2y}l(2l\varphi_c - y_{t1} + y_{t2} - h_3(\theta_{t1} - \theta_{t2})) \\ &\quad + 2c_{2y}l(2l\dot{\varphi}_c - \dot{y}_{t1} + \dot{y}_{t2} - h_3(\dot{\theta}_{t1} - \dot{\theta}_{t2})) \\ &\quad + 2k_{2x}b_2^2(\varphi_c - \varphi_{t1}) + 2c_{2x}b_2^2(\dot{\varphi}_c - \dot{\varphi}_{t1}) \\ &\quad + 2k_{2x}b_2^2(\varphi_c - \varphi_{t2}) + 2c_{2x}b_2^2(\dot{\varphi}_c - \dot{\varphi}_{t2}) = 0 \end{aligned} \tag{4.3}$$

$$\begin{aligned} &J_{cy}\ddot{\psi}_c + 2k_{2x}h_1(2h_1\psi_c + h_3(\psi_{t1} + \psi_{t2})) \\ &\quad + 2c_{2x}h_1(2h_1\dot{\psi}_c + h_3(\dot{\psi}_{t1} + \dot{\psi}_{t2})) \\ &\quad + 2k_{2z}l(2l\psi_c + z_{t1} - z_{t2}) + 2c_{2z}l(2l\dot{\psi}_c + \dot{z}_{t1} - \dot{z}_{t2}) = 0 \end{aligned} \tag{4.4}$$

$$\begin{aligned} &J_{cx}\ddot{\theta}_c - 2k_{2y}h_1(2y_c - 2h_1\theta_c - y_{t1} - y_{t2} - h_3(\theta_{t1} + \theta_{t2})) \\ &\quad - 2c_{2y}h_1(2\dot{y}_c - 2h_1\dot{\theta}_c - \dot{y}_{t1} - \dot{y}_{t2} - h_3(\dot{\theta}_{t1} + \dot{\theta}_{t2})) \\ &\quad + 2k_{2z}b_2^2(\theta_c - \theta_{t1}) + 2c_{2z}b_2^2(\dot{\theta}_c - \dot{\theta}_{t1}) \\ &\quad + 2k_{2x}b_2^2(\theta_c - \theta_{t2}) + 2c_{2x}b_2^2(\dot{\theta}_c - \dot{\theta}_{t2}) = 0 \end{aligned} \tag{4.5}$$

(b) Leading bogie dynamics:

$$\begin{aligned} & m_t\ddot{z}_{t1} - 2k_{2z}(z_c - l\varphi_c - z_{t1}) - 2c_{2z}(\dot{z}_c - l\dot{\varphi}_c - \dot{z}_{t1}) \\ & \quad + k_{1z}(4z_{t1} - \frac{b_1}{b}(z_{1r} + z_{2r} + z_{1l} + z_{2l})) \\ & \quad + c_{1z}(4\dot{z}_{t1} - \frac{b_1}{b}(\dot{z}_{1r} + \dot{z}_{2r} + \dot{z}_{1l} + \dot{z}_{2l})) = m_t g \end{aligned} \tag{4.6}$$

$$\begin{aligned} & m_t\ddot{y}_{t1} - 2k_{2y}(y_c + l\varphi_c - h_1\theta_c - y_{t1} - h_3\theta_{t1}) \\ & \quad - 2c_{2y}(\dot{y}_c + l\dot{\varphi}_c - h_1\dot{\theta}_c - \dot{y}_{t1} - h_3\dot{\theta}_{t1}) \\ & \quad + 2k_{1y}(2y_{t1} - 2h_4\theta_{t1} - y_{w1} - y_{w2}) \\ & \quad + 2c_{1y}(2\dot{y}_{t1} - 2h_4\dot{\theta}_{t1} - \dot{y}_{w1} - \dot{y}_{w2}) = 0 \end{aligned} \tag{4.7}$$

$$\begin{aligned} & J_{tz}\ddot{\varphi}_{t1} - 2k_{2x}b_2^2(\varphi_c - \varphi_{t1}) - 2c_{2x}b_2^2(\dot{\varphi}_c - \dot{\varphi}_{t1}) \\ & \quad + 2k_{1y}l_1(2l_1\varphi_{t1} - y_{w1} + y_{w2}) \\ & \quad + 2c_{1y}l_1(2l_1\dot{\varphi}_{t1} - \dot{y}_{w1} + \dot{y}_{w2}) \\ & \quad + 2k_{1x}b_1^2(\varphi_{t1} - \varphi_{w1}) + 2c_{1x}b_1^2(\dot{\varphi}_{t1} - \dot{\varphi}_{w1}) \\ & \quad + 2k_{1x}b_1^2(\varphi_{t1} - \varphi_{w2}) + 2c_{1x}b_1^2(\dot{\varphi}_{t1} - \dot{\varphi}_{w2}) = 0 \end{aligned} \tag{4.8}$$

$$\begin{aligned} & J_{ty}\ddot{\psi}_{t1} + 2k_{2x}h_3(h_1\psi_c + h_3\psi_{t1}) + 2c_{2x}h_3(h_1\dot{\psi}_c + h_3\dot{\psi}_{t1}) \\ & \quad + 4k_{1x}h_4^2\psi_{t1} + 4c_{1x}h_4^2\dot{\psi}_{t1} \\ & \quad + k_{1z}l_1(4l_1\psi_{t1} + \frac{b_1}{b}(z_{1r} + z_{1l} - z_{2r} - z_{2l})) \\ & \quad + c_{1z}l_1(4l_1\dot{\psi}_{t1} + \frac{b_1}{b}(\dot{z}_{1r} + \dot{z}_{1l} - \dot{z}_{2r} - \dot{z}_{2l})) = 0 \end{aligned} \tag{4.9}$$

$$\begin{aligned} & J_{tx}\ddot{\theta}_{t1} - 2k_{2y}h_3(y_c + l\varphi_c - h_1\theta_c - y_{t1} - h_3\theta_{t1}) \\ & \quad - 2c_{2y}h_3(\dot{y}_c + l\dot{\varphi}_c - h_1\dot{\theta}_c - \dot{y}_{t1} - h_3\dot{\theta}_{t1}) \\ & \quad - 2k_{2z}b_2^2(\theta_c - \theta_{t1}) - 2c_{2z}b_2^2(\dot{\theta}_c - \dot{\theta}_{t1}) \\ & \quad - 2k_{1y}h_4(2y_{t1} - 2h_4\theta_{t1} - y_{w1} - y_{w2}) \\ & \quad - 2c_{1y}h_4(2\dot{y}_{t1} - 2h_4\dot{\theta}_{t1} - \dot{y}_{w1} - \dot{y}_{w2}) \\ & \quad + k_{1z}b_1(4b_1\theta_{t1} - \frac{b_1}{b}(z_{1r} + z_{2r} - z_{1l} - z_{2l})) \\ & \quad + c_{1z}b_1(4b_1\dot{\theta}_{t1} - \frac{b_1}{b}(\dot{z}_{1r} + \dot{z}_{2r} - \dot{z}_{1l} - \dot{z}_{2l})) = 0 \end{aligned} \tag{4.10}$$

(b) Trailing bogie dynamics:

$$\begin{aligned} & m_t\ddot{z}_{t2} - 2k_{2z}(z_c - l\varphi_c - z_{t2}) - 2c_{2z}(\dot{z}_c - l\dot{\varphi}_c - \dot{z}_{t2}) \\ & \quad + k_{1z}(4z_{t2} - \frac{b_1}{b}(z_{3r} + z_{4r} + z_{3l} + z_{4l})) \\ & \quad + c_{1z}(4\dot{z}_{t2} - \frac{b_1}{b}(\dot{z}_{3r} + \dot{z}_{4r} + \dot{z}_{3l} + \dot{z}_{4l})) = m_t g \end{aligned} \tag{4.11}$$

$$\begin{aligned} & m_t\ddot{y}_{t2} - 2k_{2y}(y_c + l\varphi_c - h_1\theta_c - y_{t2} - h_3\theta_{t2}) \\ & \quad - 2c_{2y}(\dot{y}_c + l\dot{\varphi}_c - h_1\dot{\theta}_c - \dot{y}_{t2} - h_3\dot{\theta}_{t2}) \\ & \quad + 2k_{1y}(2y_{t2} - 2h_4\theta_{t2} - y_{w3} - y_{w4}) \\ & \quad + 2c_{1y}(2\dot{y}_{t2} - 2h_4\dot{\theta}_{t2} - \dot{y}_{w3} - \dot{y}_{w4}) = 0 \end{aligned} \tag{4.12}$$

$$\begin{aligned} & J_{tz}\ddot{\varphi}_{t2} - 2k_{2x}b_2^2(\varphi_c - \varphi_{t2}) - 2c_{2x}b_2^2(\dot{\varphi}_c - \dot{\varphi}_{t2}) \\ & \quad + 2k_{1y}l_1(2l_1\varphi_{t2} - y_{w3} + y_{w4}) \\ & \quad + 2c_{1y}l_1(2l_1\dot{\varphi}_{t2} - \dot{y}_{w3} + \dot{y}_{w4}) \\ & \quad + 2k_{1x}b_1^2(\varphi_{t2} - \varphi_{w3}) + 2c_{1x}b_1^2(\dot{\varphi}_{t2} - \dot{\varphi}_{w3}) \\ & \quad + 2k_{1x}b_1^2(\varphi_{t2} - \varphi_{w4}) + 2c_{1x}b_1^2(\dot{\varphi}_{t2} - \dot{\varphi}_{w4}) = 0 \end{aligned} \tag{4.13}$$

$$\begin{aligned} & J_{ty}\ddot{\psi}_{t2} + 2k_{2x}h_3(h_1\psi_c + h_3\psi_{t2}) + 2c_{2x}h_3(h_1\dot{\psi}_c + h_3\dot{\psi}_{t2}) \\ & \quad + 4k_{1x}h_4^2\psi_{t2} + 4c_{1x}h_4^2\dot{\psi}_{t2} \\ & \quad + k_{1z}l_1(4l_1\psi_{t2} + \frac{b_1}{b}(z_{3r} + z_{3l} - z_{4r} - z_{4l})) \\ & \quad + c_{1z}l_1(4l_1\dot{\psi}_{t2} + \frac{b_1}{b}(\dot{z}_{3r} + \dot{z}_{3l} - \dot{z}_{4r} - \dot{z}_{4l})) = 0 \end{aligned} \tag{4.14}$$

$$\begin{aligned} & J_{tx}\ddot{\theta}_{t2} - 2k_{2y}h_3(y_c + l\varphi_c - h_1\theta_c - y_{t2} - h_3\theta_{t2}) \\ & \quad - 2c_{2y}h_3(\dot{y}_c + l\dot{\varphi}_c - h_1\dot{\theta}_c - \dot{y}_{t2} - h_3\dot{\theta}_{t2}) \\ & \quad - 2k_{2z}b_2^2(\theta_c - \theta_{t2}) - 2c_{2z}b_2^2(\dot{\theta}_c - \dot{\theta}_{t2}) \\ & \quad - 2k_{1y}h_4(2y_{t2} - 2h_4\theta_{t2} - y_{w3} - y_{w4}) \\ & \quad - 2c_{1y}h_4(2\dot{y}_{t2} - 2h_4\dot{\theta}_{t2} - \dot{y}_{w3} - \dot{y}_{w4}) \\ & \quad + k_{1z}b_1(4b_1\theta_{t2} - \frac{b_1}{b}(z_{3r} + z_{4r} - z_{3l} - z_{4l})) \\ & \quad + c_{1z}b_1(4b_1\dot{\theta}_{t2} - \frac{b_1}{b}(\dot{z}_{3r} + \dot{z}_{4r} - \dot{z}_{3l} - \dot{z}_{4l})) = 0 \end{aligned} \tag{4.15}$$

(c) Wheelsets dynamics (when $i = 1, j = 1; 2$ and $i = 2, j = 3$):

$$\begin{aligned} m_w\ddot{y}_{wj} &- 2k_{1y}(y_{ti} - (-1)^j l_1\varphi_{ti} - h_4\theta_{ti} - y_{wj}) \\ &- 2c_{1y}(\dot{y}_{ti} - (-1)^j l_1\dot{\varphi}_{ti} - h_4\dot{\theta}_{ti} - \dot{y}_{wj}) \\ &+ 2f_{22}\left[\frac{\dot{y}_{wj}}{V}(1 + \frac{\sigma r_w}{b}) - \varphi_{wj}\right] + k_{gy}y_{wj} \\ &= 2f_{22}\left[\frac{\sigma r_w}{Vb}\dot{y}_{aj} + \frac{\sigma r_w^2}{Vb}\dot{\theta}_{clj}\right] + k_{gy}(y_{aj} + r_w\theta_{clj}) \end{aligned} \tag{4.16}$$

$$\begin{aligned} J_{wz}\ddot{\varphi}_{wj} &+ 2k_{1x}b_1^2(\varphi_{wj} - \varphi_{ti}) + 2c_{1x}b_1^2(\dot{\varphi}_{wj} - \dot{\varphi}_{ti}) \\ &+ 2f_{11}\left[\frac{b\lambda_e}{r_w}y_{wj} + \frac{b^2}{V}\dot{\varphi}_{wj}\right] - k_{g\varphi}\varphi_{wj} \\ &= 2f_{11}\frac{b\lambda_e}{r_w}(y_{aj} + r_w\theta_{clj}) \end{aligned} \tag{4.17}$$

The definitions and values of MB railway vehicle model parameters, introduced in its governing equations, are given in Tables 4.2, 4.3, 4.4 and 4.5. The parameters values of the MB model are defined according to a freight wagon parameters.

It's worth to clarify that the rigid body equations of motion 4.16 and 4.17 are not considered for the fourth wheelset which is modelled using the Timoshenko beam FE model. Also, the name "horizontal direction" used to describe the vibration signal in the traveling direction of the vehicle, in the previous chapters, is replaced here by "longitudinal direction" for MB-FE results, because this name is more convenient with the multi-body simulations of the railway vehicle.

Table 4.2: *Definitions and values of the masses and moments of inertia used in the MB-FE model*

Component	Symbol	Definition	Value	Unit
Car body	m_c	Mass of car body	80.6×10^3	kg
	J_{cx}	Roll moment of inertia of car body	58.192×10^3	$kg.m^2$
	J_{cy}	Pitch moment of inertia of car body	1.768×10^6	$kg.m^2$
	J_{cz}	Yaw moment of inertia of car body	1.734×10^6	$kg.m^2$
Bogie	m_t	Mass of bogie	1635	kg
	J_{tx}	Roll moment of inertia of bogie	1025	$kg.m^2$
	J_{ty}	Pitch moment of inertia of bogie	875	$kg.m^2$
	J_{tz}	Yaw moment of inertia of bogie	1823	$kg.m^2$
Wheelset	m_w	Mass of wheelset	1254	kg
	J_{wz}	Yaw moment of inertia of wheelset	688	$kg.m^2$

Table 4.3: *Definitions and values of the suspensions parameters used in the MB-FE model*

Component	Symbol	Definition	Value	Unit
Primary suspension	k_{1x}	Primary longitudinal stiffness	0.9×10^6	N/m
	k_{1y}	Primary lateral stiffness	0.9×10^6	N/m
	k_{1z}	Primary vertical stiffness	1.6×10^6	N/m
	c_{1x}	Primary longitudinal damping	1×10^3	Ns/m
	c_{1y}	Primary lateral damping	1×10^3	Ns/m
	c_{1z}	Primary vertical damping	1×10^3	Ns/m
Secondary suspension	k_{2x}	Secondary longitudinal stiffness	5.7×10^7	N/m
	k_{2y}	Secondary lateral stiffness	5.7×10^7	N/m
	k_{2z}	Secondary vertical stiffness	5.7×10^7	N/m
	c_{2x}	Secondary longitudinal damping	0	Ns/m
	c_{2y}	Secondary lateral damping	0	Ns/m
	c_{2z}	Secondary vertical damping	3.2×10^4	Ns/m

Table 4.4: *Definitions and values the dimensions parameters used in the MB-FE model*

Component	Symbol	Definition	Value	Unit
Dimensions	l	Half of bogie centre pin spacing	7.43	m
	l_1	Half of wheelbase	0.9	m
	b	Half of wheelset contact distance	0.75	m
	b_1	Half of primary suspension spacing (lateral)	1	m
	b_2	Half of secondary suspension spacing (lateral)	0	m
	h_1	Vertical distance from car body center of gravity to secondary spring	0.155	m
	h_2	Vertical distance from car body center of gravity to secondary lateral damper	0.155	m
	h_3	Vertical distance from bogie frame center of gravity to secondary spring	0.195	m
	h_4	Vertical distance from bogie frame center of gravity to primary suspension	0.25	m
	h_5	Vertical distance from bogie frame center of gravity to secondary lateral damper	0.195	m
	r_w	Wheel rolling radius	0.46	m

4.1.2 Railway track model

To consider the track and its pertinent flexibility, in vertical and lateral directions, in MB-FE model, so-called "moving track models" [61, 62], are used, introducing one sectional model of the type shown in Figure 4.1 under each wheelset.

The sleeper passing effect, i.e. the periodic variation of track stiffness between a maximum value when the wheelset is over one sleeper and a minimum one when the wheelset is at mid-span between two consecutive sleepers, is considered in the sectional models by periodically varying the track parameters (stiffness, damping and mass) depending on the wheelset position with respect to the sleeper [61].

Table 4.5: *Parameters values and definitions of wheel/rail contact model*

Component	Symbol	Definition	Value	Unit
Wheel/rail parameters	f_{11}	Longitudinal creep coefficient	25798281	
	f_{22}	Lateral creep coefficient	26066493	
	λ_e	Effective wheel conicity	0.015	
	σ	Wheelset roll coefficient	0.5	
	W	Load per wheelset	2.18×10^5	N
Rail track irregularities	$z_{1r} \sim z_{4r}$	Vertical disturbances acting on the right wheels of wheelset $1 \sim 4$		m
	$z_{1l} \sim z_{4l}$	Vertical disturbances acting on the left wheels of wheelset $1 \sim 4$		m
	$y_{1r} \sim y_{4r}$	Lateral disturbances acting on the right wheels of wheelset $1 \sim 4$		m
	$y_{1l} \sim y_{4l}$	Lateral disturbances acting on the left wheels of wheelset $1 \sim 4$		m
	$y_{a1} \sim y_{a4}$	Lateral alignment of wheelset $1 \sim 4$		m
	$\theta_{cl1} \sim \theta_{cl4}$	Cross-level of the track irregularities for wheelset $1 \sim 4$		rad
Other definitions	V	Vehicle speed	100	km/h
	k_{gy}	Lateral gravitational stiffness	$= \frac{W\lambda_e}{b}$	N/m
	$k_{g\varphi}$	Yaw gravitational stiffness	$= -Wb\lambda_e$	N/m

This model is appropriate for investigating the dynamic interaction between the vehicle and the track in a frequency range up to 200 Hz [61]. Considering that for a vehicle moving at 120 km/h the 3xRev frequency is approximately 35 Hz, the frequency range of the model is fully consistent with the scope of this work.

One moving track model is considered under each wheelset, as shown Figure 4.1, and the four moving track models are assumed to follow the longitudinal forward movement of the vehicle. More details about this model and its parameters values can be found in [61].

Figure 4.2 introduces an example of track response, in vertical and lateral directions, due to its flexibility using this moving track model by applying 105 kN static load in vertical direction and 30 kN static load in lateral direction at masses m_1 (see Figure 4.1) for each side of the track and at 100 km/h train speed. Figure 4.2 presents the time history of the track response and its spectrum in both directions evaluated at mass m_1. The effect of sleeper passing is visible in the time history and spectrum of the vertical displacement which shows a single harmonic component at 55.55 Hz corresponding to the sleeper passing frequency (spacing of sleepers equal 0.5 m). No effect of sleeper passing appears in lateral direction, just static deflection can be obtained from this direction due to the effect of the static load.

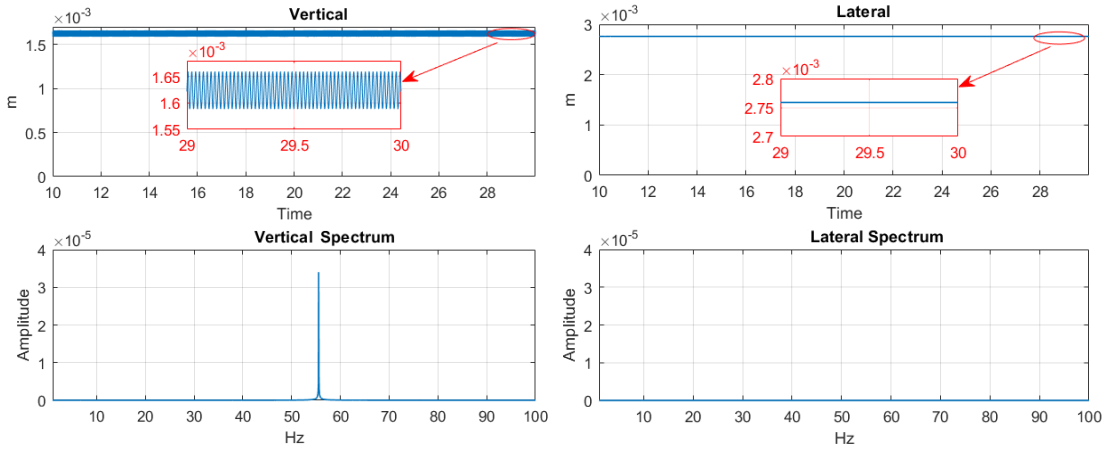

Figure 4.2: *An example of vertical and lateral track response due to its flexibility at train speed 100 km/h and static forces.*

4.1.3 Equation of motion of MB-FE model

The governing equations combining the dynamics of the railway vehicle (MB) integrated with FE model of one axle and the dynamics of the rail track irregularities are developed and arranged in matrices form as:

$$[M_T]\langle \ddot{X} \rangle + [C_T]\langle \dot{X} \rangle + [K_T]\langle X \rangle = \langle F_T \rangle \tag{4.18}$$

$$M_T = \begin{bmatrix} M_{MB} & 0 \\ 0 & M_{FE} \end{bmatrix}; \; C_T = \begin{bmatrix} C_{MB} & c_{cn} \\ c_{cn}^T & C_{FE} \end{bmatrix};$$

$$K_T = \begin{bmatrix} K_{MB} & k_{cn} \\ k_{cn}^T & K_{FE} \end{bmatrix}; \quad F_T = \begin{bmatrix} F_{MB} \\ F_{FE} \end{bmatrix}. \tag{4.19}$$

Where;
- M_T, C_T and K_T: are the mass, damping and stiffness matrices for the entire system (237 DOF).
- M_{MB}, C_{MB} and K_{MB}: Mass, damping and stiffness matrices of the vehicle MB model including the moving track models, for a total of 57 DOF.
- M_{FE}, C_{FE} and K_{FE}: Mass, damping and stiffness matrices for Timoshenko beam FE model of the flexible axle (180 DOF).
- c_{cn} and k_{cn}: damping and stiffness terms of the primary suspension connecting the FE wheelset to the vehicle. The superscript T means the transpose of the matrix.
- X: Vector of independent coordinates, including the coordinates listed in Table 4.1 and the nodal displacements of the Timoshenko beam FE model.
- F_T: Forces vector for the whole model (237 elements).
- F_{MB}: Forces vector acting on the coordinates of the MB model (57 elements).
- F_{FE}: Vector of the nodal forces acting on the Timoshenko beam FE model (180 elements).

Equation (4.18) is solved in time domain using the Newmark method with fixed time step using a code written in MATLAB language.

4.1.4 Irregularities considered in MB-FE model

Two different types of disturbance were considered in MB-FE model, Track geometrical irregularities and wheel OOR.

Railway track geometrical irregularities

Railway track irregularities are due to combinations of initial installation errors, general degradation, cumulative track loading, and low rail joints. Track geometrical variations are the primary inputs to the railway vehicles [63]. The geometrical track irregularities include the vertical profile, cross-level, lateral alignment, and gauge irregularities [64], see Figure 4.3. The lateral alignment (y_a) and cross-level (θ_{cl}) of the track irregularities can be expressed as:

$$y_a = \frac{y_r + y_l}{2} \qquad ; \qquad \theta_{cl} = \frac{z_l - z_r}{2b} \tag{4.20}$$

where; y_r and y_l represent the lateral track irregularities of the right and left rails, respectively; z_r and z_l represent the vertical track irregularities of the right and left rails, respectively, and b is half of wheelset contact distance.

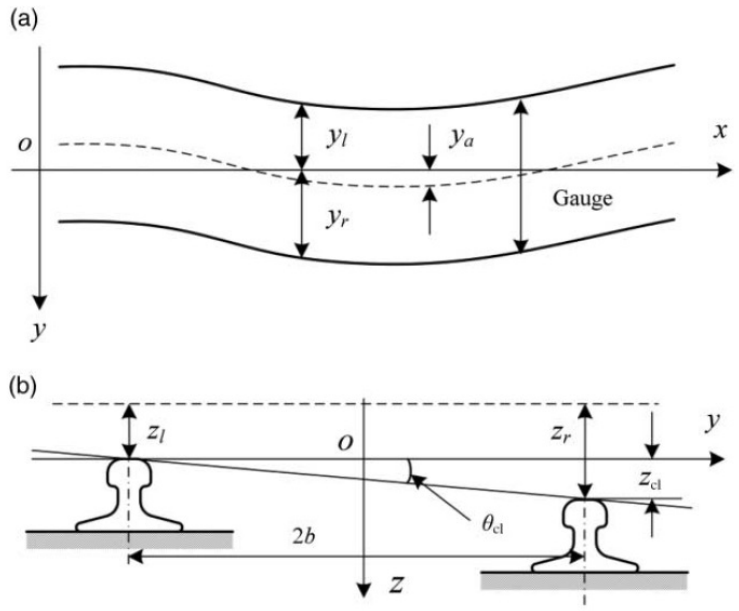

Figure 4.3: *Definitions of the track geometrical irregularities: (a) the lateral alignment and gauge and (b) the vertical profile and cross level [63].*

Random track irregularities in vertical and lateral directions were used in these simulations. The random track irregularities are usually described by their power spectral densities (PSDs), which are determined from the measured data [64]. To obtain a realistic case, vertical level, cross level and lateral alignment track irregularities are considered in these simulation, using random-phase spatial realisations of the power spectral density curves defined as "low level" irregularity by report ORE B 176 [65],

considering wavelengths in the range 0.25 to 25 m. For wavelengths shorter than 3 m, the ORE B 176 spectra are linearly extrapolated [62].

Figure 4.4 presents an example of vertical and lateral irregularities of one side of the track and their spectra.

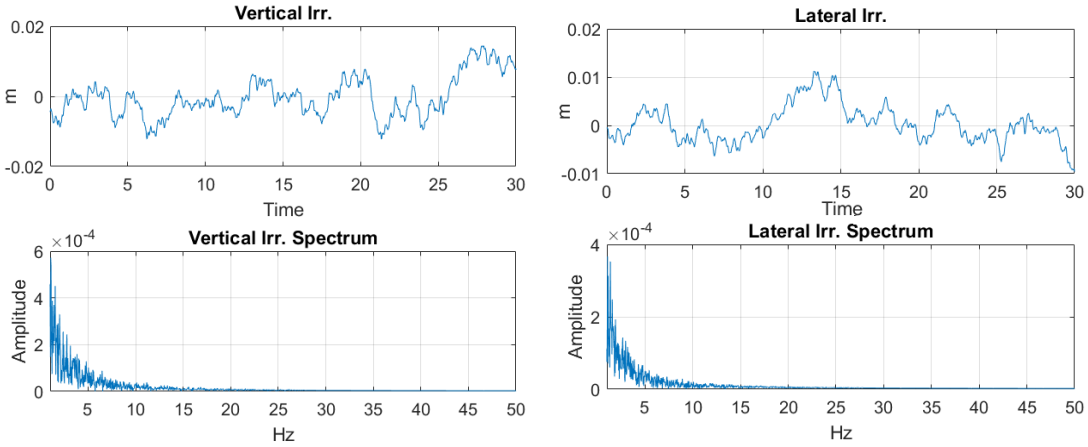

Figure 4.4: *An example of vertical and lateral track irregularities.*

Wheel OOR irregularities

Same model of wheel OOR mentioned in subsection 3.2.8 is used here in the MB-FE model. In that model, the profile of wheel OOR was introduced as a sum of twenty sine functions with wavelengths corresponding to the nominal wheel circumference (2.88 m) and the nineteen lowest sub-multiples. The amplitudes of these components were defined based on the elaboration of experimental measurements of wheel OOR reported in [54] while the phases of the harmonics were generated using different random sets of numbers for each wheel, so to avoid correlation of the OOR profiles obtained on the different wheels.

To investigate further the effect of this very important type of disturbance, other wheel OOR profiles were considered in these analyses using scaling factor up to 2.

4.2 MB-FE model verification

In order to assess to which extent, the MB-FE model can be assumed representative of the actual behavior of the railway vehicle with/without cracked axle, two levels of verification have been carried out. These verification activities allowed to verify that the model is able to reproduce with good accuracy:

1. The rigid-body dynamics of the vehicle without considering any crack in the axle.

2. The dynamics of railway vehicle with one cracked axle and without considering any irregularities to assess the capability of the MB-FE model to reproduce the crack breathing mechanism effect.

4.2.1 First verification level

In this verification level, the MB-FE model, without considering any crack, was validated against Polimi conventional railway vehicle MB software (ADTReS) coded by FORTRAN programming language [62, 66]. To avoid the deformation of the flexible wheelset in this case of simulation, its stiffness has been increased by increasing its modulus of elasticity three times the normal value. The same parameters values and the same track irregularities (vertical, lateral and cross level) were introduced in both models. Simulations were performed considering a vehicle speed of 100 km/h which is realistic for a freight wagon. The time histories of some DOFs of the two models are compared in Figure 4.5.

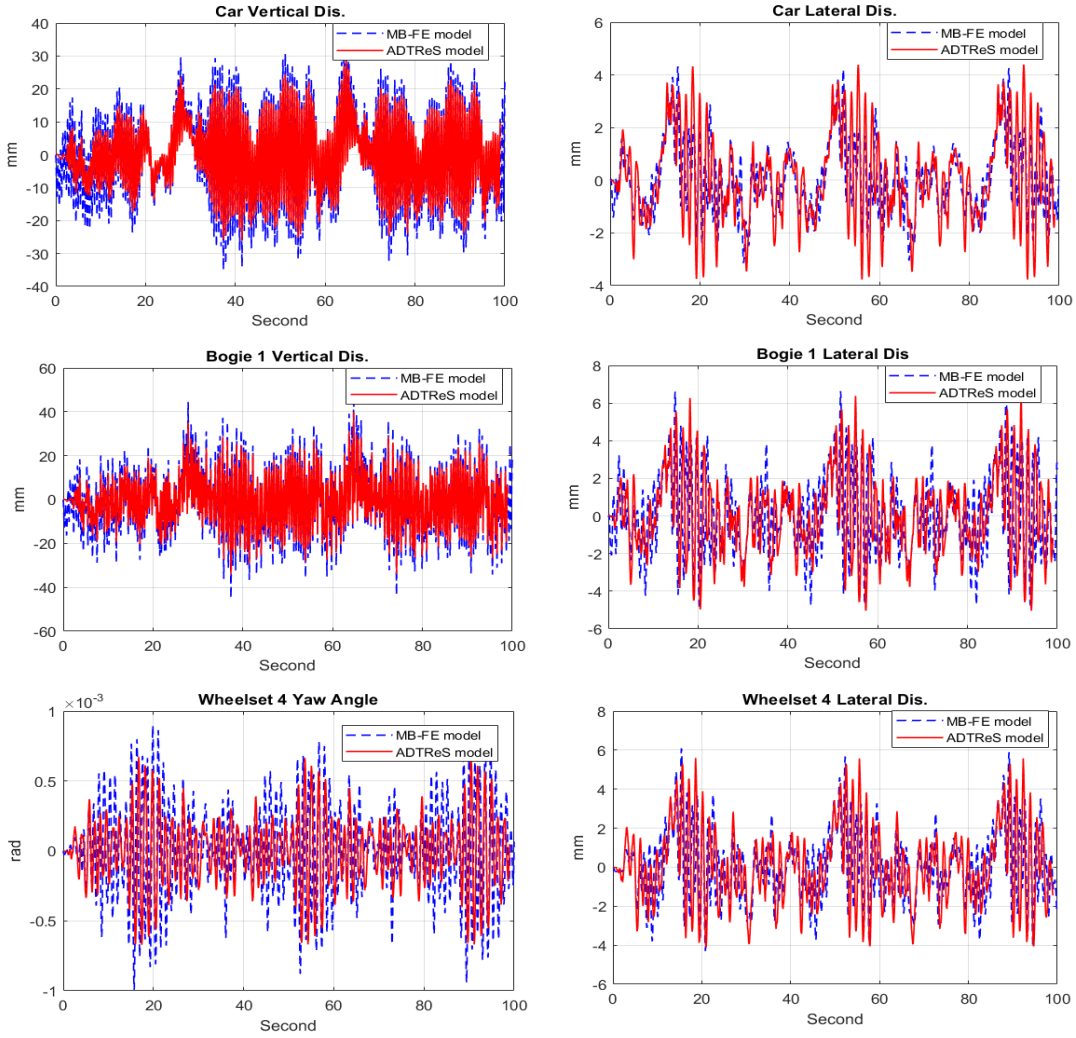

Figure 4.5: *Verification results of MB-FE model (MATLAB) against ADTReS model (FORTRAN).*

Figure 4.5 reveals a good agreement between MB-FE and ADTReS model, although slight differences can be noted in lateral and yaw direction, due to the use of different theories used in the two models to represent the creepage-creep force relationship. In software ADTReS, the Shen-Hedrick-Elkins non-linear model of creep forces [67] is used whilst in the MB-FE model the simpler linear model due to Kalker [67] is used.

4.2.2 Second verification level

In the second verification level, the MB-FE model was used to simulate a vehicle with a crack in the fourth axle running on a track with no irregularity and no wheel OOR disturbance. The results were compared to those obtained for the Timoshenko beam FE model of one single wheelset, introduced in Section 3.3, considering the same crack size and location introduced in the MB-FE model.

In both models, the crack breathing mechanism model was applied to the central element (element 15 in Figures 3.12 and 4.1) and three different crack sizes (0% "No crack", 35% and 50%) were simulated. The vertical and longitudinal displacements of node 15, located at the center of the axle (see Figures 3.12 and 4.1), are compared in Figure 4.6.

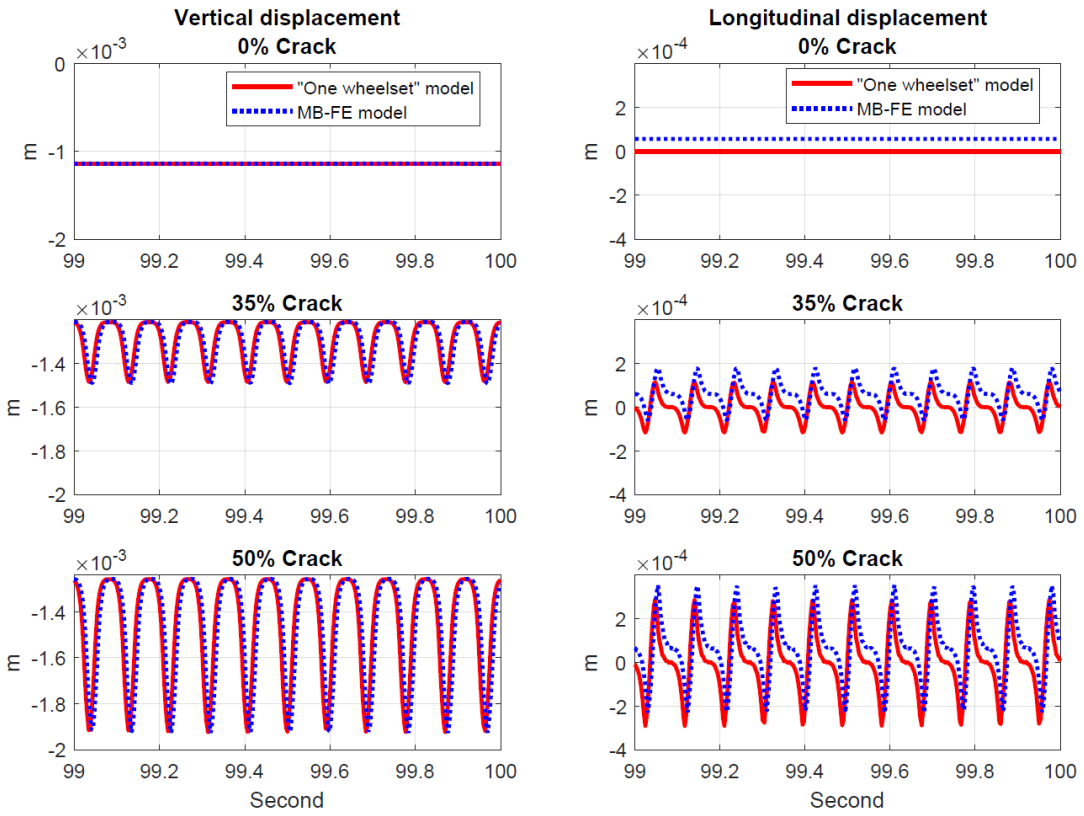

Figure 4.6: *Verification of MB-FE model results against "One Axle" beam FE model in vertical (left) and longitudinal (right) directions.*

Figure 4.6 reveals good agreements between the two models results. In the vertical directions, the results are almost the same while in longitudinal direction, the peak-peak values, approximately, are equal but the mean values of MB-FE model results, in this direction, are not equal 0, this because of the longitudinal static force introduced at the axle-boxes of the fourth wheelset due to the rotation of the car body and the trailing bogie with positive pitch angles due to the flexibility of the fourth wheelset.

In conclusion, it can be stated that despite its simplicity the MB-FE model is capable of reproducing the running dynamics of the vehicle and therefore can be used to generate realistic boundary conditions for the analysis of vibrations resulting in the cracked axle from the simultaneous effect of the crack breathing mechanism and disturbances arising from track irregularity and wheel OOR profile.

4.3 MB-FE model results

The MB-FE model was used to study the influence of crack propagation on the vibration signals measured at the axle-boxes in vertical and horizontal direction. Two crack locations were simulated, the first one close to the wheel (crack at element 7, see Figure 4.1) and the second in the centre of the axle (crack at element 15, see Figure 4.1). Both simulations are carried out for crack sizes varying from 0% (no crack) until 50% in 5% steps.

The same track irregularities used in the first verification level as well as wheel OOR disturbance, with amplitude level equal to the one introduced in Section 3.2.8, are considered in these simulations. The simulated signals were obtained in time domain and by means of FFT function converted to frequency domain to obtain trends with crack sizes of the harmonic components of axle-box acceleration.

Figures 4.7 and 4.8 show the trends with crack sizes of the first three harmonics of the acceleration signals, measured at the left axle-box of the cracked wheelset (node 3, see Figure 4.1), for the first and second crack location respectively, with and without considering wheel OOR irregularities.

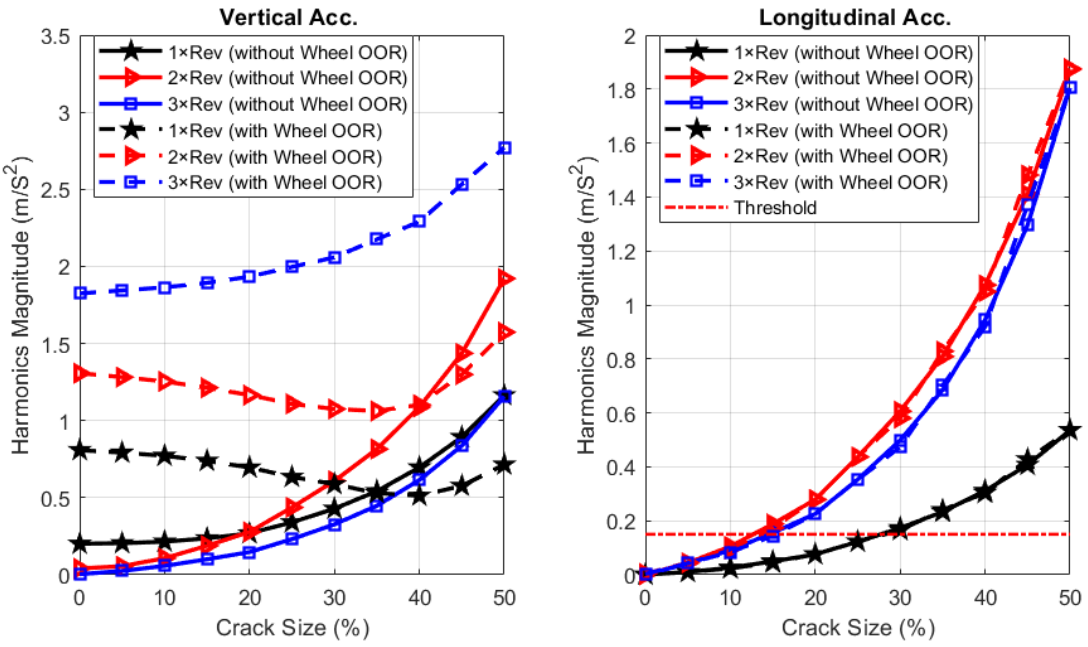

Figure 4.7: *Trends of first three harmonics of acceleration signal for crack at first location (left: vertical axle-box acceleration, right: horizontal axle-box acceleration).*

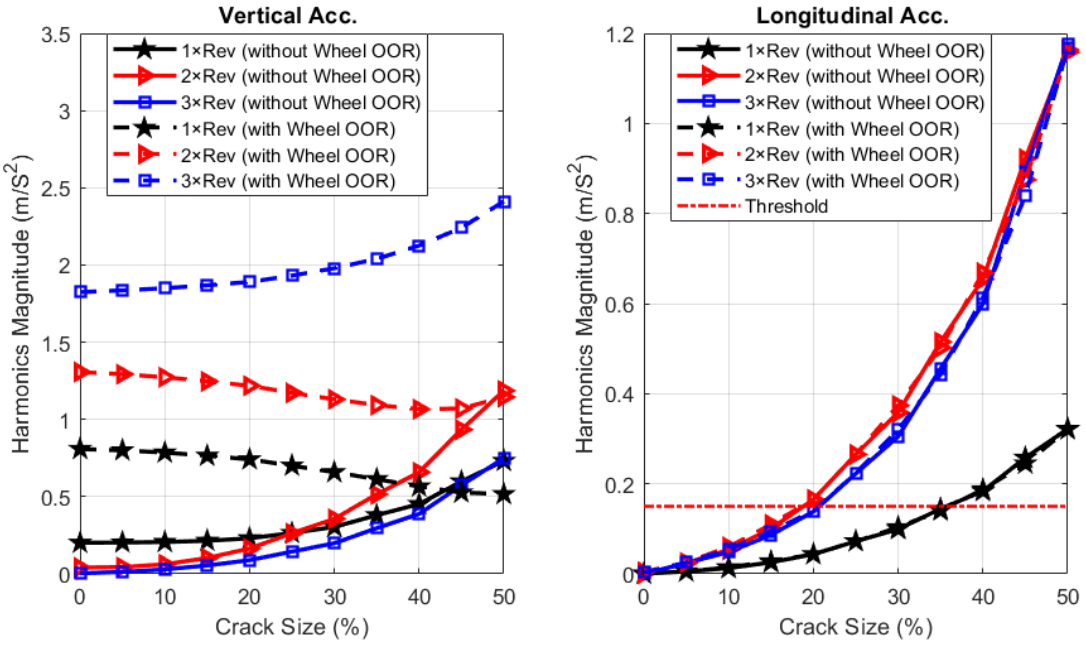

Figure 4.8: *Trends of first three harmonics of acceleration signal for crack at second location (left: vertical axle-box acceleration, right: horizontal axle-box acceleration).*

As far as the harmonics of the vertical acceleration are concerned, the effect of wheel OOR disturbance appears to be dominant for all the harmonics considered especially for crack sizes below 30%, as demonstrated by the comparison between the results obtained with and without considering wheel OOR. For crack sizes greater than 30% the effect of crack breathing becomes visible at least in the 2xRev and 3xRev harmonics, but it is still difficult to separate the two effects, to the point that the trends of these harmonics are not even monotonic with increasing crack size. Indeed, the trends of vertical direction depend on the phase angle between the crack harmonics and its conjunction from wheel OOR, for instance, the third harmonics (3xRev) seems to be in same phase leading to an increasing trend while the first and second harmonics seem to be in phase opposition, so they produce a decreasing trend.

The harmonic components of the horizontal axle-box acceleration are instead weakly affected by wheel OOR disturbance and show clear monotonic trends with increasing size of the crack. To confirm these conclusions, a second set of simulations was performed considering a double amplitude for all wheel OOR harmonics, and the results are shown in Figure 4.9 and 4.10 for the two crack locations.

It is confirmed that the harmonics of the horizontal axle-box acceleration are weakly affected by wheel OOR disturbance and therefore a crack detection criterion based on monitoring these quantities can be robust towards the effect of disturbances arising at wheel-rail contact. On the other hand, the results shown in Figure 4.9 and 4.10 for the vertical axle-box acceleration confirm that this signal is highly affected by wheel OOR profile. Therefore, it can be concluded that the measure of the horizontal component is nearly insensitive to the effect of various sources of disturbance, particularly wheel OOR, compared to vertical one, thus, it provides promising indicator of axle fault development.

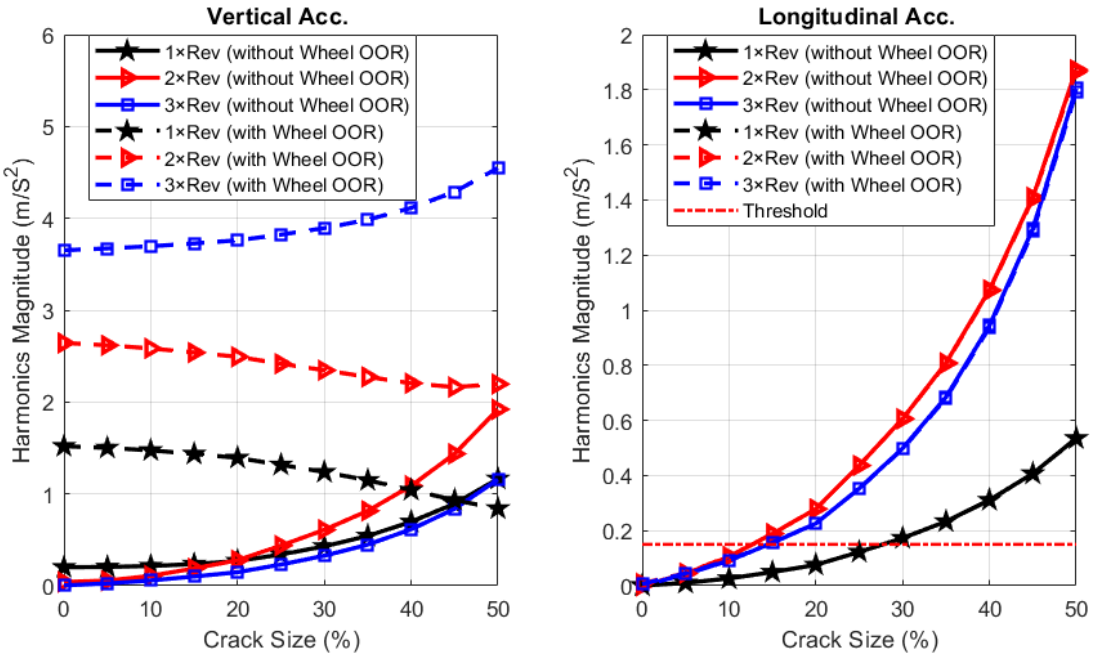

Figure 4.9: *Trends of first three harmonics of acceleration signal for crack at first location with double wheel OOR irregularity amplitude (left: vertical axle-box acceleration, right: horizontal axle-box acceleration).*

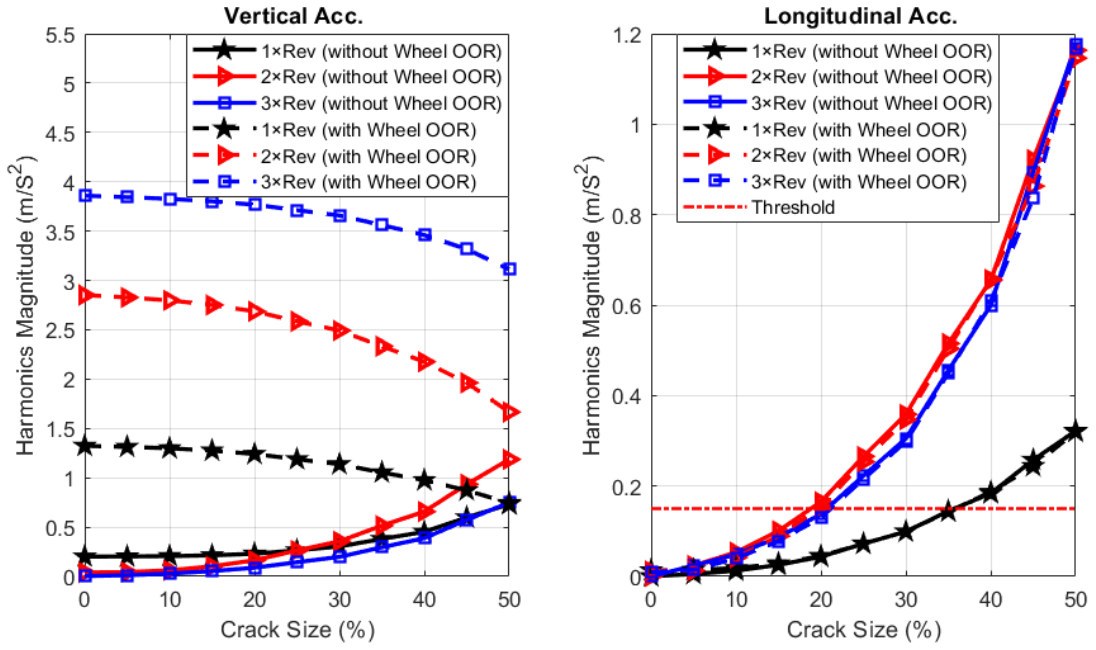

Figure 4.10: *Trends of first three harmonics of acceleration signal for crack at second location with double wheel OOR irregularity amplitude (left: vertical axle-box acceleration, right: horizontal axle-box acceleration).*

4.4 Definition of threshold for defect detection

The last stage of the proposed SHM is defining a threshold criterion of a running axle in order to give the operator an alarm when the faulty axle deterioration exceeds the pre-adjusted threshold. The general procedure of statistical monitoring is to collect a large number of healthy data samples used as the reference data set. All new measured data are then compared to the healthy ones to check whether an abnormal behaviour occurs.

In order to establish a simple crack detection criterion, the horizontal acceleration of the axle-box at zero crack size obtained from MB-FE model simulation presented in Section 4.3 is examined, see Figure 4.11. Despite this quantity is partly related to random excitation from track irregularity which is eliminated once the extraction of the NxRev harmonics of the signal is performed, it can still be considered as a realistic quantification of noise and disturbance affecting the detection of axle crack based on the measure of longitudinal axle-box acceleration. As shown by the Normal Probability Plot, this quantity is reasonably described by a Normal distribution with zero mean. Then the standard deviation σ of the signal can be used to define a threshold for crack detection. From the simulation of zero crack, a standard deviation value σ = 0.0485 m/s^2 is obtained. Assuming a threshold value equal to three times the standard deviation results in a threshold value which is approximately 0.15 m/s^2. This threshold value is superimposed on Figures 4.7 to 4.10 as a horizontal line.

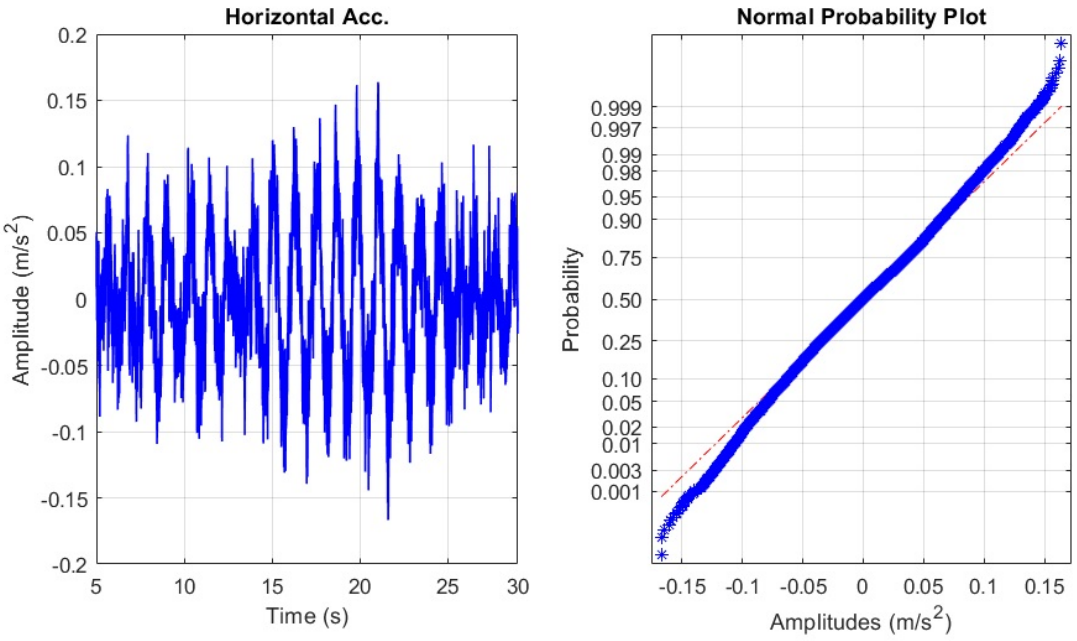

Figure 4.11: *Horizontal acceleration of the axle-box for zero crack size (left: Time history, right: Normal Probability Plot).*

Considering again the magnitude of the 2xRev and 3xRev harmonics of the horizontal axle-box acceleration shown in Figures 4.7 to 4.10, it is observed that values in excess of the threshold are obtained for crack size 15% or greater when the first crack

location (close to the wheel) is considered and for crack size 20% or greater when the crack is at the second location (in the centre of the axle). Although these crack sizes are much greater than those that can be detected by an ultra-sonic (US) non-destructive inspection, it shall be noted that this crack detection criterion can be applied for the continuous structural health monitoring of the axle, whereas US inspections are taken, for freight wagons, at 600,000 km or 6-year distance. It shall also be considered that a crack size in the order of 15-20% is still far enough from the critical size that will produce the failure of the axle to allow to stop the wagon and scrap the axle avoiding service disruptions and, most importantly, in-line failure of the axle which might result in major safety issues.

It is worth to observe that the crack size at which the threshold value of 0.15 m/s^2 is exceeded is approximately the same for both the 2xRev and 3xRev harmonic components, so the crack detection procedure could be made more robust to false alarms by checking that the threshold is exceeded on both these harmonic components.

CHAPTER 5

Data treatment techniques

5.1 Introduction

In previous chapters, it was shown that the examination of super-synchronous vibrations at the axle-boxes can be used to detect the presence of a crack in a railway axle before the size of the crack becomes critical. However, it is not an easy task to implement a structural health monitoring technique for axle integrity based on measuring axle-box vibrations mainly for two reasons:

1. The presence of very large noise affecting the measured signals.

2. The fact that in a real case the rotational speed of the wheelset is not constant in time leading to non-stationary vibration signals.

Different feature extraction techniques like time domain, frequency domain and time-frequency domain can be used to solve these issues and enable the effective SHM of the axle.

In this chapter, after examination of the State-of-the-Art, different techniques are tested to propose an effective technique able to extract the useful information from noisy and non-stationary vibration signals which are representative of signals obtained from railway field. The proposed signal processing technique is applied to crack simulated signal corrupted with random noise to assess the possibility of using this technique to extract the signal harmonics. Moreover, a tacho-less technique suitable for railway continuous SHM applications is proposed and validated.

5.2 State of the Art analysis

5.2.1 SHM using vibration measurements

SHM is an independent tool for measuring the different parameters (e.g. vibration, temperature, etc.) to monitor the condition of the different components of the machine. SHM can be done on-line or off-line. In the long term, SHM provides current information from time to time about the condition of the machine. The SHM consists of three steps: signal measuring, signal processing (e.g. de-noising), and data analysis [68–70].

The main goals of the SHM are:

1. To discover the presence of damage in the machine.
2. To estimate the geometric location of the damage.
3. To estimate the severity level of the damage.
4. To predict the remaining service life of the machine.

Sometimes, the deterioration in machine takes place so fast that there is a very small gap between fault detection and total failure [71], in such cases, continuous or real-time monitoring with automatic data treatment technique is needed to stop the machine at the proper time. Unusual vibrations frequency or magnitude can be used as an indicator for problems in systems having rotating or reciprocating parts, such as bearings, engines, gear boxes, shafts, turbines, and motors. To reduce regular periodic inspections, reliable structural health monitoring is very important and can be performed by measuring the in-service vibration of the system [72].

The vibration signals can be described in terms of three parameters: displacement, velocity and acceleration. The sensitivity of sensors used for measuring these parameters varies with the frequency of the vibration. The general selection guideline is to use displacement sensors to pick up low-frequency signals, velocity sensors in the intermediate frequency ranges and accelerometers for high frequencies [73–84].

The vibration signal properties that have to be measured are usually vibration amplitude, frequency and phase. The vibration measurements are carried out in the time domain which gives only the trend of vibration level (e.g. peak-to-peak, RMS, etc.). In some cases, time domain signal might be used as an indication of the condition of the whole machine (whether the machine is in good or bad condition) but in cause of the vibration level increases at the component level, it is difficult to assign it with such lone measurement of overall vibration. To examine the source of vibration in component level, one needs to study the relationship between the vibration signal frequencies and the rotational speed of the shaft. In fact, every fault in rotating machines has a unique frequency (or frequencies) to participate in the overall vibration signal [85]. In rotating machinery, different faults at the component level might provide vibration frequencies in integer multiples (or divisions) of the rotational frequency of component speeds.

A valuable and intensive literature survey of vibration monitoring methods and signal processing techniques for SHM was introduced in [72, 86, 87]. In addition, many researches were carried out for SHM of a rotating machinery in [88–91].

5.2.2 Vibration signal processing techniques

There are no general signal processing techniques that would be appropriate for all applications and also, it is not practically possible to express all signal processing methods for various applications [92, 93].

As long as this work is concerned with SHM of railway axles, a review of various types of vibration signal processing techniques for a variety of rotating machines is reviewed and presented. These techniques are grouped into three categories: time domain, frequency domain, and the joint time-frequency domain.

Time Domain

Vibration signals (displacement, velocity or acceleration) are measured as a series of digital numbers in the time domain. In some applications, time domain signal is very useful and can be used to describe the statistical properties of the vibration signal (e.g. peak-peak value, RMS, crest factor, enveloping, Probability distribution, density function, etc...). Time Series (TS) models which are developed as an approximate mathematical model based on a set of input-output measurements are the earliest models used in SHM where the time domain analysis of vibration signals was used to diagnose the damages in mechanical structures [94–97].

Frequency domain

Frequency domain as well as time-frequency domain features can generally show rotating machinery faults better than time domain vibration features. In these domains, particular frequency components such as resonance frequency components or defect frequency can be relatively easily detected and matched to faults such as railway axle transversal crack which causes a change of the axle bending vibration harmonics, the topic of this thesis.

By increasing the order of frequency or time-frequency transformation parameters, these techniques were researched to effectively extract coefficients and were used by calculating correlation or logarithmic value of transformation parameters. For instance, after the spectrum had been used widely in both linear and logarithmic presentations, the power spectrum as a second order spectrum was applied successfully [87]. In rotating machinery, spectral analysis of the vibration signals is perhaps the most popularly applied approach and by means of Fast Fourier Transform (FFT), the features of the signals (raw signals or processed signals) can be estimated. The higher order spectrum is also called the bispectrum. The power cepstrum is a logarithm of the power spectrum which was also used to machinery fault diagnosis [87]. Another second order of frequency domain method is "cyclostationarity". Cyclostationarity was used as an effective tool for early diagnosis of faults in gear systems [87].

Fast Fourier transform (FFT)

To estimate the strength of different frequency components (i.e. the power spectrum) of a time-domain signal, the well-known transform, Fourier transform (FT), is used [72]. There are two types of Fourier transform, direct FT used to convert the signal from time domain to frequency domain, and an inverse FT used to convert the signal from frequency domain to time domain. Discrete Fourier transform (DFT) is considered for

a finite time called the "frame" or "time window", which is then digitized and stored for feature extraction. FFT is a special case of DFT with some requirements to make DFT faster. FFT is considered as more effective and efficient diagnosis technique to obtain the Fourier transform of discretized time signals.

To avoid false frequency components that take place due to aliasing, the selection of an appropriate sampling rate is important for signal digitization [72]. As per Nyquist theorem, the sampling frequency should be at least twice the maximum frequency required in the signal spectrum. FFT has been used in several types of structures to detect damage in many applications.

Frequency domain technique is used effectively with stationary signals but in the case of non-stationary signals, this technique is not valid anymore. Time-frequency domain techniques are the suitable techniques for non-stationary signals.

Time-frequency domain

As mentioned before, FFT has some limitations as it's unable to describe the change in time of the signal's frequency content. Therefore, the joint time-frequency analysis technique is used to define a signal simultaneously using two-dimensional representation (time vs. frequency) by comparing them with elementary functions such as the frequency modulated Gaussian functions [98]. The major difference between each time-frequency method is to handle the problem of uncertainty. Here, the uncertainty principle states that "one can't simultaneously have good frequency resolution and good amplitude resolution" [99]. To overcome the time information loss problem of FFT, other signal processing techniques (e.g. short-time Fourier transform (STFT), Wigner-Ville distribution (WVD) and wavelet transform (WT)) are introduced to represent the signal in time-frequency domain.

In the past decade, time-frequency analysis techniques have been studied and applied to machinery fault diagnosis due to their ability to represent signals in both the time and frequency domains. Preliminary time-frequency techniques, windowed Fourier Transform [100] and short time Fourier transform (STFT) [101], were used to monitor the condition of rotating machinery. Wigner distribution [102] and the spectrogram [103] are the most well-known quadratic time-frequency representations belonging to the Cohen class. Continuous wavelet transform (CWT) has been generated based on the STFT with better time-frequency resolution and used to monitor the condition of the rotating machinery. Discrete wavelet packet analysis (DWPA), and discrete wavelet analysis also showed their potential in fault diagnosis [87].

Short-time Fourier transform (STFT)

STFT is an extension of FFT capability of analyzing non-stationary or noisy signals by dividing the time domain signal into small time windows and implementing the Fourier transform for each time segment to represent the change in signal frequency existed in that segment. It gives constant absolute bandwidth analysis to identify harmonic components and offers fixed resolution in two-dimensional description, irrespective of the actual frequency range [104]. The size of the window defines the accuracy of time and frequency resolution. Large window introduces poor time resolution and good frequency resolution and vice versa, therefore, STFT has a weakness of low-resolution

problem. This limitation is resulted choosing a small window, which can't be used with the dynamic transient behavior of the structure. Also, it can't be used to define two closed natural frequencies [105].

Spectrogram is a visual representation of the STFT. The spectrogram is a 2D visual heat map where the horizontal axis represents the time of the signal and the vertical axis represents the frequency axis. The third dimension is the amplitude and is represented by colors. What is visualized is an image, in which, for a specified time point and a specified frequency, darker colors means that lower in magnitude and lighter color represents the higher in magnitude, as shown in the example presented in Figure 5.1. The main drawback of the spectrogram appears in cases with large frequency variation where bad time-frequency resolution is obtained as a result of fixed window length used during whole time history. To overcome this disadvantage, variable window length should be used where wider window applied with low frequencies and narrower window applied with high frequencies.

Chirplet transform (CT) is a time- frequency representation tool, similar to STFT, but it is using a window with adjustable length depending on the rate of change in the signal frequency with the time. CT involves the inner product between the signal and chirp basis functions [106]. CT can be physically interpreted as the projection of the signal on a set of atoms with different chirp rates. When the chirp rate equal zero, the CT degrades into normal spectrogram [106]. From this view, spectrogram can be considered as a special case of CT. In other words, CT could provide a more flexible and effective time- frequency representation than STFT [106]. Even though the spectrogram renders a limited time-frequency resolution, it is motivated by its computationally efficient compared to the Chirplet transform [107]. Figure 5.1 presents an example of spectrogram and Chirplet transform for same vibration signal.

Wavelet transform (WT)

As mentioned before, there is a disadvantage of the STFT, namely that the frequency resolution fixed for all frequencies range as shown in Figure 5.2. For good resolution in time at different frequencies range, different width of the window should be used where the window length is defined depending on the required resolution for different frequencies. Wavelet transform is able to deal with this condition, even though it is mapping the signal into timescale or time-level rather than time-frequency, but there is a connection between scale, level, and frequency. The better resolution at high frequencies in time is achieved by reducing the resolution in frequency and the resolution in time becomes weaker at lower frequencies [108] (see Figure 5.2.

The first idea of Wavelet transformer (WT) was presented by Jean Morlet in 1982. He introduced the idea of accurate time-frequency analysis strategy to obtain an optimal balance between frequency resolution and time resolution for seismic wave analysis. In comparison to STFT where complex cosine and sine functions are used to map the signal from time to frequency domain, WT consists of a group of basic functions (as a function of time) that can be independently dilated and shifted. WT of a signal is calculated using one of two methods, Discrete wavelet transform (DWT) and continuous wavelet transform (CWT). The main difference between the two methods is the scaling, where DWT scaling factor is taken as a power of two and it is generally

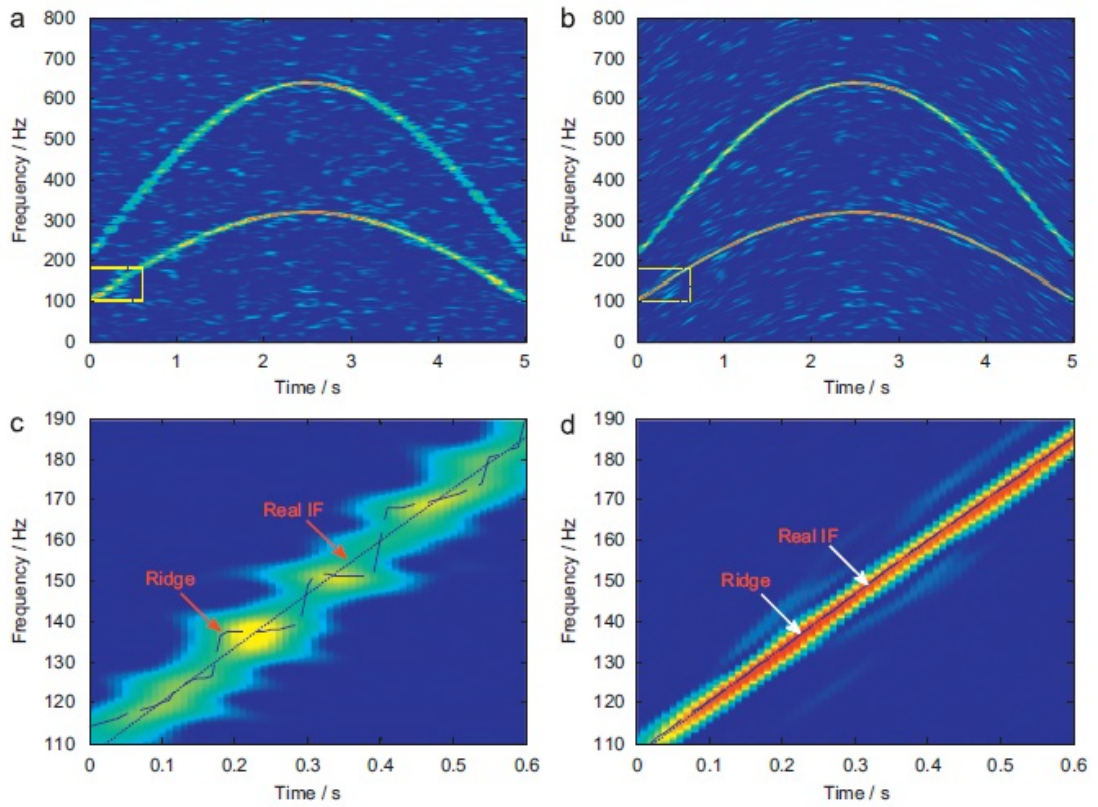

Figure 5.1: *(a) STFT spectrogram; (b) CT spectrogram; (c) zoomed-in spectrogram of (a); (d) zoomed-in spectrogram of (b) [106].*

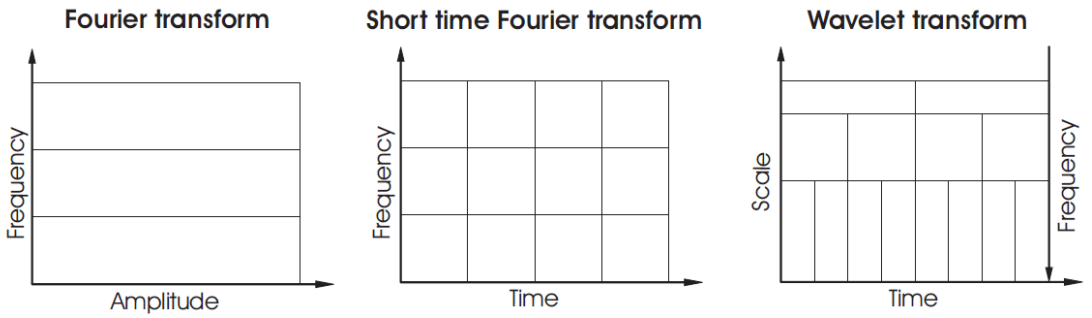

Figure 5.2: *Schematic picture of the Fourier, short time Fourier and wavelet transform resolution.*

performed through a pair of low-pass and high-pass wavelet filters while CWT scaling factor is chosen randomly or by means of convolution [109]. CWT is more sensitive than Wigner-Ville Distribution (WVD) to stiffness change [110].

WT has a great possibility to detect a sudden change in a signal or to locate an abrupt change in response from the acceleration signal. Also, it is robust and insensitive to changing working conditions. WT has been used profusely in many fields such as mechanical engineering, robotics, biomedical engineering, transportation engineering, power engineering, structural vibration control, earthquake, image processing. WT was used also for noise decreasing, data compression and computational efficiency. For denoising purposes, complex harmonic wavelets (typically of one-octave bandwidth)

are especially used with a compact in the frequency domain, but infinite in the time domain [111]. Complex harmonic wavelets are narrower and look like windowed sinusoids (harmonic functions) and because its imaginary part is orthogonal to the real part, complex wavelets have the advantage of non-sensitivity to the phasing of the event being transformed (sine rather than cosine).

Different wavelet transformers were used for SHM [112]. We can summarize that the wavelet transform is a tool that cuts up data, functions or operators into different frequency components, and then studies each component with a resolution matched to its scale by using a variable length window, where:
- Narrower windows are more appropriate at high frequencies.
- Wider windows are more appropriate at low frequencies.

Cohen's class

Cohen's class (CC) distribution is a technique to evaluate the energy of time-varying systems [113]. In 1932, Eugene Wigner introduced the initial Wigner distribution to study the problem of statistical equilibrium in quantum mechanics. After 15 years, Jean Ville modified the Wigner distribution and introduced it, as a first time, in the signal processing to reduce interference between the frequency components. Now, in the field of signal processing, it is commonly known as Wigner-Ville distribution (WVD).

WVD is one of the most common time-frequency analysis techniques and it's one of the so-called 'Cohen's class' of time-frequency distributions. WVD is used to monitor the nonlinear behavior because it breaks the uncertainty principle to give great resolution for accurate examination in both domains. For the fault diagnosis of bearing, WVD was applied based on empirical mode decompositions (EMDs) [114]. The main advantages of WVD are its simplicity, excellent accuracy, effectiveness, no requirement of window function for its analysis, better resolution than STFT, and stable with window effects. On the other hand, WVD has some drawbacks of cross-term interference (i.e. generation of false frequency does not exist in the original signal).

To overcome the WVD cross-term interference problem, Choi- William [115] introduced alternative kernels, but his method has also some drawbacks summarized in the cost of lower resolution and the increase in computational time. Different smoothing techniques were proposed to maintain the optimum resolution by first locating the interference components, and then withdraw from the unsmoothed WVD [116]. A smooth pseudo WVD is used in condition monitoring field in many applications such as to monitor the condition of the gearbox by detecting the broken tooth in a spur gear [117] and to spread the energy of the frequency component by using a Gaussian window [118]. It is also used for comparing the acoustic and vibration signals to detect the faults in gear and to compare the time-frequency characteristic of cracked rotor [110, 119].

Hilbert-Huang transform

The traditional methods, e.g. Fourier integral transform and FFT, have a strong assumption that the signals being processed should be obtained from linear systems and the data must be stationary or periodic. Hilbert-Huang transform (HHT) is an algorithm used for analyzing the data obtained from non-linear and non-stationary signal

by decomposing the signal into "Intrinsic Mode Functions" (IMF) and then obtains "Instantaneous frequency" (IF).

Huang et al. [114] introduced the HHT as a data analysis tool or an adaptive signal processing technique to obtain the properties of stationary, non-stationary and transient signals, especially for time-frequency-energy representations. HHT consist of two steps, firstly, by using empirical mode decomposition (EMD) strategy [114, 120–124], the signal will be decomposed into a collection of band-limited quasi-stationary functions called IMFs. Second step, to determine the local energy of all the instantaneous frequency or to obtain its amplitude and phase angle from the non-linear or non-stationary signals, the Hilbert spectral analysis is applied to each IMF. HHT has been applied for vibration signal processing in various fields such as mechanical engineering, earthquake engineering and biomedical.

HHT has some advantages of nonparticipation of any convolution, less computational time and it's a promising method to extract the features of the non-linear and non-stationary signal [125]. On the other hand, HHT has some drawbacks. Firstly, the EMD produces some IMFs at the low-frequency region may lead to result misunderstanding. Secondly, the monocomponent property of obtained IMF cannot be achieved due to wide frequency range. Thirdly, the EMD cannot be used to separate the signals of low frequency components. Therefore, improvements for HHT technique are needed to overcome these shortcomings. In the improved version, wavelet packet transform (WPT) is used as a preprocessor to separate the analyzed signal into a family of narrow band signals [126].

5.2.3 Vibration signal de-noising techniques

Raw vibration measurements always contain unwanted data which are called noise. Ideally, the vibration signal should be free of any noise or interference that would prevent analysis. Unfortunately, this is never happening in the real world because always there are uncontrollable changes of the vibration in a machine that add noise to the signal. High level of noise in the measuring signal can hide useful information included in the measurements. Data processing would be much easier if we do not have to deal with noise and interference signals. The best method to eliminate vibrations noise is to identify the source of it and, if possible, remove it, therefore, the signal can be acquired with less noise. If the noise source cannot be eliminated, then the raw vibration data has to be treated using data processing techniques to minimize the noise level.

The first step for any data processing techniques is to eliminate the noise or at least to decrease its effect. There are different strategies for signal de-noising and the selection of the suitable strategy depends on some factors such as vibration signal source (e.g. signals from rotating machinery are different from the other signals because of the repeatability of the signals features) and also the signal to noise ratio (SNR). In this section, different vibration signal de-noising techniques appropriate for rotating equipments (e.g. railway axles) are introduced briefly:

Filters

Filtering is the most common signal denoising operation. The first step in data acquisition is analog to digital (A-to-D) signal conversion with filtering. Filtering is now

routinely performed digitally after A-to-D conversion. Different types of filters are commonly used with vibration signals include low-pass, high-pass, band-pass, notch, and tracking filters [127].

Averaging

In rotating machinery, averaging is an effective method for minimizing the effects of noise, for isolating frequencies of interest and for showing specific patterns in the data. The instrument uses a digitized time waveform and performs the mathematical operation to produce the FFT. However, observing only one section of time waveform may exclude some peak caused by a random vibration influence. To minimize this, it is common to look at several sections of the time waveform. Several averaging techniques are available in most vibration analysis software, including: linear, exponential, peak hold, and time synchronous averaging (TSA) [128]. Each type has certain qualities that allow it to better suited for a given application.

Singular value decomposition (SVD)

SVD is a matrix decomposition method that can be used to extract the main components representing the useful information from stationary or non-stationary signal. In essence, the SVD method decomposes any $(m \times n)$ matrix A into three matrices: U, S and V, so that, $[A] = [U][S][V]^T$. Where, U is $(m \times m)$ matrix, S is diagonal and $(m \times n)$ matrix, and contains the singular values of A in descending order, and V is $(n \times n)$ matrix. U is called the left singular vector matrix and V is called the right singular vector matrix.

To use the SVD for noise reduction, all singular values in S matrix below a particular threshold are replaced by zero and then matrix A is reconstructed based on the new S matrix. A lot of researches have been carried out to introduce a suitable method for judging which part of diagonal elements in the matrix S should be regarded as those with small values and replaced by zero. Up to now, no general method to determine the effective singular values has been introduced. SVD has good stability in noise reduction and its principles can be found in more details in [129–135].

5.2.4 Computed order tracking (COT)

The vibration signal collected from machines that are working at a constant rotational speed is mainly formed a spectral component defined at discrete frequencies, which are generally related to the rotating speed of the shaft. The condition monitoring procedure assumes a linear behavior of the machine, and each individual spectral component, or a group of them, is related to a specific dynamic force in the machine. These can be inherent in the operation condition of the machine or can arise due to a fault. In the machines working at variable rotational speeds, its vibration signals will be non-stationary signals and when the conventional FFT analysis is applied to these signals, each spectral component spreads over several adjacent spectral lines, depending on the change of the velocity in the machine. Because of this, it is impossible to analyze the resulting spectrum.

One method for vibration analysis suitable for rotating machinery, working under variable speed conditions, is known as order tracking. This is a frequency analysis method that uses multiples of the running speed "orders" instead of absolute frequencies

(Hz) as the frequency base. Order tracking is useful for machine condition monitoring because it can easily identify speed related vibrations such as shaft defects (e.g. axles cracks and bearing wear) [136].

There are at least two order tracking methods that can be implemented, the traditional hardware method and the software computational method. The traditional hardware method directly samples the vibration signal at constant angle increments using analog instrumentation. The sampling frequency is fixed to track the shaft's rotational speed and the shaft speed is calculated from two consecutive tachometric pulses. Ideally, this velocity could be used to fix the sampling frequency of the following shaft revolution. However, to adjust the antialiasing filter, the fixed sampling frequency is retarded for at least another revolution. Using a sampling frequency that was calculated two revolutions beforehand makes this method prone to error for a rapidly changing shaft speed [136].

Computational or digital methods have been introduced in which the signal is sampling at constant time increment (Δt) and then by using computational technique, it can be resampled to a desired constant angle increment ($\Delta\theta$) based on keyphasor pulses. This method is referred to as computed order tracking because it uses numerical techniques to extract speed-normalised data from the vibration signal that has been obtained through traditional sampling methods. COT procedures and examples of its applications can be found in [49, 136]

5.2.5 Rotating shafts RPM determination

One main requirement to perform the above mentioned COT technique is the keyphasor pulses or the tachometer signal in order to resample the signal from time domain to angle domain. There are two techniques are used to obtain the RPM of the rotating shaft:

1. Direct RPM measurements using sensors (e.g. tachometer).
2. RPM estimation using the vibration signal features (tacho-less techniques).

RPM measurement sensors

Low-cost, high-value sensor options are available for RPM measurement applications. Most of these sensors provide simple, reliable and inexpensive transducers for highly sophisticated signal processing techniques. Sensors used for this purpose are shaft (rotary type) encoders, photoelectric (optical type) sensors and magnetic rotational speed (proximity type) sensors. All of these sensors send RPM data in the form of electrical pulses.

Shaft encoders offer a high resolution of typically 1-5000 pulses per revolution (PPR) and clearly defined, symmetrical pulses. Proximity sensors provide medium (or low) resolution sensing, depending on the number of pulses measured per revolution. Photoelectric sensors usually sense a reflective target on the rotating shaft. Magnetic rotational speed sensors use various magnetic proximity measuring principles to monitor the speeds of machine components till 30,000 rpm.

In principle, RPM sensors convert mechanical motion into electric pulses with or without direct contact when positioned near a turning rotor, gear, shaft or other regularly moving device. The resultant output signals are then fed to a digital counter, tachometer, or other monitoring and control device.

RPM estimation using tacho-less techniques

In some applications, it's not possible to add a tachometer hardware due to its complexity or shortage of power. Therefore, to overcome this weakness point, some tacho-less order tracking methods have been introduced in the last few years. Tacholess order tracking approaches, which use the vibration signals to obtain the instantaneous angular speed information, are therefore actively investigated by the engineering community to deal with the limitations of using tachometer.

In reference [137], the acceleration signal was used to perform tacholess order tracking in slightly varying rotational speed applications using a narrow-band demodulation on one of the gear mesh frequencies. A clustering procedure was used by [138], to track an instantaneous frequency (IF) component in the spectrogram of the vibration signal. The IF estimated is low-pass filtered, since it contains noise due to the limited resolution provided by the spectrogram. The filtered instantaneous frequency is used to resample the signal for fault detection.

Papers [106, 139] proposed tacholess order tracking procedures used in case of large speed variation conditions. Reference [139] proposed performing maxima tracking on the spectrogram of the vibration signal where the rough estimation of the instantaneous frequency, obtained from the maxima tracking process, is used to order track the signal and filter out all components except the single of the instantaneous frequency. This mono-component signal is reverse resampled to the time domain.

Paper [106] used the chirplet transform to extract an instantaneous frequency component and then the angular velocity Vold-Kalman filter is applied to the signal to obtain a mono-component signal. Hilbert transform is used on the mono-component signal in [106, 139] to extract the instantaneous phase of the signal over time. This instantaneous phase provides a mapping from the time to the angle domain, which is used to order track the vibration signal.

Similar to the methods proposed in [106, 139], paper [107] improved the maxima tracking algorithm by incorporating acceleration information into the maxima tracking process which renders it more robust in the presence of angular acceleration and noise components. The ensemble empirical mode decomposition (EEMD) algorithm was used by [140] to obtain the mono-component intrinsic mode functions of the signal, which are subsequently used to obtain the phase information of the shaft of interest. Using the discrete spectrum correction technique was proposed in [141] to track the orders of vibration signal obtained from a wind turbine.

Reference [142] proposed a multi-order approach for instantaneous angular speed estimation. The spectrogram is applied to the vibration signal, after which a whitening procedure is applied to attenuate structural resonances. The probability density function (PDF) within an expected operating frequency range is estimated at each time step using multi order information, whereafter the PDF is smoothed to calculate the instantaneous angular speed.

5.3 Proposed signal processing technique suitable for vibration signal of cracked axle

As introduced before, it is not an easy task to implement a SHM technique for railway axle integrity based on measuring its axle-boxes vibrations because mainly of two reasons. Firstly, the high level of disturbance generated by track irregularity which introduces very large noise affecting the measured signals. Generally, the level of vertical axle-box acceleration caused by track irregularity can be in the range of 500 m/s^2 whereas the amplitude of the acceleration caused by the crack is in the order of magnitude of 1 m/s^2. Secondly, the fact that in a real case, the rotational speed of the wheelset is not constant in time, therefore, the signals related to the rotational speed of the axle, e.g. its crack signal, it will be non-stationary signals and more processing has to be performed to treat non-stationary signals as previously mentioned in the State of the Art.

The following signal processing technique, shown schematically in Figure 5.3, is proposed to treat the cracked railway axle vibration signal. This technique is a combination of diverse techniques from the State of the Art and it is able to extract the useful information from noisy and non-stationary signals which is the same conditions of signals acquired from railway filed.

The proposed technique starts with acquiring vibration and tachometer signals then the vibration signal has to be passed through band-pass filter. After filtering, the time domain vibration signal is resampled at constant angular increments of the axle using the tachometer signal, therefore, the non-stationary signal in time domain is converted to a stationary signal in the angle domain. Afterward, the new signal has to be averaged to reduce the effect of random noise. To improve the signal to noise ratio (SNR), the Singular Value Decomposition (SVD) technique is applied to the averaged signal. Finally, the signal spectrum in order domain is obtained by means of FFT.

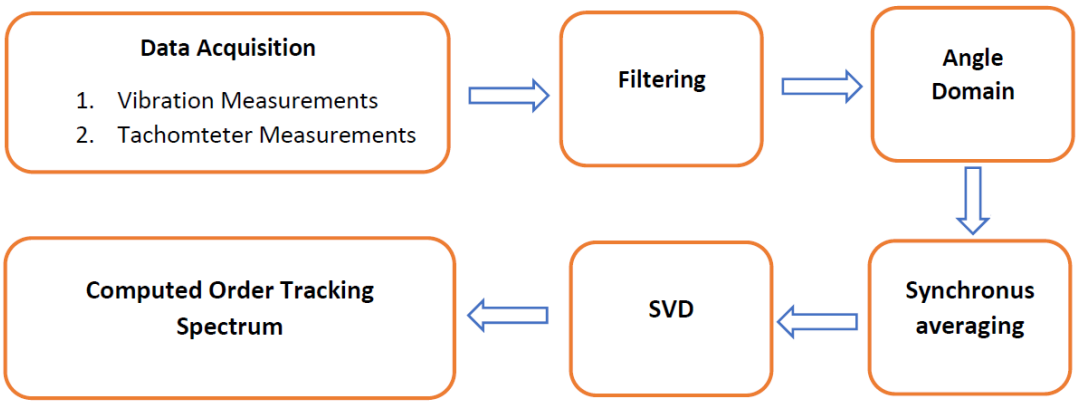

Figure 5.3: *Scheme of the proposed signal processing technique.*

5.3.1 Example of non-stationary crack signal

An example of non-stationary crack signal is shown in Figure 5.4. The signal was obtained from a numerical simulation of an axle with 50% crack size running at variable angular speed according to the time history of the RPM curve shown in Figure 5.5. In fact, the RPM curve is adapted with this large variation to produce a signal with high non-stationarity in which, afterward, is treated using the proposed signal processing technique as an example of the technique application. The wheel OOR disturbance is considered in this simulation.

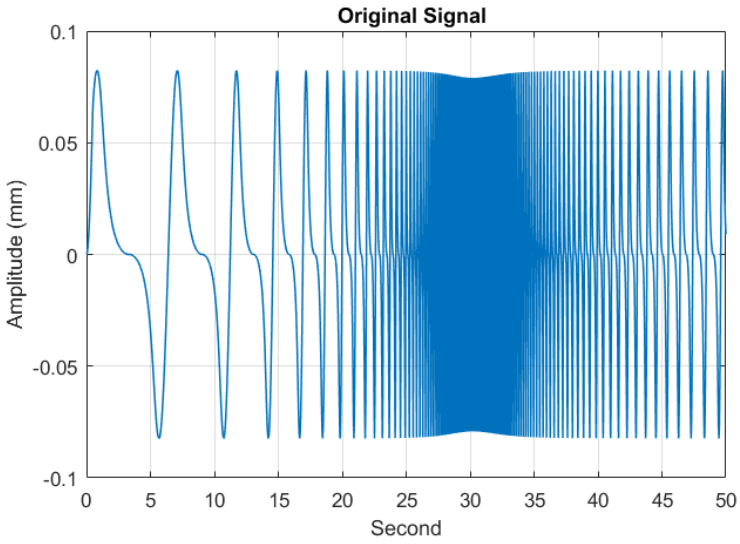

Figure 5.4: *Horizontal vibration signal of cracked axle with variable speed obtained from beam FE model introduced in Section 3.3.*

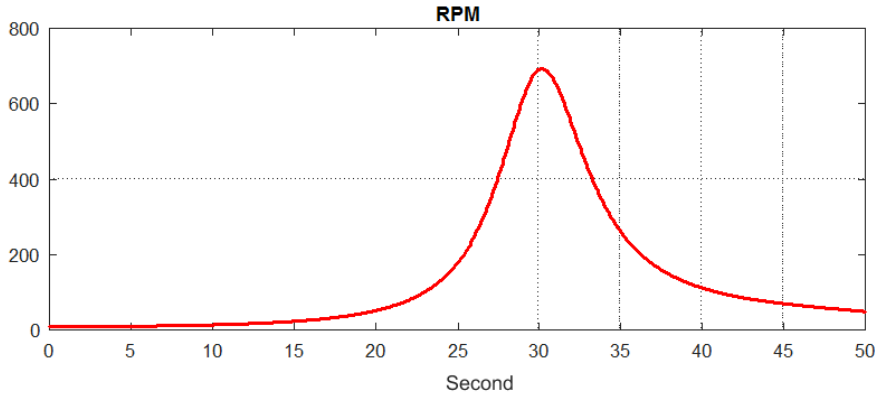

Figure 5.5: *Example of variable RPM.*

Figure 5.6 presents a comparison between the signal spectrum in time domain and angle domain to show the effect of signal non-stationarity on its spectrum and to clarify the benefits of using the COT technique. Figure 5.6 shows that the spectrum of the signal in time domain is corrupted and the signal harmonics cannot be identified, on the other hand, the spectrum of the same signal in angle domain after applying COT technique is very clear and the harmonics order can be identified easily.

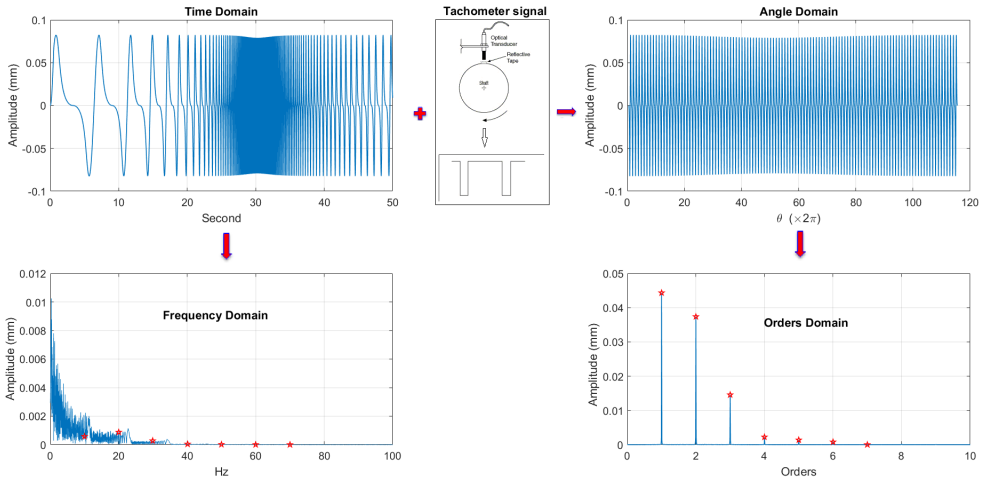

Figure 5.6: *Comparison between two spectra of a signal in time and angle domain.*

5.3.2 Example of application of the proposed signal processing technique

In order to test the validity of using the proposed signal processing technique, an example of noisy and non-stationary vibration signal has been processed using this technique. This faulty signal has been created by adding two different signals, as shown in Figure 5.7. The first signal is the aforementioned non-stationary crack signal shown in Figure 5.4. The second signal is a random noise with standard deviation of 10 times the standard deviation of the crack signal. In fact, the faulty signal has been created by this way due to the lack of having actual non-stationary crack signal measured from a real environment.

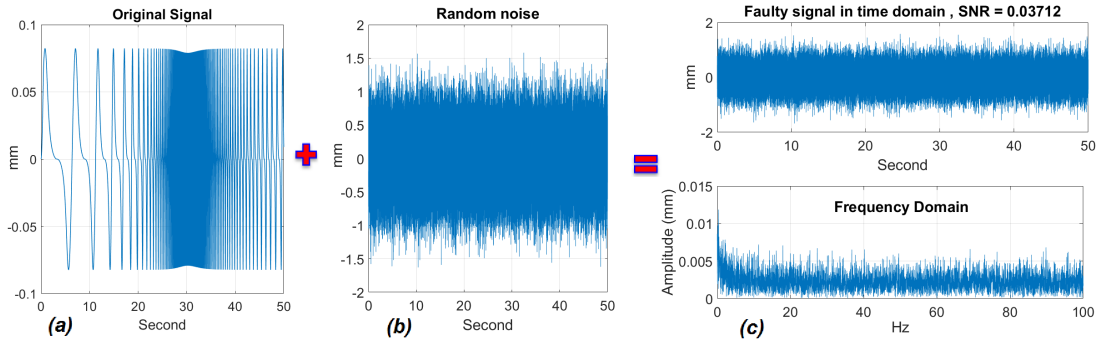

Figure 5.7: *Faulty crack signal construction: (a) non-stationary crack signal without noise; (b) random noise; (c) the total signal and its spectrum.*

The treatment processes of this faulty signal using the proposed signal processing approach is presented in Figure 5.8. It's worth to note the substantial improvement of the SNR in the various phases of the process also the "clean" spectrum obtained at the end of the process. Moreover, Figure 5.8 shows that SVD approach improves the SNR of the angle domain signal but does not add much improvement to the signal order spectrum in terms of the orders peak values.

Figure 5.8 reveals that the proposed signal processing technique can be used to extract the useful information from a non-stationary signal corrupted with random noise.

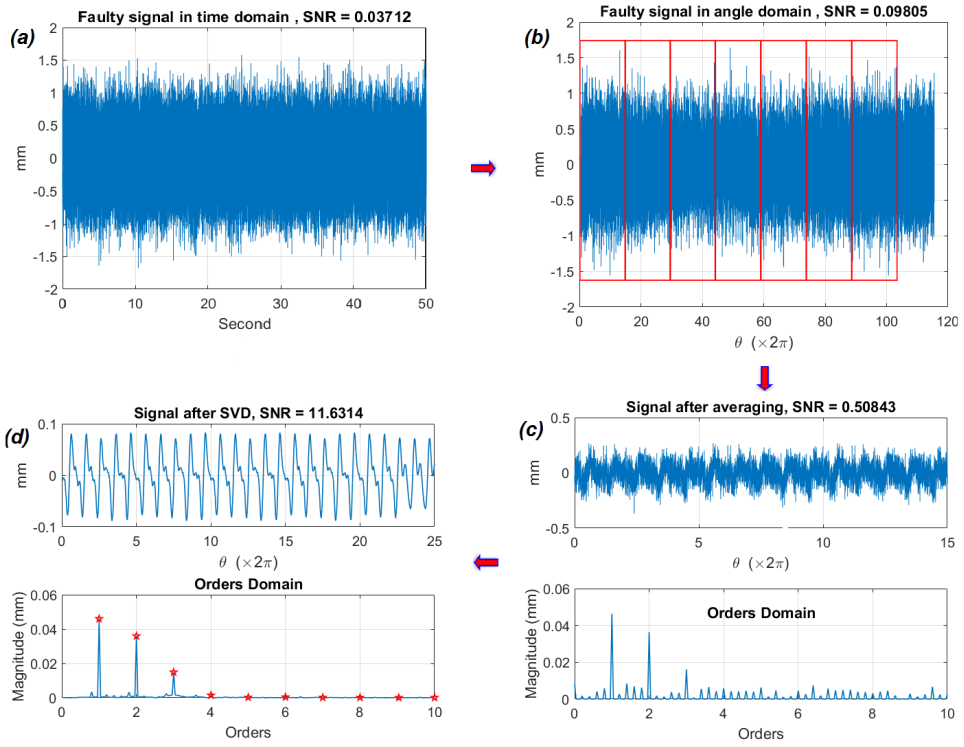

Figure 5.8: *Example of using the proposed signal processing technique: (a) the faulty crack signal in time domain; (b) the signal in angle domain after resampling using tacho-signal; (c) the angle domain signal and its spectrum after averaging; (d) the angle domain signal and its spectrum after averaging and applying SVD.*

5.4 Proposed tacho-less order tracking technique suitable for railway vehicle continuous structural health monitoring application

The proposed signal processing technique introduced in Section 5.3 requires a tacho-signal in order to perform the COT technique but in some railway vehicles, it's not possible to add a tachometer hardware. Therefore, a suitable tacho-less technique is needed to overcome this drawback. Several approaches of tacho-less techniques are mentioned in the literature survey introduced in Section 5.2.5. The main drawback of these techniques is the lack of the automatization which means that they are working off-line, therefore, cannot be used in continuous SHM. Furthermore, the performance of these traditional techniques depends on the level of speed variation and on the SNR.

To overcome the disadvantages of these techniques, a new approach suitable for continuous SHM of railway applications is proposed in this work. In this approach, a coarse angular speed of the axle calculated using the train speed is used to modify the performance of the traditional tacho-less techniques, as shown in Figure 5.9.

In this technique, the train speed is estimated from two axle-boxes vibration signals collected from the vertical direction. The sequential properties of these signals are used to estimate the delay time of one signal with respect to the other one by means of cross-correlation function applied within a rectangular window moving simultaneously through over the two signals. The suitable length of the window and its overlapping percentage have to be selected based on the sampling frequency of the signals. Instan-

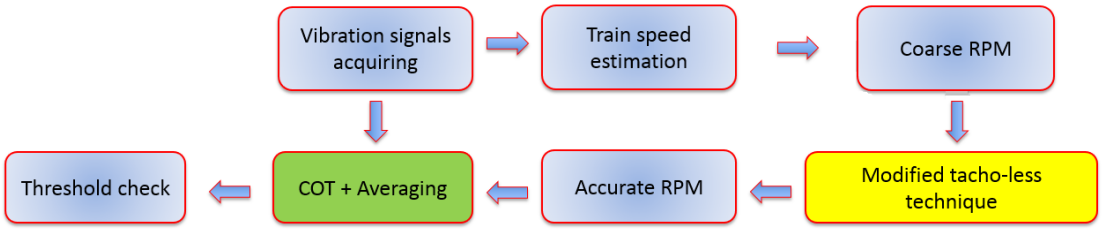

Figure 5.9: *Scheme of complete signal processing technique including the proposed tacho-less technique.*

taneous train speed can be estimate at each window using the horizontal distance (in traveling direction) between the two sensors and the calculated delay time. Because only one value of the delay time is calculated in each window, the instantaneous train speed is considered constant within each window. Therefore, the final curve of the speed is not smooth enough and smoothing process is applied to obtain a continuous smooth curve.

By using the estimated train speed, V, and the wheel radius, R_w, coarse angular speed of the axle can be estimated. This coarse angular speed is set as a reference during extracting the accurate angular speed from the studying signal spectrogram using maxima tracking strategy of one harmonic line, as introduced in Section 5.4.1. This modification improves the effectiveness and robustness of the traditional maxima tracking strategy to operate automatically and, therefore, to be suitable for the continuous SHM of railway applications. Thereafter, the signal processing technique, introduced in Section 5.3, is applied using this accurate (fine) angular speed.

A brief description of the proposed tacho-less order tracking technique steps is listed as follow:

1. Acquiring the acceleration signals from axle-boxes.
2. Filtering the signals using a band-pass filter.
3. Applying the cross-correlation function to the filtered vertical acceleration signals to estimate the delay time between the two signals.
4. Estimation of train speed using the estimated delay time calculated in step 3.
5. Calculation of the axle coarse angular speed (coarse instantaneous frequency (coarse IF)) using the estimated train speed.
6. Calculation of the spectrogram of the filtered acceleration signal to be inspected.
7. Extracting the accurate angular speed using the signal spectrogram and the coarse angular speed calculated in step 5.
8. Applying the proposed signal processing technique, introduced in Section 5.3, using the estimated angular speed, obtained in step 7, to the signal to be inspected. As previously reported in Section 5.3.2, SVD technique does not add much improvement to the signal order spectrum but it enhances the SNR of the angle domain signal and since the signal order spectrum is the main focus of this work, therefore, SVD technique is not considered here to save the computation time.

The technique is illustrated using two examples, as reported in Section 5.4.1. To this aim, acceleration signals measured in a line test are used. Due to the lack of having actual faulty signals, the simulated signal obtained from the beam FE model of cracked axle, introduced in Section 3.3, has been added to one of the measured acceleration signals to construct a signal represents the faulty axle real signal.

Unfortunately, the RPM could not be measured during these line tests and instead the train speed was measured. Therefore, this measured train speed has been used in the proposed tacho-less technique to extract the axle RPM from its measured acceleration signals. Only in this case, the spectrograms of the measured acceleration signals were inspected visually to select an obvious harmonic line to track its maxima values. In addition, the measured train speed was used in step 5 instead of the estimated one to extract the axle angular speed obtained in step 7. Afterward, the extracted RPM was used to simulate the beam FE model of cracked axle. This extracted RPM is considered as the one obtained from a tachometer signal, therefore, it is set as a reference for the other estimated angular speeds, i.e. reference for the coarse and accurate angular speed, obtained from the proposed tacho-less technique depending on the estimated train speed.

5.4.1 Examples of application of the proposed tacho-less technique using faulty signals constructed by adding simulated crack signals to measured acceleration signals

Measurements obtained from two line tests performed on vehicles running at different speed variations are used in this section. The measurements were obtained from the axle-boxes of non-cracked axles. Since these tests were performed on in-service vehicles, wheel OOR disturbances are included in the measurements. Moreover, the spectrograms of the vertical measurements revealed a low level of wheel OOR disturbances where some harmonic lines appeared at low frequencies. Faulty axle signals, constructed as mentioned in Section 5.4, are processed using the tacho-based method and the proposed tacho-less method.

First example

In this example, the proposed tacho-less technique, is validated using line test measurements acquired from the vertical direction of the vehicle axle-boxes. Unfortunately, the horizontal signals could not be measured in this test, therefore, only vertical faulty signal is constructed and processed. The faulty signal is constructed by adding one of the measured acceleration signals shown in Figure 5.10 to the simulated crack signal shown in Figure 5.11. The proposed tacho-less technique steps are explained in more details in this example as follow:

- *Step 1: Acquiring the vibration signals.*

  The effective condition monitoring technique based on vibration measurements, firstly, begins with acquiring the time-varying signal from vibration transducers, such as the accelerometers. The acceleration signals of the railway axle-boxes have to be acquired simultaneously. In this example, two vertical acceleration signals, shown in Figure 5.10, were collected from two axle-boxes of the train, one from leading bogie and the other from trailing bogie of the same vehicle.

These vertical signals have to be acquired from the same side of the vehicle to be subjected to the same track disturbance.

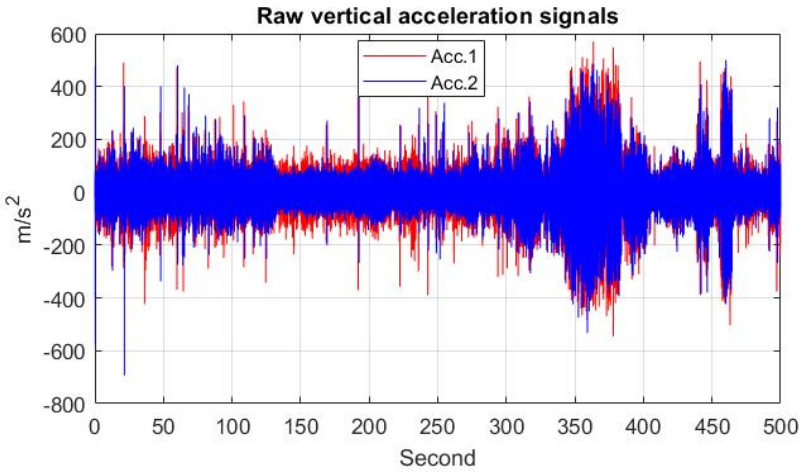

Figure 5.10: *Two axle-boxes vertical acceleration signals obtained from a line test.*

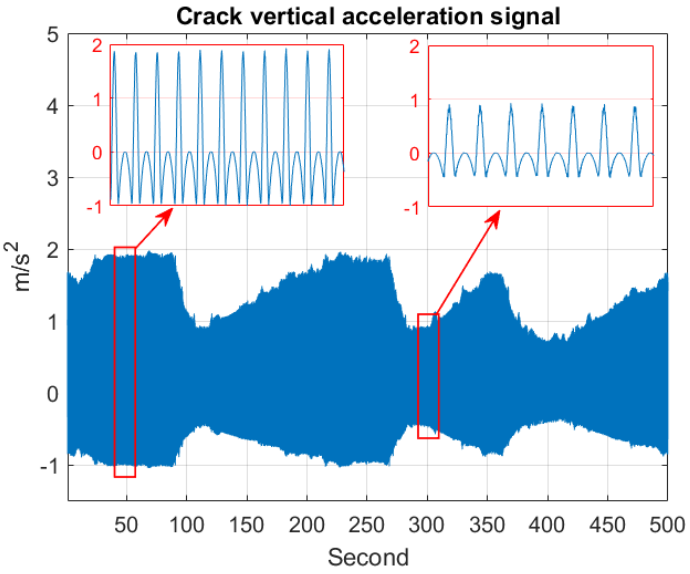

Figure 5.11: *Simulated vertical acceleration signal of axle with 35% crack.*

- *Step 2: Filtering the signals.*

  In this step, the two vertical acceleration signals are filtered using band-pass filter. The simulations results revealed that the filtered signals give more accurate estimation for the train speed than the raw signals. Figure 5.12 shows the vertical acceleration signals after filtering.

- *Step 3: Applying the cross-correlation function.*

  The two filtered signals are divided simultaneously using a rectangular window with 80% overlapping and the cross-correlation function is applied in each window to estimate the delay time between the two signals.

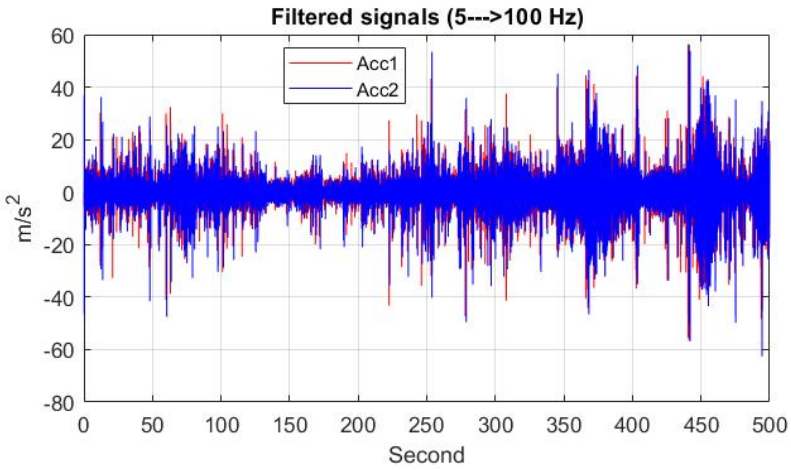

Figure 5.12: *The axle-boxes vertical acceleration signals after filtering.*

- *Step 4: Train speed estimation.*

  The estimated delay time, calculated in *step 3*, is inversely proportional with the train speed and by knowing the longitudinal distance between the two accelerometers (L), the train speed can be calculated at each window using this formula; $V = \frac{L}{delay\,time}$. Because only one value of the delay time is estimated from each window and the train speed is assumed constant within each window, the final train speed curve changes sharply from each window to the adjacent one. Therefore, a smoothing process is used to reduce the sudden changes of the speed curve in which the data points of the curve are modified, where, the individual points that are higher than the immediately adjacent points are reduced, and points that are lower than the adjacent points are increased. This naturally leads to a smoother curve and a slower step response of the curve changes. The measured, estimated (calculated directly from each window) and smoothed train speed are shown in Figure 5.13.

- *Step 5: Coarse angular speed calculation.*

  By assuming constant effective wheel radius and without considering wheel-rail creepage, coarse angular speed of the axle can be calculated using the estimated train speed as; $coarse\,angular\,speed = \frac{V}{R_w}$ (rad/s).

- *Step 6: Time- frequency representation (TFR) of the filtered vertical acceleration signal.*

  There are several algorithms available for tacho-less techniques. Among them, IF estimation based on time-frequency representation (TFR) tool is used mostly in practice. The time and frequency domain information in the vibration signal are investigated simultaneously in a time-frequency distribution so that the IF of interest can be estimated at each time step. Reference [139] used the spectrogram for maxima tracking whilst [106] used the spectrogram to estimate the chirp rate so that the chirplet transform could be used to estimate the component of concerned IF.

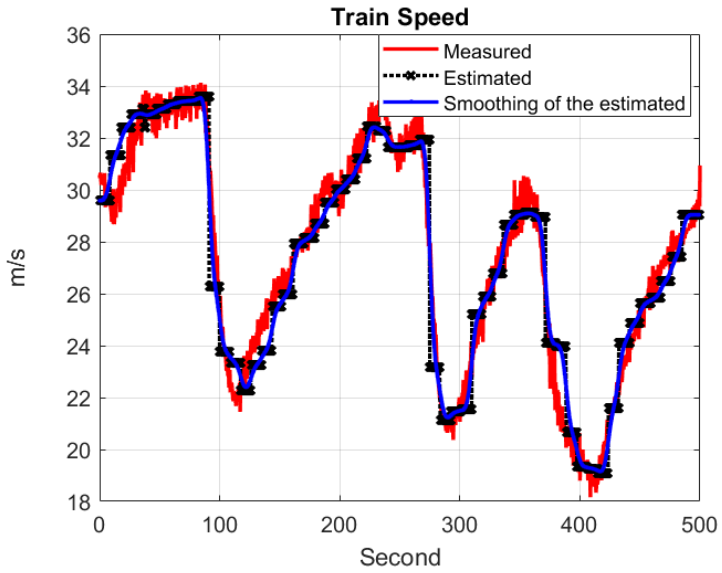

Figure 5.13: *Measured, estimated and smoothed train speed.*

Even though the spectrogram renders a limited time-frequency resolution, it is used for maxima tracking in this work. This choice is motivated by the computational efficiency of this method compared to the chirplet transform. Figure 5.14 shows the spectrogram, using Hanning window and 80% overlapping, of the concerned faulty acceleration signal after filtering using band-pass filter. From Figure 5.14, the harmonics line can easily be noted related to the axle angular speed.

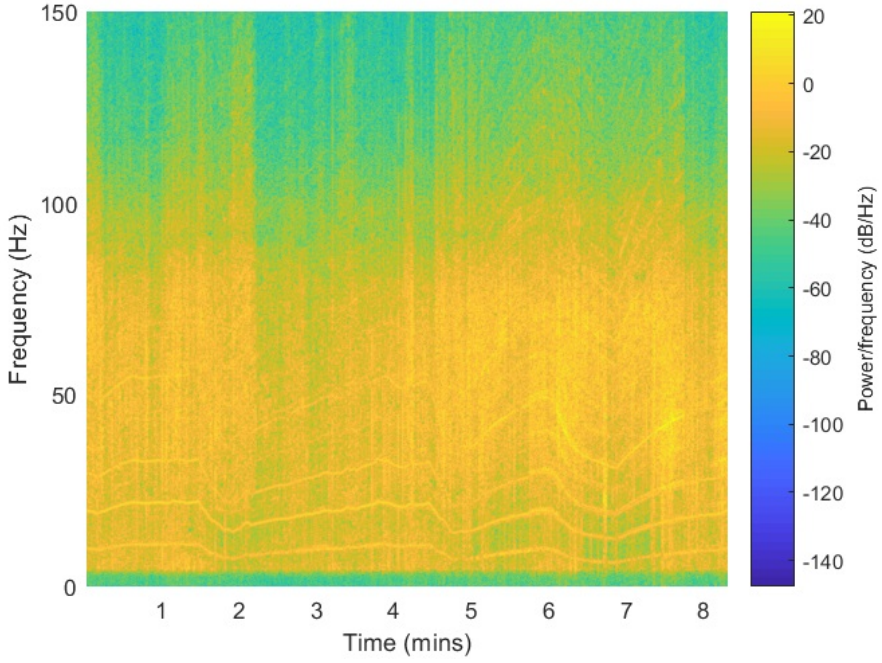

Figure 5.14: *The spectrogram of the faulty acceleration signal.*

- *Step 7: Estimation of the axle accurate angular speed using maxima tracking algorithm.*

  In this step, maxima tracking algorithm [106, 139] is adapted to obtain the axle accurate angular speed. This algorithm depends on tracking the maxima values of one harmonic line, the Instantaneous Frequency (IF), of the signal TFR tool (e.g. the spectrogram). This IF is related to the rotating frequency or angular speed of the shaft, with time-invariant factor N which is the number of the concerned harmonic. The traditional tacho-less techniques [106, 139] based on maxima tracking strategies inspect the TFR of the signal off-line to detect the initial maximum value of the IF. Therefore, there is a limitation on using these techniques in the on-line condition monitoring.

  In this work, the coarse angular speed, obtained in $step\,5$, is converted to frequency (Hz) and then multiplied by N to obtain $coarse\,IF$ which is used as a reference to track the maxima values of the concerned IF. Due to the signal noise or unpredictable changes of operating conditions, traditional maxima tracking methods can lose the track of the IF but in this proposed approach, the maxima tracking algorithm is bound to a specified bandwidth (Δf) with respect to the $coarse\,IF$, as shown in Figure 5.15. The extracted IF results in a discrete curve depending on the spectrogram window length and it's not smooth enough. Therefore, this IF is smoothed to obtain a continuous smooth curve.

  Figure 5.15 presents the $coarse\,IF$ line (black solid line), the bandwidth lines (black dotted lines) and the extracted IF (red solid line) for $N = 2$, all superimposed on the signal spectrogram.

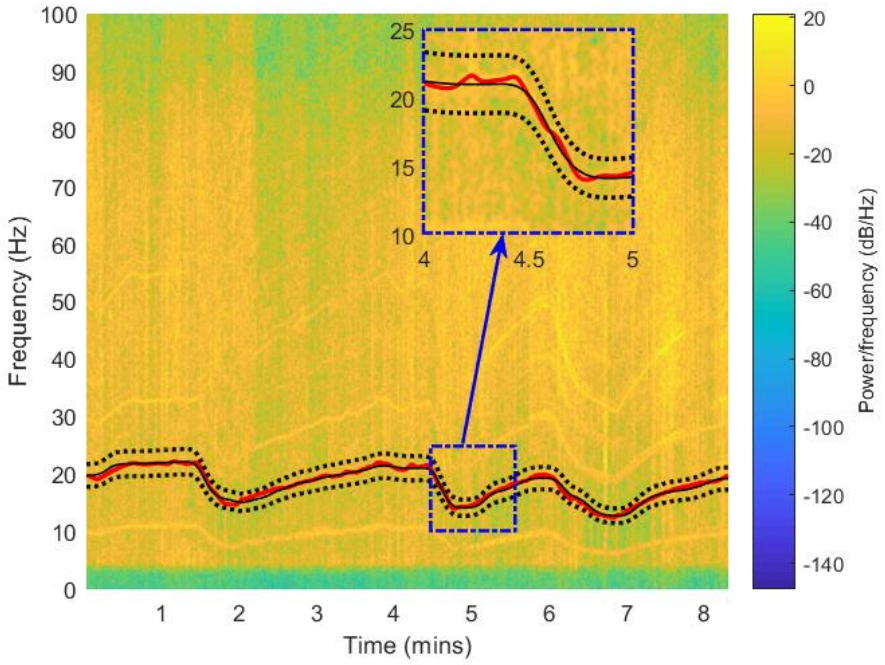

Figure 5.15: *Coarse IF (solid black line), band width based on coarse If (dotted lines) and fine IF (solid red line) superimposed on the signal spectrogram.*

Figure 5.16 shows the axle RPM obtained using the tacho-based method (the same RPM used to simulate the FE model), the axle coarse RPM (obtained from the estimated train speed as in $step\,5$) and the axle fine RPM (obtained from maxima tracking algorithm). The comparison shows that the axle estimated angular speed (fine RPM) is in good agreement with the one obtained using the tacho-based method.

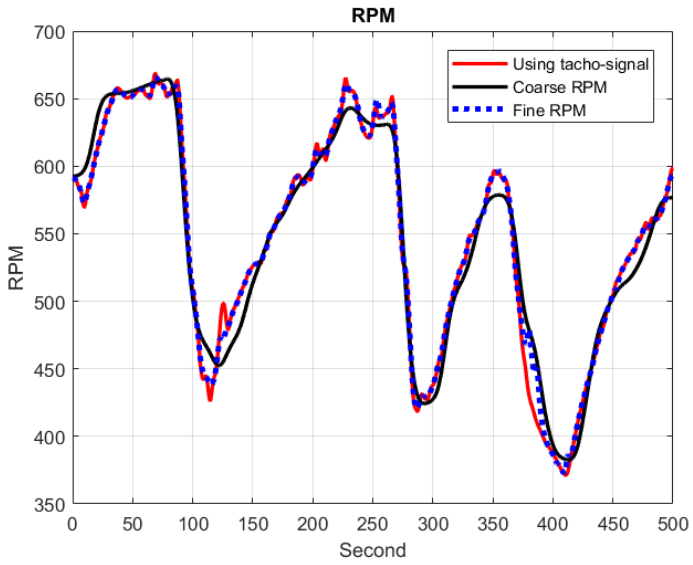

Figure 5.16: *The axle RPMs using tacho-based method, coarse IF and fine IF.*

- *Step 8: Applying the proposed signal processing technique.*

  After extracting the fine IF component, [106, 107, 139] used the angular-velocity Vold-Kalman filter to obtain a mono-component signal related to the fine IF then the Hilbert transform was applied to this mono-component signal to extract the instantaneous phase of the signal over the time. The instantaneous phase provides a mapping from the time to the angle domain, which is used in vibration signal order tracking.

  In this work, the COT technique mentioned in Section 5.2.4 is applied using the estimated angular speed obtained in $step\,7$. The main reason behind using the COT technique rather than using the instantaneous phase is because the effectiveness and the robustness of the instantaneous phase method is directly affected by the IF estimation error, the SNR and the bandwidth of Vold-Kalman filter.

  Figure 5.17 shows the average order spectra of the angle domain signals calculated using the tacho-based method (where the RPM used to simulate the FE model is considered as a tacho-signal) and the proposed tacho-less technique for a faulty signal with 35% crack.

  A good agreement between the two techniques is observed in terms of the waveform of angle domain signals and also in terms of the order spectra, although slight deviations are observed at orders peaks. This small deviation appears because of using the spectrogram which has limited time-frequency resolution due to its fixed

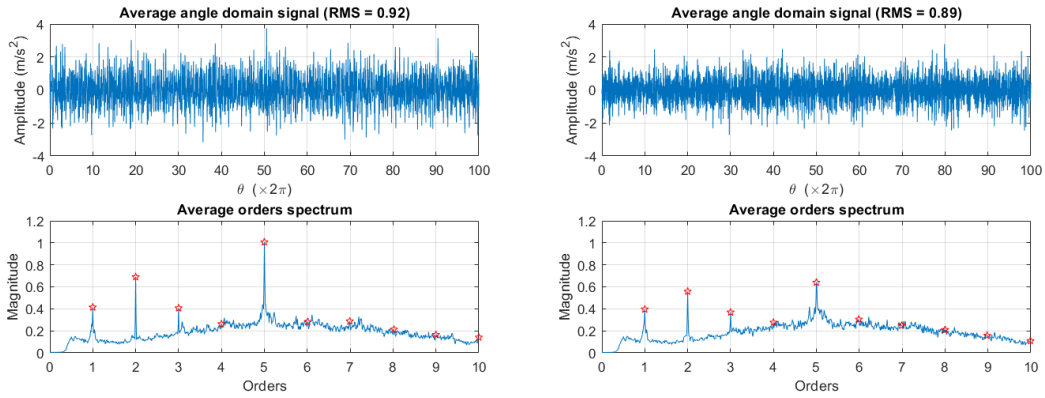

Figure 5.17: *The average order spectra of the angle domain signals (with 35% crack) (left: using tacho-based method, right: using proposed tacho-less method).*

window length. To overcome this drawback, a variable window length should be used where wider window applied with low frequencies and narrower window applied with high frequencies, as introduced in section 5.2.2. Chirplet transform (CT) could provide a more flexible and effective time- frequency representation tool than the spectrogram [106, 107]. The choice of using the spectrogram is motivated because of its computational efficiency compared to the CT.

In order to further extend the comparison, faulty signals constructed from different crack sizes (from non-cracked axle (0%) until 50% cross-section area cracked with 5% step) are processed. Figure 5.18 compares the trend with crack size of the magnitude of the 1xRev, 2xRev and 3xRev harmonics for the processed signals using the tacho-based and the proposed tacho-less techniques.

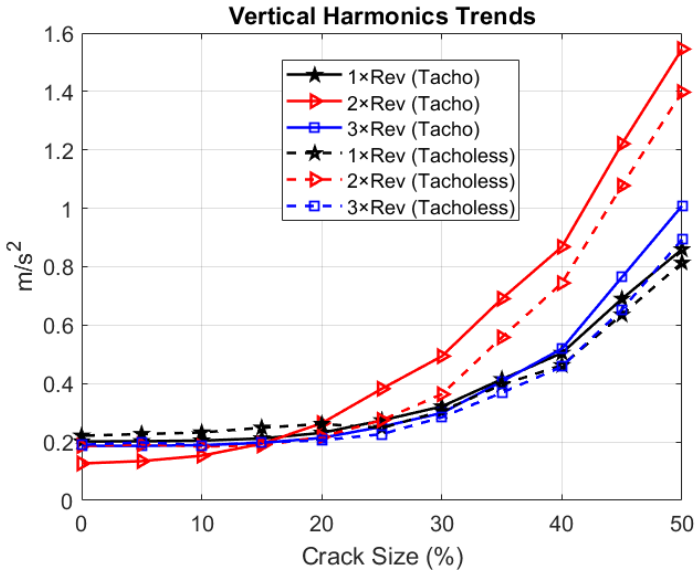

Figure 5.18: *Trends of first three harmonics of faulty signals after processed using the tacho-based method and the proposed tacho-less method.*

In figure 5.18 a satisfactory agreement between the two techniques results can be observed. A small deviation between the two techniques results can be noted due to the use of the spectrogram with fixed window length, as mentioned before.

As far as the harmonics of the vertical acceleration are concerned in Figure 5.18, the effect of wheel OOR appears to be dominant for all the harmonics considered especially with small crack sizes. This is because of the signal caused by wheel OOR disturbance which is periodic with the wheel turn, hence providing the same NxRev components caused by crack breathing mechanism, so that this disturbance cannot be separated by the use of synchronous averaging.

Second example

Same procedures have been applied to another set of measured vertical and horizontal acceleration signals, shown in Figure 5.19, acquired from axle-boxes of a vehicle during another line test. Figure 5.20 shows the train speed measured during this test as well as the estimated speed obtained as previously explained in the first example.

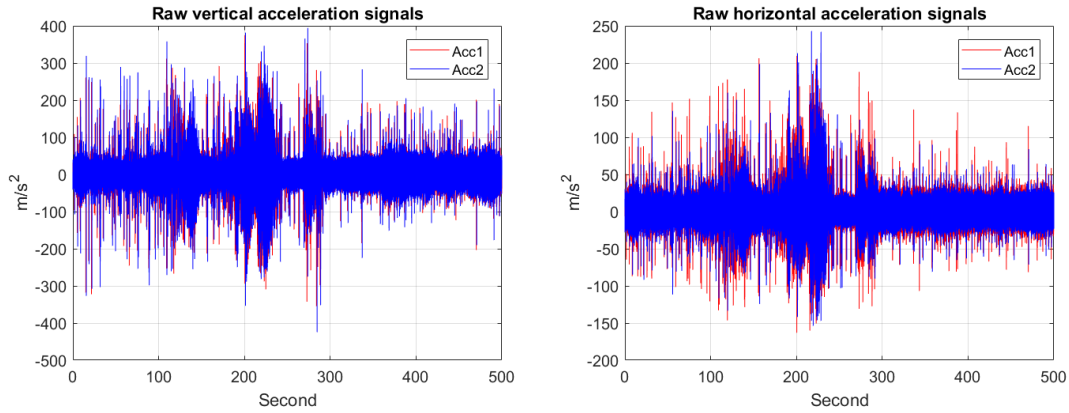

Figure 5.19: *Two axle-boxes acceleration signals obtained from a line test.*

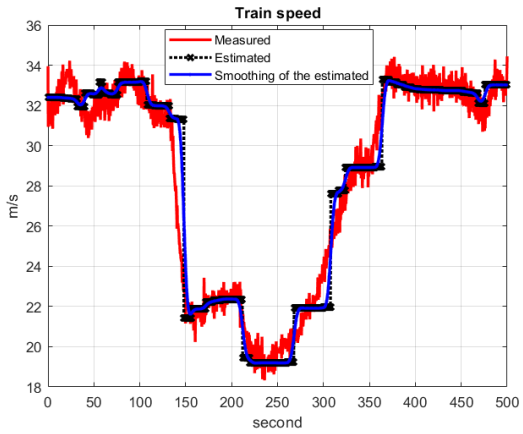

Figure 5.20: *The measured and estimated train speed of the second example.*

Also, in this test, it was not possible to measure the axle RPM therefor, it was extracted from the measured acceleration signal of the axle to be inspected, as illustrated in the first example. After simulating the FE model using the extracted RPM, the simulated vertical and horizontal acceleration signals of the axle with different crack sizes were obtained and added to the measured signals to construct vertical and horizontal axle-box signals of faulty axle.

Figure 5.21 presents an example of the simulated signals of axle with 20% crack size. The faulty vertical and horizontal signals are treated using the tacho-based method and the proposed tacho-less technique.

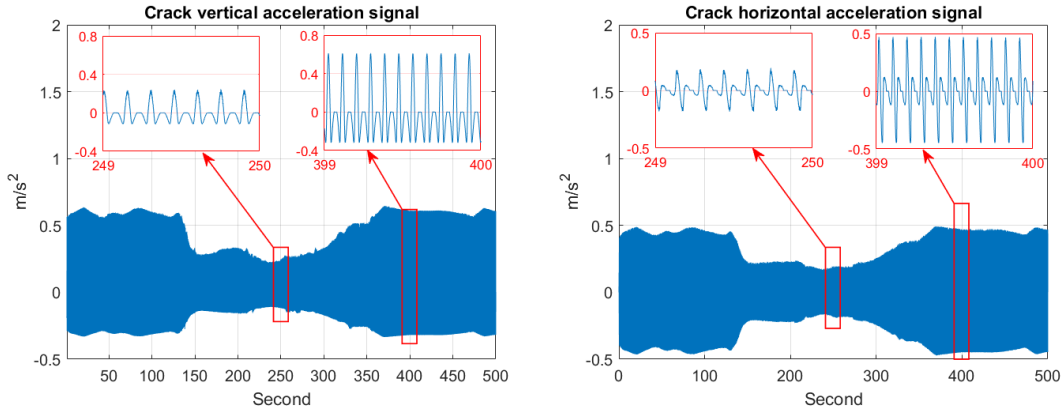

Figure 5.21: *Simulated acceleration signals of axle with 20% crack.*

An example of the processed signals and the order spectra is shown in Figures 5.22 and 5.23 for the vertical and horizontal signals respectively. A good agreement between the results of the two processing techniques can be observed from Figures 5.22 and 5.23. It's worth to observe that, for this small crack size (20%), the spectrum of the horizontal signal gives recognizable harmonic components whilst the spectrum of the vertical signal cannot. This due to the high influence of wheel OOR disturbance arising in vertical signals which cannot be eliminated using the synchronous averaging.

The comparison is extended to another set of faulty signals with different crack sizes and its results is presented in Figure 5.24 for the first three harmonic trends of the vertical and horizontal signals after treated using the two techniques. Considering Figure 5.24, the proposed tacho-less technique results give a satisfactory agreement with the tacho-based method results. Figure 5.24 shows that the harmonic components of the horizontal axle-box acceleration are weakly affected by the noise introduced by rail irregularity or by other sources (e.g. wheel OOR) and can be used to detect a crack at early stage of its propagation. On the other hand, the vertical components are highly affected by these irregularities, especially wheel OOR disturbance, and the influence of relatively large size crack can appear in these components, therefore, the vertical measurements cannot detect the crack at early stage of its propagation.

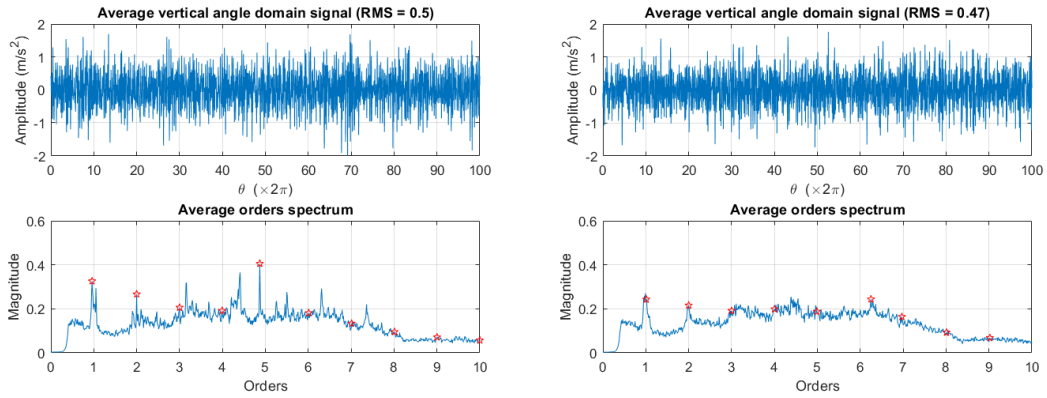

Figure 5.22: *Average order spectra of the vertical angle domain signals (with 20% crack) (left: using the tacho-based method, right: using the proposed tacho-less method).*

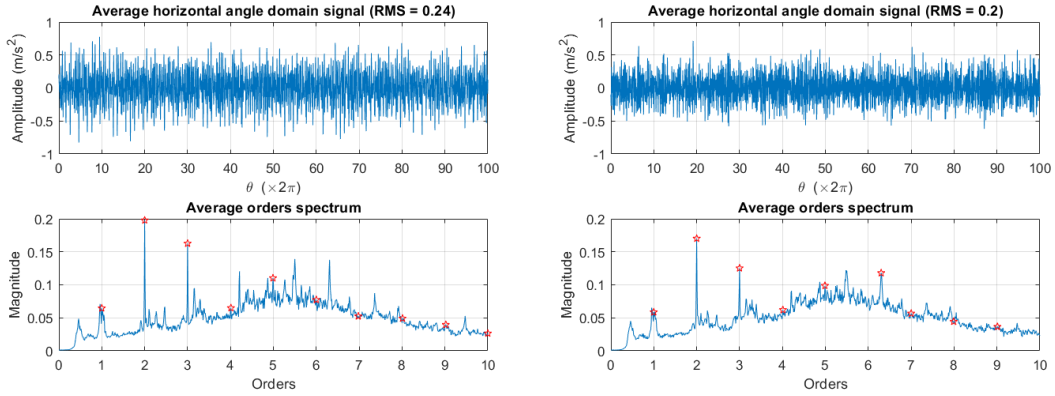

Figure 5.23: *Average order spectra of the horizontal angle domain signals (with 20% crack) (left: using the tacho-based method, right: using the proposed tacho-less method).*

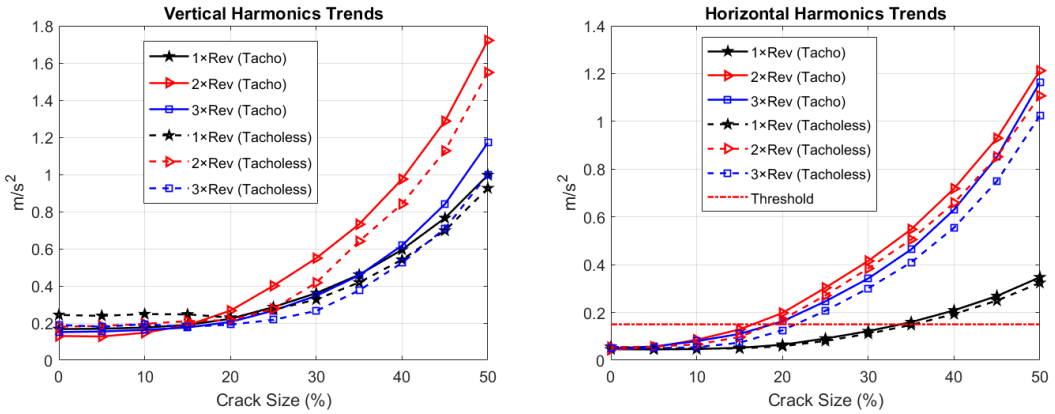

Figure 5.24: *Trends of first three harmonics of faulty signals after processed using the tacho-based method and the proposed tacho-less method.*

Considering again the simple threshold definition introduced in Section 4.4, a threshold with value equal to 0.15 m/s^2 is superimposed on the right subplot of Figure 5.24 as a horizontal line. Figure 5.24 reveals that the magnitudes of 2xRev and 3xRev harmonics of the horizontal axle-box acceleration exceed the threshold at crack sizes between 15% and 20%, which are almost the same detectable sizes that are reported in Section 4.4.

From this chapter, the following points can be summarized:

1. By using faulty signals constructed by adding simulated crack signals to measured acceleration signals, the proposed signal processing technique including the tacho-less technique proved to be able to extract information related to the presence of a crack from non-stationary vibration signals with high background noise.
2. The harmonics components of the vertical axle-box acceleration are strongly affected by the disturbance arising from wheel OOR profile.
3. The 2xRev and 3xRev components of the horizontal axle-box acceleration are almost insensitive to the effect of wheel OOR disturbance, hence, can be used for the continuous monitoring of axle integrity.
4. Cracks with size in the order of 15-20% of the total cross-section area can be detected using the horizontal axle-boxes measurements (based on the simple criterion of crack detection defined in Chapter 4).

CHAPTER 6

Conclusions and Future work

6.1 Conclusions

To maintain European railway at an advanced level as one of the safest transportation means in Europe, condition monitoring for some safety critical components in the vehicles is strongly needed. Railway wheelsets are one of the important elements affect the reliability of railway vehicles (passenger and freight rolling stock elements) in the perspective of safety. Wheelsets consist of three main components, the wheels, the axle and the bearings. The axles are one of the most critical components in railway vehicles since their failure can lead to derailment and, potentially, to catastrophic accidents.

Because the axles are operating under harsh conditions of rotating bending at high number of cycles, a large proportion of all accidents in the rail industry, related to rolling stock failures, is due to crack propagation in the axles. Cracks in railway axles generally propagate in a plane perpendicular to the axles axis, taking the name of transverse cracks. Railway axles are inspected periodically at regular intervals, e.g. for freight wagons, every 600,000 km or 6-year distance, to detect any defects and prevent axles rupture.

To perform an effective inspection test (e.g. Magnetic Particles and Ultra-Sonic), axles need to be removed from the bogie at the maintenance schedule and disassemble the auxiliary systems to access to the main body of the axles which means time, effort and money consuming. Although the high standards of present engineering practice in non-destructive inspection of axles, fatigue induced in-service failures of railway axles still occasionally occur, representing a serious threat to the safe operation of railway systems. Therefore, it's needed to introduce an innovative and effective approach for railway axle continuous structural health monitoring (SHM) to play a pivotal role in further reducing occasional in-service failures of railway axles, which is not meant to replace the existing non-destructive test (NDT) inspections, but rather to serve as an

additional safety measuring tool.

In this thesis, a new method of continuous SHM for railway axles, based on measuring the axle in-service bending vibration to detect the presence of a crack, is proposed. Due to the so-called crack breathing mechanism, the presence of a crack perturbs the axi-symmetric bending stiffness of the axle, affecting the bending vibration at frequencies that are multiple integers of the frequency of revolution, referred to as NxRev. The proposed SHM strategy therefore entails the measure of the first 3 harmonic components of axle vibration.

This strategy has been successfully applied in the past to the detection of cracks in turbine shafts. However, in the case of railway axles the detection of NxRev components is more problematic due to:

1. The high level of disturbance generated by track irregularity and wheel out-of-roundness (OOR). Indeed, the level of vertical axle-box acceleration caused by track irregularity can be up to 500 m/s^2 whereas the amplitude of the acceleration caused by the crack is in the order of magnitude of 1 m/s^2. Wheel OOR typically causes lower amplitudes of axle-box acceleration compared to track irregularity, but the component of the signal caused by this disturbance is periodic with the wheel turn, hence providing the same NxRev components caused by crack breathing mechanism, so that this disturbance cannot be separated by the use of synchronous averaging.

2. Railway axles are rotating at speeds below their first critical speed, whereas shafts in turbomachinery and other industrial machinery are often working above at least the first critical speed.

3. Limited space is available in wheelsets to install the measuring sensors because the axle body is providing support for auxiliary systems.

4. The angular speed of railway axles is changing in complicated way therefore, it produces non-stationary vibration signals.

Considering these challenges, a combination of modelling, simulation and testing activities have been carried out to assess the possibility of using the SHM approach proposed in this thesis. Three models have been built based on non-linear Finite Element (FE) models of the cracked railway axle and simulated at different conditions of crack sizes, crack locations and track disturbances.

After examination of the State of the Art, the first model, non-linear solid Finite Element model of cracked railway solid/hollow axle, is developed using 3D elements (C3D8R) included in the commercial software ABAQUS/CAE representing the crack by means of non-linear contact elements with or without friction. This model is expensive from calculation time point of view because it represents the exact size and shape of railway axle (even with some simplifications for 3D analysis).

To overcome the drawback of highly computationally intensive of the solid FE model, the second model of a cracked axle is defined using Timoshenko beam Finite Element with 6 DOFs per node and a simplified crack breathing mechanism model is applied to a specific element, depending on the crack location, to represent the change of the cross-section area and moments (A, J_x, J_z and J_{xz}). The Timoshenko beam FE

model was coded by MATLAB and verified using results obtained from the solid FE model and against results measured from full-scale rotating bending tests performed on the Dynamic Test Bench for Railway Axles available at the labs of Politecnico di Milano. After validation, different sizes and locations of the crack are simulated for different boundary conditions of railway axle.

Because the proposed SHM technique needs to take into account properly the effect of disturbances associated with track irregularity, wheel OOR and flexibility of the track, more realistic boundary conditions than the ones used in the solid FE and the beam FE models need to be considered for the wheelset. A multi-body (MB) model of a railway vehicle also considering track flexibility is merged with the Timoshenko beam FE model of one cracked axle to form a detailed model of a railway vehicle with one cracked axle (third model). To this aim, the beam FE model is used because it is highly efficient from the computational point of view compared with the solid FE model. In this model, called MB-FE model, the crack breathing mechanism is applied to a specific beam element, depending on the crack location. Also, in this model, track flexibility in vertical and lateral directions has been considered by using the so called "moving track models". The moving track models are assumed to follow the longitudinal forward movement of the vehicle.

The MB model has a total of 57 degrees of freedom (DOF), whereas the Timoshenko beam model has 180 DOF (30 nodes, 6 DOF for each node). Therefore, the MB-FE model has a total of 237 DOF. The MB-FE model was coded in MATLAB and verified by Polimi conventional railway vehicle MB software (ADTReS). After verification, the MB-FE model is used to study the influence of crack propagation, at two positions, on the vibration signals measured at the axle-box in vertical and horizontal (perpendicular to the axle axis in travelling direction), directions.

A tentative crack detection criterion, depending on the mean value (μ) and standard deviation (σ) of a healthy (without considering crack) acceleration signal is proposed.

After examination of the State of the Art, different signal processing techniques are tested to propose an effective technique able to extract the useful information from noisy and non-stationary vibration signals which are representative of signals obtained from railway field. The proposed technique is a combination of diverse techniques from the State of the Art. Because the proposed signal processing technique requires a tacho-signal but in some railway vehicles, it's not possible to add a tachometer hardware, a tacho-less technique suitable for railway continuous SHM applications is proposed and validated.

From the results of the numerical and experimental activities, the following conclusions are formulated:

1. The presence of a crack in railway axle affects not only the vertical vibration, but also the horizontal one (perpendicular to the axle axis in travelling direction) generating harmonic components of bending vibration at frequencies that are multiple integers of the frequency of revolution of the axle, mainly the first three harmonics (1xRev, 2xRev and 3xRev), which can be used to detect the axle crack.

2. Axle-boxes measurements can be used to detect the presence of a crack at any position along the axle.

3. The measure of the horizontal vibration provides a promising indicator of axle fault development because this component is nearly insensitive to the effect of various sources of disturbance, particularly wheel OOR, compared to vertical vibration.

4. The signal processing technique proposed in this thesis is able to rule out the signal components that are unrelated to the angular speed of the axle and provides an order spectrum which enables the clear tracking of NxRev components of vibration even in presence of large noise caused by wheel-rail interaction.

5. The proposed tacho-less technique is suitable for the continuous SHM of railway applications, thus avoiding using tachometer hardware.

6. The simple criterion for crack detection, introduced in this work, shows the possibility of detecting cracks with size in the order of 15-20% of the total section area, depending on the crack location. This means that crack detection according to the method proposed here can be performed when the crack size is still much smaller than its critical size, so that the cracked axle can be safely put out of service avoiding dangerous in-line failures.

7. The proposed method represents a promising opportunity for railway axle continuous SHM, which is not meant to replace the existing NDT inspections, but rather to serve as an additional safety measure to eliminate occasional in-service failures.

6.2 Future work

Some further developments and experiments have been left for the future work due to lack of time:

- The accuracy and sensitiveness of the proposed continuous SHM technique, including all the disturbance effects related to wheel-rail interaction, have to be investigated experimentally. Therefore, as an example, tests on a full-scale roller rig for a complete railway vehicle incorporating one or two cracked axles could be carried out.

- More effective, robust and accurate definition for threshold of railway axle defect detection needs to be introduced. For instance, a threshold definition based on a statistical outlier analysis (e.g. Mahalanobis Squared Distance) applied to the harmonics amplitudes has to be investigated. Moreover, since this is a threshold-based detection, Receiver Operating Characteristic (ROC) curves have to be calculated in order to prove the robustness of the technique against false positives (false indications of the presence of a crack).

- The use of the Ensemble Empirical Mode Decomposition (EEMD) technique is recommended for signal de-noising because this approach is suitable for analyzing non-linear and non-stationary signals. Currently, this approach is highly computationally intensive, but its development is progressing fast.

Bibliography

[1] European Railway Agency(ERA). Railway safety in the european union. 2011.

[2] Mayorkinos Papaelias, Arash Amini, Zheng Huang, Patrick Vallely, Daniel Cardoso Dias, and Spyridon Kerkyras. Online condition monitoring of rolling stock wheels and axle bearings. *Proceedings of the Institution of Mechanical Engineers, Part F: Journal of Rail and Rapid Transit*, 230(3):709–723, 2016.

[3] Andersen T. Analysis of past derailments: Information from data bases, investigation reports and surveys. *DNV presentation on the results of the D-RAIL FP7 Project*.

[4] Keith Bladon, David Rennison, Grigory Izbinsky, Roger Tracy, Trevor Bladon, et al. Predictive condition monitoring of railway rolling stock. *CORE 2004: New Horizons for Rail*, page 22, 2004.

[5] BS EN13261. Railway applications–wheelsets and bogies–axles–product requirements. *European Committee for Standardization*, 2003.

[6] EN 13103. Railway applications-wheelset and bogies-non-powered axles-design method. *European Committee for Standardization/Technical Committee CEN/TC 25*, 2012.

[7] Alten F Grandt Jr. Fundamentals of structural integrity. *Hoboken (NJ): JohnWiley & Sons*, 2004.

[8] Stefano Cantini and Stefano Beretta. *Structural reliability assessment of railway axles*. Lucchini RS, 2011.

[9] Chang-Hong Jiang, Wen You, Long-Shan Wang, Ming Chu, and Ning Zhai. Real-time monitoring of axle fracture of railway vehicles by translation invariant wavelet. In *Machine Learning and Cybernetics, 2005. Proceedings of 2005 International Conference on*, volume 4, pages 2409–2413. IEEE, 2005.

[10] Nicolò Bachschmid, Paolo Pennacchi, and Ezio Tanzi. *Cracked rotors: a survey on static and dynamic behaviour including modelling and diagnosis*. Springer Science & Business Media, 2010.

[11] VI Gorbunov and VA Sutorikhin. Microwave nondestructive testing method. *Applied Physics Research*, 4(1):206, 2012.

[12] R Zoughi and Sergey Kharkovsky. Microwave and millimetre wave sensors for crack detection. *Fatigue & Fracture of Engineering Materials & Structures*, 31(8):695–713, 2008.

[13] RW Ngigi, Crinela Pislaru, Andrew Ball, and Fengshou Gu. Modern techniques for condition monitoring of railway vehicle dynamics. In *Journal of Physics: Conference Series*, volume 364, page 012016. IOP Publishing, 2012.

[14] UK JOSHI. Study on fatigue failure and stress analysis with safe life on railway axle-a review.

[15] Uwe Zerbst, Katrin Mädler, and Hartmut Hintze. Fracture mechanics in railway applications—-an overview. *Engineering fracture mechanics*, 72(2):163–194, 2005.

[16] N Gravier, JJ Viet, and A Leluan. Predicting the life of railway vehicle axles. In *Proceedings of the 12th International Wheelset Congress*, pages 133–146. China, 1998.

[17] S Beretta, M Madia, M Schode, and U Zerbst. Sif solutions for cracks in railway axles under rotating bending. In *Fracture of Nano and Engineering Materials and Structures*, pages 263–264. Springer, 2006.

[18] Uwe Zerbst, M Schödel, and H Th Beier. Parameters affecting the damage tolerance behaviour of railway axles. *Engineering Fracture Mechanics*, 78(5):793–809, 2011.

[19] Mona Soodi. Investigation of laser deposited wear resistant coatings on railway axle steels. 2013.

[20] DS Hoddinott. Railway axle failure investigations and fatigue crack growth monitoring of an axle. *Proceedings of the Institution of Mechanical Engineers, Part F: Journal of Rail and Rapid Transit*, 218(4):283–292, 2004.

[21] Eric M Leishman. *Analysis of Canadian Train Derailments from 2001 to 2014*. PhD thesis, University of Alberta, 2017.

[22] Christian Klinger. Failure analysis on a broken ICE3 railway axle-interdisciplinary approach. 2010.

[23] A Bracciali. Railway wheelsets: history, research and developments. *International Journal of Railway Technology*, 5(1):23–52, 2016.

[24] European Railway Agency(ERA). Railway safety in the european union. 2017.

[25] Meral Bayraktar, Necati Tahrali, and Rahmi Guclu. Reliability and fatigue life evaluation of railway axles. *Journal of mechanical science and technology*, 24(3):671–679, 2010.

[26] RA Smith. Railway fatigue failures: an overview of a long standing problem. *Materialwissenschaft und Werkstofftechnik*, 36(11):697–705, 2005.

[27] RA Smith and S Hillmansen. A brief historical overview of the fatigue of railway axles. *Proceedings of the Institution of Mechanical Engineers, Part F: Journal of Rail and Rapid Transit*, 218(4):267–277, 2004.

[28] K Hirakawa, K Toyama, and M Kubota. The analysis and prevention of failure in railway axles. *International journal of fatigue*, 20(2):135–144, 1998.

[29] SL Dedmon, JM Pilch, and CP Lonsdale. A comparison of railroad axle stress results using different design sizes, loading criteria and analysis methods. In *2001 ASME International Mechanical Engineering Congress and Exposition*, 2001.

[30] S Beretta, A Ghidini, and F Lombardo. Fracture mechanics and scale effects in the fatigue of railway axles. *Engineering fracture mechanics*, 72(2):195–208, 2005.

[31] Viktor Gerdun, Tomaž Sedmak, Viktor Šinkovec, Igor Kovše, and Bojan Cene. Failures of bearings and axles in railway freight wagons. *Engineering Failure Analysis*, 14(5):884–894, 2007.

[32] J Vogwell. Analysis of a vehicle wheel shaft failure. *Engineering Failure Analysis*, 5(4):271–277, 1998.

[33] Sebastian Stichel and Klaus Knothe. Fatigue life prediction for an s-train bogie. *Vehicle System Dynamics*, 29(S1):390–403, 1998.

[34] Wei Chen, Ying Xiong, Kwok-Leung Tsui, and Shuchun Wang. A design-driven validation approach using bayesian prediction models. *Journal of Mechanical Design*, 130(2):021101, 2008.

[35] M McDonald and S Mahadevan. Design optimization with system-level reliability constraints. *Journal of Mechanical Design*, 130(2):021403, 2008.

[36] Giampaolo Mancini, Alessandro Corbizi, Francesco Lombardo, and Steven Cervello. Design of railway axle in compliance with the european norms: high strength alloyed steels compared to standard steels. In *Proceedings of WCRR*, 2006.

[37] JR Snell. Key issues in the application of unified railway axle standards. *Proceedings of the Institution of Mechanical Engineers, Part F: Journal of Rail and Rapid Transit*, 218(4):279–282, 2004.

[38] JR Rudlin and R Shipp. Review of rail axle inspection methods. In *Proceedings of the International Seminar on Railway axles, London, UK*, 2003.

[39] Muhammad Sohail Malik. Reliability analysis of laser ultrasonics as an ndt method for surface defect detection in high speed hollow train axles using experimental and numerical methods. 2015.

[40] Arash Amini. *Online condition monitoring of railway wheelsets*. PhD thesis, University of Birmingham, 2016.

[41] PAWEL ROLEK. *Low Frequency Vibrations analysis as a method for condition based monitoring system for railway axles*. PhD thesis, Italy, 2015.

[42] Michele Carboni and Stefano Cantini. A "model assisted probability of detection" approach for ultrasonic inspection of railway axles. In *18th World Conf. on Nondestructive Testing 2012 Conference, Durban (South Africa)*, 2012.

[43] JA Benyon and AS Watson. The use of monte-carlo analysis to increase axle inspection interval. In *Proceedings of the 13th International Wheelset Congress, Rome, Italy*, 2001.

[44] UIC Leaflet. *Technical specification for the supply of axles for tractive and trailing stock*. Paris, 1987.

[45] John ET Penny and Michael I Friswell. The dynamics of cracked rotors. In *IMAC-XXV: A Conference & Exposition on Structural Dynamics, Orlando, FL, February*, pages 19–22, 2007.

[46] S Beretta, M Carboni, A Lo Conte, D Regazzi, S Trasatti, and M Rizzi. Crack growth studies in railway axles under corrosion fatigue: Full-scale experiments and model validation. *Procedia Engineering*, 10:3650–3655, 2011.

[47] Tejas H Patel and Ashish K Darpe. Influence of crack breathing model on nonlinear dynamics of a cracked rotor. *Journal of Sound and Vibration*, 311(3):953–972, 2008.

[48] Paolo Pennacchi and Andrea Vania. Diagnostics of a crack in a load coupling of a gas turbine using the machine model and the analysis of the shaft vibrations. *Mechanical Systems and Signal Processing*, 22(5):1157–1178, 2008.

[49] KR Fyfe and EDS Munck. Analysis of computed order tracking. *Mechanical Systems and Signal Processing*, 11(2):187–205, 1997.

[50] ABAQUS. Abaqus/explicit (version 6.12) user's manual. *ABAQUS*, 2012.

[51] Jeff Brown. Characterization of msc/nastran & msc/abaqus elements for turbine engine blade frequency analysis. In *Proc. MSC Aerospace Users' Conference*. Citeseer, 1997.

[52] Robert D Cook. *Finite element modeling for stress analysis*. Wiley, 1994.

[53] José Martínez-Casas, Laura Mazzola, Luis Baeza, and Stefano Bruni. Numerical estimation of stresses in railway axles using a train–track interaction model. *International Journal of Fatigue*, 47:18–30, 2013.

[54] Jens CO Nielsen and Anders Johansson. Out-of-round railway wheels-a literature survey. *Proceedings of the Institution of Mechanical Engineers, Part F: Journal of Rail and Rapid Transit*, 214(2):79–91, 2000.

[55] Anders Johansson and Clas Andersson. Out-of-round railway wheels-a study of wheel polygonalization through simulation of three dimensional wheel-rail interaction and wear. *Vehicle System Dynamics*, 43(8):539–559, 2005.

[56] JR Hutchinson. Shear coefficients for timoshenko beam theory. *TRANSACTIONS-AMERICAN SOCIETY OF MECHANICAL ENGINEERS JOURNAL OF APPLIED MECHANICS*, 68(1):87–92, 2001.

[57] R Gasch. A survey of the dynamic behaviour of a simple rotating shaft with a transverse crack. *Journal of sound and vibration*, 160(2):313–332, 1993.

[58] S Beretta, M Carboni, S Cantini, and A Ghidini. Application of fatigue crack growth algorithms to railway axles and comparison of two steel grades. *Proceedings of the Institution of Mechanical Engineers, Part F: Journal of Rail and Rapid Transit*, 218(4):317–326, 2004.

[59] JA Harter. Afgrow users guide and technical manual (v. 4.0012. 15). Technical report, Technical Memorandum, AFRL-VA-WP-TR-2008, Air Force Research Laboratory, Wright-Patterson AFB, OH, 2008.

[60] M Hassan, S Bruni, and M Carboni. Crack detection in railway axle using horizontal and vertical vibration measurements. In *Railway Condition Monitoring 2016 (RCM 2016), 7th IET Conference on*, pages 1–6. IET, 2016.

[61] Nizar Chaar and Mats Berg. Dynamic wheel-rail force measurements and simulations of a high-speed train running on two tracks with different flexibility and irregularities. 2007.

[62] Egidio Di Gialleonardo, Francesco Braghin, and Stefano Bruni. The influence of track modelling options on the simulation of rail vehicle dynamics. *Journal of Sound and Vibration*, 331(19):4246–4258, 2012.

[63] Lu-Hang Zong, Xing-Long Gong, Shou-Hu Xuan, and Chao-Yang Guo. Semi-active h control of high-speed railway vehicle suspension with magnetorheological dampers. *Vehicle System Dynamics*, 51(5):600–626, 2013.

[64] DH Wang and WH Liao. Semi-active suspension systems for railway vehicles using magnetorheological dampers. part i: system integration and modelling. *Vehicle System Dynamics*, 47(11):1305–1325, 2009.

[65] B ORE. 176, bogies with steered or steering wheelsets. Technical report, Report, 1989.

[66] Stefano Bruni, Andrea Collina, Giorgio Diana, and Pietro Vanolo. Lateral dynamics of a railway vehicle in tangent track and curve: tests and simulation. In *THE DYNAMICS OF VEHICLES ON ROADS AND ON TRACKS-SUPPLEMENT TO VEHICLE SYSTEM DYNAMICS, VOLUME 33. PROCEEDINGS OF THE 16TH IAVSD SYMPOSIUM HELD IN PRETORIA, SOUTH AFRICA, AUGUST 30-SEPTEMBER 3, 1999*, 2000.

[67] Simon Iwnicki. *Handbook of railway vehicle dynamics*. CRC press, 2006.

[68] Z Peng and N Kessissoglou. An integrated approach to fault diagnosis of machinery using wear debris and vibration analysis. *Wear*, 255(7):1221–1232, 2003.

[69] Hojjat Adeli and Xiaomo Jiang. *Intelligent infrastructure: neural networks, wavelets, and chaos theory for intelligent transportation systems and smart structures*. Crc Press, 2009.

[70] Daniel Balageas, Claus-Peter Fritzen, and Alfredo Güemes. *Structural health monitoring*, volume 90. John Wiley & Sons, 2010.

[71] N Tandon and A Parey. Condition monitoring of rotary machines. In *Condition Monitoring and Control for Intelligent Manufacturing*, pages 109–136. Springer, 2006.

[72] D Goyal and BS Pabla. The vibration monitoring methods and signal processing techniques for structural health monitoring: A review. *Archives of Computational Methods in Engineering*, 23(4):585–594, 2016.

[73] Albert HC Tsang. Condition-based maintenance: tools and decision making. *Journal of Quality in Maintenance Engineering*, 1(3):3–17, 1995.

[74] Robert Bond Randall. *Vibration-based condition monitoring: industrial, aerospace and automotive applications*. John Wiley & Sons, 2011.

[75] Jordi CusidÓCusido, Luis Romeral, Juan A Ortega, Javier A Rosero, and Antonio GarcÍaGarcia Espinosa. Fault detection in induction machines using power spectral density in wavelet decomposition. *IEEE Transactions on Industrial Electronics*, 55(2):633–643, 2008.

[76] Greg W Terpay, George G Zipfel, and G George. Measuring blade condition in a gas turbine engine using eddy-currents. In *Proc. 9th Int. Conf. Adaptive Structures Technologies*, pages 71–80, 1999.

[77] Mike Dowell and Garrett Sylvester. Turbomachinery prognostics and health management via eddy current sensing: current developments. In *Aerospace Conference, 1999. Proceedings. 1999 IEEE*, volume 3, pages 1–9. IEEE, 1999.

[78] LM Adams Jr. Rotating machinery vibration. from analysis to troubleshooting mechanical engneering. *A Series of Textbooks and Reference Books*, 2001.

[79] Frédéric Restagno, Jérôme Crassous, E Charlaix, and M Monchanin. A new capacitive sensor for displacement measurement in a surface-force apparatus. *Measurement Science and Technology*, 12(1):16, 2001.

[80] Wang Zhao-hua. Capacitive sensor based on active bridge circuit and its measurement system [d]. *Beijing University of Chemical Technology Master Degree Thesis*, 11, 2006.

[81] MG Li, RX Sun, and Yong Li. Research on vibration sensor of ultra low frequency. *Colliery Mechanical & Electrical Technology*, 3:012, 2008.

[82] Jens Trampe Broch. *Mechanical vibration and shock measurements*. Brüel & Kjær, 1980.

[83] Raymond R Bouche. Calibration of shock and vibration measuring transducers. Technical report, DTIC Document, 1979.

[84] Xu Fu-cheng. Common vibration sensor and its typical application circuit [j]. *Practical Electronics*, 10:13–15, 2008.

[85] Young S Shin and Jae-Jin Jeon. Pseudo wigner-ville time-frequency distribution and its application to machinery condition monitoring. *Shock and Vibration*, 1(1):65–76, 1993.

[86] Scott W Doebling, Charles R Farrar, Michael B Prime, and Daniel W Shevitz. Damage identification and health monitoring of structural and mechanical systems from changes in their vibration characteristics: a literature review. 1996.

[87] Hongyu Yang, Joseph Mathew, and Lin Ma. Vibration feature extraction techniques for fault diagnosis of rotating machinery: a literature survey. 2003.

[88] Anders Rytter. Vibrational based inspection of civil engineering structures. 1993.

[89] Gyuhae Park, Daniel E Muntges, and Daniel J Inman. Self-monitoring and self-healing jointed structures. In *Key Engineering Materials*, volume 204, pages 75–84. Trans Tech Publ, 2001.

[90] Bharat M Shah, JC Cannington, EJ Ferko, YS Kwon, SA Saunders, N Phan, and JM Candela. P-3c service life management. In *Proceedings of 2004 USAF ASIP Conference*, 2004.

[91] J Tlusty. The detection of tool breakage in milling operations. *Journal of Engineering for Industry*, 110:271, 1988.

[92] Imed Khemili and Mnaouar Chouchane. Detection of rolling element bearing defects by adaptive filtering. *European Journal of Mechanics-A/Solids*, 24(2):293–303, 2005.

[93] C James Li. Signal processing in manufacturing monitoring. In *Condition monitoring and control for intelligent manufacturing*, pages 245–265. Springer, 2006.

[94] Hoon Sohn and Charles R Farrar. Damage diagnosis using time series analysis of vibration signals. *Smart materials and structures*, 10(3):446, 2001.

[95] Mitchell Lebold, Katherine McClintic, Robert Campbell, Carl Byington, and Kenneth Maynard. Review of vibration analysis methods for gearbox diagnostics and prognostics. In *Proceedings of the 54th meeting of the society for machinery failure prevention technology*, volume 634, page 16, 2000.

[96] Athanasios Papoulis and S Unnikrishna Pillai. *Probability, random variables, and stochastic processes*. Tata McGraw-Hill Education, 2002.

[97] D Dyer and RM Stewart. Detection of rolling element bearing damage by statistical vibration analysis. *ASME J. Mech. Des*, 100(2):229–235, 1978.

[98] Shie Qian and Dapang Chen. *Joint time-frequency analysis: methods and applications*. Prentice-Hall, Inc., 1996.

[99] Leon Cohen. *Time-frequency analysis*, volume 778. Prentice Hall PTR Englewood Cliffs, NJ:, 1995.

[100] M-C Pan, P Sas, and H Van Brussel. Nonstationary time-frequency analysis for machine condition monitoring. In *Time-Frequency and Time-Scale Analysis, 1996., Proceedings of the IEEE-SP International Symposium on*, pages 477–480. IEEE, 1996.

[101] R Klein, D Ingman, and S Braun. Non-stationary signals: phase-energy approach-theory and simulations. *Mechanical Systems and Signal Processing*, 15(6):1061–1089, 2001.

[102] In Soo Koo and Whan Woo Kim. The development of reactor coolant pump vibration monitoring and a diagnostic system in the nuclear power plant. *ISA transactions*, 39(3):309–316, 2000.

[103] WJ Wang and PD McFadden. Early detection of gear failure by vibration analysis–ii. interpretation of the time-frequency distribution using image processing techniques. *Mechanical Systems and Signal Processing*, 7(3):205–215, 1993.

[104] Svend Gade and Klaus Gram-Hansen. Non-stationary signal analysis using wavelet transform, short-time fourier transform and wigner-ville distribution. *Bruel & Kjaer Technical Review*, (2), 1996.

[105] Juan Pablo Amezquita-Sanchez, Arturo Garcia-Perez, Rene J Romero-Troncoso, Roque A Osornio-Rios, and Gilberto Herrera-Ruiz. High-resolution spectral-analysis for identifying the natural modes of a truss-type structure by means of vibrations. *Journal of Vibration and Control*, 19(16):2347–2356, 2013.

[106] Ming Zhao, Jing Lin, Xiufeng Wang, Yaguo Lei, and Junyi Cao. A tacho-less order tracking technique for large speed variations. *Mechanical Systems and Signal Processing*, 40(1):76–90, 2013.

[107] Stephan Schmidt, Philippus Stephanus Heyns, and Johan Pieter De Villiers. A tacholess order tracking methodology based on a probabilistic approach to incorporate angular acceleration information into the maxima tracking process. *Mechanical Systems and Signal Processing*, 100:630–646, 2018.

[108] Carl Sunde. *Wavelet and Spectral Analysis of Some Selected Problems in Reactor Diagnostics*. PhD thesis, Chalmers tekniska högsk., 2004.

[109] Stephane G Mallat. A theory for multiresolution signal decomposition: the wavelet representation. *IEEE transactions on pattern analysis and machine intelligence*, 11(7):674–693, 1989.

[110] J Zou and J Chen. A comparative study on time–frequency feature of cracked rotor by wigner–ville distribution and wavelet transform. *Journal of Sound and Vibration*, 276(1):1–11, 2004.

[111] David E Newland. *Wavelet analysis of vibration signals*. Wiley Online Library, 1996.

[112] J Vass, R Šmíd, RB Randall, P Sovka, C Cristalli, and B Torcianti. Avoidance of speckle noise in laser vibrometry by the use of kurtosis ratio: Application to mechanical fault diagnostics. *Mechanical Systems and Signal Processing*, 22(3):647–671, 2008.

[113] Leon Cohen. Generalized phase-space distribution functions. *Journal of Mathematical Physics*, 7(5):781–786, 1966.

[114] Norden E Huang, Zheng Shen, Steven R Long, Manli C Wu, Hsing H Shih, Quanan Zheng, Nai-Chyuan Yen, Chi Chao Tung, and Henry H Liu. The empirical mode decomposition and the hilbert spectrum for nonlinear and non-stationary time series analysis. In *Proceedings of the Royal Society of London A: Mathematical, Physical and Engineering Sciences*, volume 454, pages 903–995. The Royal Society, 1998.

[115] H-I Choi and William J Williams. Improved time-frequency representation of multicomponent signals using exponential kernels. *IEEE Transactions on Acoustics, Speech, and Signal Processing*, 37(6):862–871, 1989.

[116] M Chiollaz and B Favre. Engine noise characterisation with wigner-ville time-frequency analysis. *Mechanical Systems and Signal Processing*, 7(5):375–400, 1993.

[117] Wieslaw J Staszewski, Keith Worden, and Geof R Tomlinson. Time–frequency analysis in gearbox fault detection using the wigner–ville distribution and pattern recognition. *Mechanical systems and signal processing*, 11(5):673–692, 1997.

[118] TACM Classen and Wolfgang FG Mecklenbrauker. The wigner distribution-a tool for time-frequency signal analysis, part i: continuous-time signals. *Philips J. Res*, 35(3):217–250, 1980.

[119] Naim Baydar and Andrew Ball. A comparative study of acoustic and vibration signals in detection of gear failures using wigner–ville distribution. *Mechanical systems and signal processing*, 15(6):1091–1107, 2001.

[120] Megha Agarwal and RC Jain. Ensemble empirical mode decomposition: An adaptive method for noise reduction. *IOSR J. Electron. Commun. Eng*, 5:60–65, 2013.

[121] Norden E Huang, Zheng Shen, and Steven R Long. A new view of nonlinear water waves: the hilbert spectrum 1. *Annual review of fluid mechanics*, 31(1):417–457, 1999.

[122] Zhaohua Wu and Norden E Huang. Ensemble empirical mode decomposition: a noise-assisted data analysis method. *Advances in adaptive data analysis*, 1(01):1–41, 2009.

[123] Zhaohua Wu and Norden E Huang. A study of the characteristics of white noise using the empirical mode decomposition method. In *Proceedings of the Royal Society of London A: Mathematical, Physical and Engineering Sciences*, volume 460, pages 1597–1611. The Royal Society, 2004.

[124] Patrick Flandrin, Paulo Gonçalves, and Gabriel Rilling. Emd equivalent filter banks, from interpretation to applications. *Hilbert-Huang transform and its applications*, pages 57–74, 2005.

[125] ZK Peng, W Tse Peter, and FL Chu. An improved hilbert–huang transform and its application in vibration signal analysis. *Journal of sound and vibration*, 286(1):187–205, 2005.

[126] Ricardo L de Queiroz and KR Rao. Time-varying lapped transforms and wavelet packets. *IEEE transactions on signal processing*, 41(12):3293–3305, 1993.

[127] Maurice L Adams. Rotating machinery vibration. *VIBRATIONS-WILLOWBROOK-*, 16(4):12–13, 2000.

[128] Dennis H Shreve. Signal processing for effective vibration analysis. *IRD Mechanalysis*, 1995.

[129] Jie Gao, Lifeng Wu, Hongmin Wang, and Yong Guan. Development of a method for selection of effective singular values in bearing fault signal de-noising. *Applied Sciences*, 6(5):154, 2016.

[130] Jian-ming DING, Jian-hui LIN, Han WANG, and Sen LI. Detection of the dynamic unbalance with cardan shaft applying the second wavelet transform and singular value decomposition [j]. *Journal of Mechanical Engineering*, 50(12):100–117, 2014.

[131] Z Chen and CK Mechefske. Machine signature identification by analysis of impulse vibration signals. *Journal of sound and vibration*, 244(1):155–167, 2001.

[132] Huiming Jiang, Jin Chen, Guangming Dong, Tao Liu, and Gang Chen. Study on hankel matrix-based svd and its application in rolling element bearing fault diagnosis. *Mechanical systems and signal processing*, 52:338–359, 2015.

[133] Wen-Xian Yang and W Tse Peter. Development of an advanced noise reduction method for vibration analysis based on singular value decomposition. *NDT & E International*, 36(6):419–432, 2003.

[134] Xuezhi Zhao and Bangyan Ye. Selection of effective singular values using difference spectrum and its application to fault diagnosis of headstock. *Mechanical Systems and Signal Processing*, 25(5):1617–1631, 2011.

[135] Fan Jiang, Zhencai Zhu, Wei Li, Gongbo Zhou, and Guoan Chen. 1504. fault diagnosis of rotating machinery based on noise reduction using empirical mode decomposition and singular value decomposition. *Journal of Vibroengineering*, 17(1), 2015.

[136] PN Saavedra and CG Rodriguez. Accurate assessment of computed order tracking. *Shock and Vibration*, 13(1):13–32, 2006.

[137] Frédéric Bonnardot, Mohamed El Badaoui, RB Randall, J Daniere, and François Guillet. Use of the acceleration signal of a gearbox in order to perform angular resampling (with limited speed fluctuation). *Mechanical Systems and Signal Processing*, 19(4):766–785, 2005.

[138] T Heyns, PS Heyns, and Radoslaw Zimroz. Combining discrepancy analysis with sensorless signal resampling for condition monitoring of rotating machines under uctuating operations. *International Journal of Condition Monitoring*, 2(2):52–58, 2012.

[139] Jacek Urbanek, Tomasz Barszcz, and Jerome Antoni. A two-step procedure for estimation of instantaneous rotational speed with large fluctuations. *Mechanical Systems and Signal Processing*, 38(1):96–102, 2013.

[140] David Abboud, J Antoni, S Sieg-Zieba, and M Eltabach. Envelope analysis of rotating machine vibrations in variable speed conditions: A comprehensive treatment. *Mechanical Systems and Signal Processing*, 84:200–226, 2017.

[141] Guolin He, Kang Ding, Weihua Li, and Xintao Jiao. A novel order tracking method for wind turbine planetary gearbox vibration analysis based on discrete spectrum correction technique. *Renewable Energy*, 87:364–375, 2016.

[142] Quentin Leclère, Hugo André, and Jérôme Antoni. A multi-order probabilistic approach for instantaneous angular speed tracking debriefing of the cmmno14' diagnosis contest. *Mechanical Systems and Signal Processing*, 81:375–386, 2016.